Photonic crystal Fano structures for all-optical signal processing

Bekele, Dagmawi Alemayehu

Publication date:
2018

Document Version
Publisher's PDF, also known as Version of record

DTU Fotonik
Department of Photonics Engineering

Photonic crystal Fano structures for all-optical signal processing

A dissertation submitted in partial fulfilment of the requirements for the degree of Doctor of Philosophy

Dagmawi Alemayehu Bekele

July 2018

Project period:	May 2015 – July 2018
Supervisors:	Prof. Jesper Mørk Assoc. Prof. Kresten Yvind Dr. Luisa Ottaviano
Ph.D. defense date:	September 18, 2018
Ph.D. defense committee:	Dr. Lars Hagedorn Frandsen Dr. Liam O'Faolain Dr. Alfredo De Rossi

Abstract

The capacity of optical communication links has been growing very fast as a result of the deployment of dense modulation formats, various multiplexing schemes, the use of multi-core fibres, and other developments. However, switching data packets in data centres between such high speed optical links is still one of the main causes of bottlenecks. This is mainly due to the need for conversion from optical domain to electrical domain and vice versa for switching and signal processing. The use of all-optical switches is believed to enable signal processing in the optical domain without the need for conversion to the electrical domain, hence avoiding bottlenecks and large energy dissipation. Our work focuses on the experimental demonstration of fast and energy-efficient all-optical switching using photonic integrated circuits.

We have investigated coupled cavity-waveguide structures realized in indium phosphide photonic crystal membranes. The interference between the discrete modes of the cavity and the continuum of waveguide modes results in an asymmetric Fano resonance lineshape, which is characterized by having its transmission maximum and minimum within a small spectral range. Two types of Fano resonances with different spectral shapes have been demonstrated. By combining these characteristic line shapes with carrier-induced nonlinear resonance shifts, devices potentially suitable for all-optical signal processing applications have been designed.

Considerable effort has been put into fabrication and platform development such as implementation of grating couplers for efficient light coupling into and out of the devices, selective membranization of the photonic crystal membrane, and implementation of a p-i-n junction for carrier sweep-out mechanisms. The fabricated devices are shown to perform well in various signal processing experiments.

We have experimentally demonstrated the use of Fano resonances for carving-out short pulses from long-duration input pulses. Input pulses as long as ~ 500 ps and ~ 100 ps can be shortened to ~ 30 ps and ~ 20 ps pulses, respectively. This self-pulse carving feature is also implemented for low-duty cycle return-to-zero on-

off keying (RZ-OOK) signal generation at 2 Gbit/s with energy consumption down to ~ 1 pJ/bit.

Reshaping of optical data signals using Fano resonances is another application that we have been investigating. The combination of an asymmetric lineshape with a nonlinear resonance shift can be used to realize nonlinear power transfer functions suitable for suppression of amplitude fluctuations of data signals. Using these transfer functions, we have demonstrated reshaping of 10 Gbit/s RZ-OOK data signals with energy consumption down to 41 fJ/bit.

Furthermore, we have investigated the switching performances of the devices in a pump-probe measurement scheme in which the pump triggers the resonance shift, hence inducing the switching action. This allowed demonstration of error-free 10 Gbit/s wavelength conversion and 40 Gbit/s to 10 Gbit/s optical time domain demultiplexing applications. All these functionalities are compared to the use of the conventional Lorentzian-shaped resonances using coupled-mode theory. Moreover, prospects of improving device performances and future perspectives are discussed.

Resumé (In Danish)

Kapaciteten af optiske kommunikationskæder er vokset meget hurtigt som følge af implementeringen af kompakte modulationsformater, diverse multiplexing-protokoller, anvendelse af multikerne-fibre samt andre udviklinger. Skiftningen af datapakker i datecentre imellem sådanne højhastigheds optiske kæder er dog stadigvæk en af hovedårsagerne til flaskehalse. Dette skyldes hovedsageligt behovet for konvertering fra det optiske domæne til det elektriske domæne og omvendt for både omskiftning og signalbehandling. Brugen af kun-optiske omskiftere antages at muliggøre signalbehandling i det optiske domæne uden behov for konvertering til det elektriske domæne, og derved undgå flaskehalse og store energitab. Vores arbejde fokuserer på den eksperimentelle demonstration af hurtig og energieffektiv kun-optisk omskiftning ved brug af fotoniske integrerede kresløb.

Vi har undersøgt koblede kavitet-bølgeleder-strukturer realiseret i fotoniske krystalmembraner af indiumfosfid. Interferensen mellem de diskrete tilstande i kaviteten og kontinuummet af tilstande i bølgelederen resulterer i en asymmetrisk Fano-resonans spektralform, som er karakteriseret ved at have dets transmissions-maksimum og -minimum inden for et smalt spektralområde. To typer af Fano-resonanser med forskellige spektrale former er blevet demonstreret. Ved at kombinere disse karakteristiske spektralformer med ladningsbærerinducerede ikke-lineære resonansskift, er enheder potentielt egnede til kun-optisk signalbehandlingsapplikationer blevet designet.

Vi har eksperimentelt demonstreret brugen af Fano-resonanser til udskæring af korte pulser fra langvarige indgangspulser. Indgangspulser så lange som $\sim$ 500 ps og $\sim$ 100 ps kan forkortes til henholdsvist $\sim$ 30 ps og $\sim$ 20 ps pulser. Denne selvpulsudskæringsfunktion er også implementeret til low-duty cycle return-to-zero on-off keying (RZ-OOK) signalbehandling ved 2 Gbit/s med et energiforbrug ned til $\sim$ 1 pJ/bit.

Omformning af optiske datasignaler ved brug af Fano-resonanser er en anden applikation, som vi har undersøgt. Kombinationen af en asymmetrisk

spektralform med et ikke-lineært resonansskift kan bruges til at realisere ikke-lineære overføringsfunktioner velegnede til undertrykkelse af amplitudefluktuationer i datasignaler. Ved brug af disse overføringsfunktioner har vi demonstreret omformning af 10 Gbit/s RZ-OOK datasignaler med et energiforbrug ned til 41 fJ/bit.

Derudover har vi undersøgt omskiftningsydeevnerne for enhederne i en pumpe-probe målingsprotokol, i hvilken pumpen udløser et resonansskift og dermed inducerer omskiftningshandlingen. Dette tillod demonstration af fejlfri 10 Gbit/s bølgelængdekonvertering og 40 Gbit/s til 10 Gbit/s optisk tidsdomæne demultiplexingsapplikationer. Alle disse funktioner er sammenlignet med brugen af den konventionelle Lorentz-formede resonans ved brug a koblede tilstande-teori. Desuden drøftes udsigterne til at forbedre enhedsydeevnerne og fremtidige perspektiver.

Preface

This thesis is submitted in candidacy for the PhD degree from the Technical University of Denmark (DTU). The project has been carried out in the Quantum and Laser Photonics group at DTU Fotonik from May 2015 to July 2018, under the supervision of Professor Jesper Mørk, Associate Professor Kresten Yvind, and Dr. Luisa Ottaviano. This Ph.D. project is the continuation of previous research efforts by Mikkel Heuck and Yi Yu. It is part of the research activities in the NAnophotonics for TErabit Communications (NATEC) centre of excellence which is financially supported by the Villum Fonden.

The research activities in the NATEC centre focuses on light-matter interaction in nanoscale devices, and the use of these devices for controlling light emission and propagation. The Ph.D. project specifically involves the investigation of passive photonic crystal devices aiming at the realization of all-optical switches for signal processing applications. It has been carried out in close collaboration with the Silicon Photonics for Optical Communications (SPOC) centre of excellence, which is also at DTU Fotonik.

Acknowledgements

First and foremost, I would like to express my great gratitude to my supervisor Jesper Mørk for his excellent guidance, endless support, and sharing his years of wisdom. I am very much grateful to have studied under him, and I could not have wished for a better supervisor for my Ph.D. study. I would like to thank my co-supervisors Kresten Yvind and Luisa Ottaviano for their competent support and excellent discussions on device physics and fabrication. A special thanks goes to Yi Yu for his support, encouragement, and excellent discussions which made this work possible. I was privileged to have a supervisors team of four researchers Jesper, Kresten, Luisa and Yi. This team has brought interesting research problems, have asked the right questions, and suggested possible solutions during our biweekly meetings. This has provided me the chance to investigate interesting problems and kept me motivated.

I would like to thank Leif Katsuo Oxenløwe and Hao Hu for their great help and guidance for our optical communication experiments. I would like to thank my former colleague at DTU Fotonik, Gyeong Cheol Park, for introducing me to the exciting world of fabrication. Most importantly, for teaching me all the good skills and best practices required to efficiently fabricate photonic devices. Additionally, I would also like to thank DTU Danchip staff for their help and support in the cleanroom.

Furthermore, would like to thank DTU Fotonik for providing us with a great research environment, fully equipped labs, and well-collaborating research groups. My Ph.D. project involved collaboration of three research groups at DTU Fotonik. This was only possible because of the positive environment we have been provided with at Fotonik. I am grateful to meeting many brilliant co-workers who shared their experience with me during this journey. Particularly, the Quantum and laser photonics group members with whom I had interesting lunch talks, and coffee breaks. I would like to thank Kristoffer Bitsch Joanesarson and Thorsten Svend Rasmussen for taking their time to read and provide me their feedback for my

thesis.

Finally, my deepest gratitude goes to my father, Alemayehu, and my sister, Rahel, for their continued encouragement. Although they were literally thousands of kilometers away, their enormous love and unconditional support was always present and felt.

Dagmawi Alemayehu Bekele
DTU, Kongens Lyngby
July 16, 2018

List of publications

Journal publications

[1] **D. A. Bekele**, Y. Yu, H. Hu, P. Guan, L. Ottaviano, M. Galili, L. K. Oxenløwe, K. Yvind, and J. Mork, "Pulse carving using nanocavity-enhanced nonlinear effects in photonic crystal Fano structures," Opt. Lett. **43**, 955 (2018).

[2] **D. A. Bekele**, Y. Yu, H. Hu, P. Guan, M. Galili, L. Ottaviano, L. K. Oxenløwe, K. Yvind, and J. Mork, "Signal reshaping and noise suppression using photonic crystal Fano structures," Opt. Express 26(15), 19596 (2018).

Conference proceedings

[1] **D. A. Bekele**, Y. Yu, H. Hu, L. K. Oxenløwe, K. Yvind, and J. Mork, "Fano resonances for realizing compact and low energy consumption photonic switches," in Proc. 20th International Conference on Transparent Optical Networks 2018 (ICTON 2018), Bucharest, Romania.

[2] **D. A. Bekele**, Y. Yu, H. Hu, P.-Y. Bony, L. Ottaviano, L. K. Oxenløwe, K. Yvind, and J. Mork, "Optical time domain demultiplexing using Fano resonance in InP photonic crystals," in 2017 CLEO/Europe-EQEC) (IEEE, 2017), pp. 1–1, Munich, Germany.

[3] **D. A. Bekele**, Y. Yu, H. Hu, Y. Ding, A. Sakanas, L. Ottaviano, E. Semenova, L. K. Oxenløwe, K. Yvind, and J. Mork, "Photonic crystal Fano resonances for realizing optical switches, lasers, and non-reciprocal elements," in Active Photonic Platforms IX, vol. 10345, p. 103451V, International Society for Optics and Photonics, 2017, San Diego, USA.

[4] **D. A. Bekele**, Y. Yu, H. Hu, P. Guan, L. Ottaviano, M. Galili, L. K. Oxenløwe, K. Yvind, and J. Mork, "Parity control of Fano resonances and its

application for signal regeneration and pulse carving," in Proceedings of the 8th international Conference on Metamaterials, Photonic crystals and Plasmonics 2017 (META 2017), Seoul, South Korea.

[5] J. Mork, Y. Yu, **D. A. Bekele**, K. S. Mathiesen, A. Rasoulzadeh, E. Semenova, L. Ottaviano, A. Sakanas, and K. Yvind, " Lasers, switches and non-reciprocal elements based on photonic crystal Fano resonances," In Numerical Simulation of Optoelectronic Devices (NUSOD), 2017 International Conference on, pp. 1-2. IEEE, 2017, Copenhagen, Denmark.

[6] J. Mork, Y. Yu, **D. A. Bekele**, K. S. Mathiesen, T. S. Rasmussen, E. Semenova, L. Ottaviano, A. Sakanas, and K. Yvind, " Photonic crystal Fano lasers and Fano switches," In Microoptics Conference (MOC), 2017 22nd, pp. 88-89. IEEE, 2017, Tokyo, Japan.

[7] Y. Yu, **D. A. Bekele**, H. Hu, W. Xue, L. K. Oxenløwe, K. Yvind, and J. Mork, "Photonic crystal Fano structures and their application to ultrafast switching and lasers," In Asia Communications and Photonics Conference, pp. AF4C-2. Optical Society of America, 2016, Wuhan, China.

Contents

Chapter 1

Introduction

1.1 Motivation

In the digital age that we live in, the role of internet is increasingly important part of our daily lives. With most of our home appliances, computers, smartphones, vehicles, refrigerators etc., sharing information with each other, the internet traffic and the associated energy consumption have been increasing exponentially [1, 2]. In order to successfully meet these demands of Internet of Things, serious contributions to the advancement of technology must be achieved as the result of synergistic research activities between multidisciplinary fields of science [1].

The well-established electronic computing technology, which has been used widely and gradually improved for decades, is reaching its physical limitation due to the high processing speed required to cope up with the exponentially growing data traffic [2, 3]. As the speed of operation increases, the energy required for interconnection between the electronic processing units becomes very high, especially for longer wire connections [4]. This is due to the energy required for charging and discharging of the electrical lines, and the increase in the resistive loss in metals at high oscillation frequency leading to large heat dissipation [2, 3].

On the other hand, fiber optics has proved to be the best means of sending large information over long distances, at low loss, and at high speed. The fact that light beams can be easily transmitted in parallel, and do not suffer from crosstalk, is of great importance [3]. Optical fiber is further advancing in data centers for connections between different parts of large electronic systems such as racks. Thus, optical interconnect is replacing the lossy electrical wires and substantially mitigating the energy and density problems [5]. The question is whether optics can be used to reduce energy dissipation within racks, chip-to-chip and possibly on-chip communications ranging from 1 cm to 10 m [4]. The key goals that are desired for such interconnects are simplicity, possibility for high density placement, and total energy consumptions per bit smaller than 10 fJ/bit [4].

Optical technology has also the opportunity to go beyond being just a convenient pipe for ultrafast data transmission, it can actually perform data signal processing [3]. This involves the efforts for building optical transistors that can perform all-optical switching and logic operations [3, 6]. However, this technology is still in its infancy and a lot of debate is going on whether optical transistors are the next logical steps or not [3, 6]. Here, the basic issue is that photons do not interact directly with each other, which makes the control of photons much more difficult than that of electrons. However, it is important to note that the design of optical transistors does not necessarily have to mimic the design of the electronic transistor, just as the design of electronic computers did not mimic the design of mechanical computing devices [3].

Nonlinear optics offers the possibility that photons can interact with each other via electrons or atoms of the host environment, enabling certain signal processing functions to be executed optically [7]. Here, a key motivation is that optical techniques do not need to "touch" or switch every individual bit as electronic transistors do [7]. Moreover, optically assisted signal processing can use optics for what it does well and electronics for what it does best. Optics can perform few functions very fast, and electronics is best for doing accurate complex computations with buffers and memory [7]. Ultimately, electronics and optics in computing are more complementary than competitive [3, 4].

1.2 All-optical signal processing

Integrated electronic circuits have continued to be the mainstream components for data signal processing at network nodes due to their ability to perform logic operations easily, mass production facilities, and high reliability [2]. At these network nodes, an optical transceiver is used to convert the incoming optical data signal to an electrical signal, and vice versa. The electrical signal is then switched, processed and regenerated before converting the resulting signal back to the optical domain for further transmission [2, 7, 8].

As described in the previous section, photonic integrated circuits, in which light beams manipulate the flow of other beams of light, are the long-standing goal for developing fast, low energy consumption, optical signal processing units [3, 9]. Performing signal processing entirely in optical domain offers the opportunity to avoid photonics to electronics conversion [3]. This will substantially benefit the system in terms of eliminating bulky and power hungry electrical hardware, in addition to increased communication capacity and speed [7, 8, 10].

There are several qualitative requirements that are essential for any practical logic device that should be met other than the energy consumption limit. These include cascadability, fan-out, logic-level restoration, input-output isolation, absence of critical biasing, and logic level independent of device loss [6]. Here, fan-out refers to the case in which the output of one stage must be able to drive the inputs of at

least two subsequent stages. It is clear that these requirements are far fetched with the current all-optical signal processing schemes. However, this also means that substantial breakthroughs are required very soon. Therefore, we should continue our efforts on investigating and implementing various device structures.

In an effort to build compact and low energy consumption all-optical switches, nanocavities provide unique opportunities due to their large field enhancement and small mode volumes [8]. The large field enhancement or the high quality-factor of nanocavities enable efficient light-matter interaction contributing to low energy consumption devices. Several all-optical switches have been reported using various device configurations exploiting resonant structures. Figure 1.1 shows a few examples of such devices. Figure 1.1(a) shows the scanning electron microscope

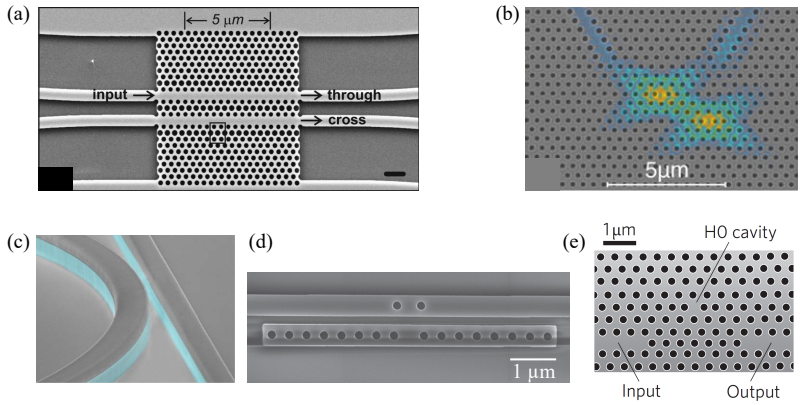

Figure 1.1: Scanning electron microscope (SEM) images showing examples of all-optical devices. (a) Slow light silicon PhC directional coupler switch [11]. (b) GaAs PhC switch consisting of coupled cavities connected to access waveguides [12]. (c) AlGaAs-on-insulator frequency comb source consisting of a micro-resonator coupled with a bus waveguide [13]. (d) A PhC nanobeam cavity side-coupled with a waveguide forming a Fano resonance structure [14]. (e) InGaAsP PhC switch consisting of input-output waveguides coupled to a nanocavity [8].

(SEM) image of a silicon photonic crystal directional coupler switch consisting of two identical slow light waveguides placed in close proximity to one another. Light from one waveguide couples to the other waveguide with very short coupling length and switching times as low as 3 ps [11].

Figure 1.1(b) shows the SEM image of gallium arsenide (GaAs) based photonic crystal switch consisting of coupled cavities connected to access waveguides. All-optical switching at 5 GHz repetition rate is demonstrated using carrier-induced nonlinear processes in the cavities. The photonic crystal is passivated by Al_2O_3 in

order to enhance the nonlinear effects by increasing the carrier lifetime to 10 ps [12]. Figure 1.1(c) shows the SEM image of aluminium gallium arsenide (AlGaAs) on insulator consisting of a micro-resonator coupled with a bus waveguide, where the AlGaAs material is indicated in blue. The device exhibits high Kerr nonlinearity which enables frequency comb generation with milliwatt-level pump power [13]. Figure 1.1(d) shows the SEM image of a silicon photonic crystal nanobeam cavity side-coupled to a waveguide Fabry-Perot resonator. The system exhibits an asymmetric transmission spectrum known as the Fano resonance [14]. Figure 1.1(e) shows the SEM image of indium gallium arsenide phosphide (InGaAsP) photonic crystal switch consisting of input-output waveguides and a nanocavity. The device transmission exhibits Lorentzian lineshape. Using carrier-induced nonlinearities in the nanocavity pulse extraction and removal from a signal train at 40 GHz is demonstrated [8].

The work in this thesis fall into a similar category of the works briefly discussed in Fig. 1.1, specially to Figs. 1.1(b) [12], and 1.1(e) [8]. We have investigated an indium phosphide (InP) photonic crystal structure consisting of a nanocavity side-coupled to a waveguide. Photonic crystals are attractive due to the possibility of realizing small mode volume cavities on the order of $(\lambda/n)^3$, where λ is the wavelength of light, and n is the refractive index of the material [15]. We have chosen the InP material system because it provides opportunities for embedding semiconductor gain materials such as quantum wells and quantum dots, in addition to the standard passive layers. Here, we have used the passive InP system, i.e. without gain medium. We have further exploited carrier-induced optical nonlinear effects at telecom wavelengths. The main goal of the thesis was to investigate such structures and experimentally demonstrate a few all-optical bit-level switching applications.

1.3 Overview of the thesis

In this work, we investigated a novel photonic crystal nanocavity based structure that employ efficient carrier-induced nonlinear process for realization of energy efficient, fast, and small footprint all-optical switches. The content of this thesis is organized as follows:

Chapter 2 summarizes the theoretical background required to understand the concepts discussed in the latter chapters. It covers the fundamental concepts of electromagnetic theory, second and third order optical nonlinear effects, and the physics of photonic crystal membrane devices. In addition, types of on-off keying modulation formats, and bit-error ratio analysis of optical data signals are introduced.

Chapter 3 describes the design and fabrication of InP photonic crystal cavity and waveguide structures. Additionally, airholes based grating coupler for fiber-to-chip coupling is designed and demonstrated. The device platform consisting of

the input-output grating couplers, photonic crystal membrane section, and a wire waveguide connecting all these sections is described and its fabrication details are provided.

Chapter 4 focuses on the design and theory of the photonic crystal Fano structure, which is the main subject this work. The Fano resonance structure is explained in comparison with the commonly known Lorentzian resonance structure using coupled-mode theory. Two-types of asymmetric Fano resonances, i.e. the blue and red-parity Fano resonance lineshapes are studied. Moreover, the carrier-induced nonlinear effects in the cavity which allows the resonance shifting feature of the device are investigated. Furthermore, the study of the carrier dynamics of InP photonic crystal cavity is summarized.

Chapter 5 reports the use of the red-parity Fano resonance for carving-out short pulses from long duration input pulses. The chapter covers the basic principle of pulse carving, theoretical and experimental investigations of pulse carving using the temporal and the spectral pulse profiles, applications of pulse carving for optical time domain multiplexing, and limitations of pulse carving.

Chapter 6 focuses on the use of the red and the blue-parity Fano resonances for reshaping of optical data signals. It discusses the theoretical and experimental nonlinear power transfer functions of the red and blue-parity Fano resonances. These power transfer functions are further compared with the case of using Lorentzian resonances. Noise suppression of return-to-zero on-off keying signals is reported as well.

Chapter 7 focuses on demonstrations of all-optical switching application of blue-parity Fano resonance. The pump-probe switching model based on nonlinear coupled-mode theory is briefly described. Using the InP photonic crystal Fano resonance structure, wavelength conversion and optical time domain demultiplexing applications are presented. Furthermore, initial investigation on carrier sweep-out mechanisms is reported.

Chapter 8 summarizes the main results of this thesis and gives an outlook on further work.

Chapter 2

Theoretical background

In this chapter, we introduce the fundamental concepts, equations, and notation that will be used throughout this thesis. We start with a brief introduction to fundamental concepts of electromagnetic theory in Section 2.1, and move on to nonlinear optical effects in Section 2.2, photonic crystal slabs in Section 2.3, and optical communication systems in Section 2.4. A detailed description of all the concepts introduced here can be found in various textbooks. A particularly comprehensive presentation of classical electrodynamics is given in [16], fundamental theory of photonic crystals can be found in [17], extensive study of nonlinear optical effects in [18], and basic concepts of optical communication systems and signal processing in [19].

2.1 Electromagnetic theory

2.1.1 The macroscopic Maxwell equations

In macroscopic electrodynamics, the singular character of charges and their associated current is avoided by considering charge densities, ρ and current densities, $\mathbf{j}$ as continuous functions of space. The macroscopic Maxwell equations are [16]

$$\nabla \times \mathbf{E}(\mathbf{r},t) = -\frac{\partial \mathbf{B}(\mathbf{r},t)}{\partial t}\,, \tag{2.1}$$

$$\nabla \times \mathbf{H}(\mathbf{r},t) = \frac{\partial \mathbf{D}(\mathbf{r},t)}{\partial t} + \mathbf{j}(\mathbf{r},t)\,, \tag{2.2}$$

$$\nabla \cdot \mathbf{D}(\mathbf{r},t) = \rho(\mathbf{r},t)\,, \tag{2.3}$$

$$\nabla \cdot \mathbf{B}(\mathbf{r},t) = 0\,, \tag{2.4}$$

where $\mathbf{E}$ is the electric field, $\mathbf{H}$ is the magnetic field, $\mathbf{B}$ is the magnetic flux density, and $\mathbf{D}$ is the electric displacement field. The vector $\mathbf{r} = (x, y, z)$ defines a point

in three dimensional space. $\nabla\cdot$ and $\nabla\times$ are the divergence and curl operators, respectively.

The magnetic flux density and the electric displacement field are related to the magnetic field and the electric field, respectively by constitutive relations

$$\mathbf{B}(\mathbf{r},t) = \mu_0\mathbf{H}(\mathbf{r},t) + \mathbf{M}(\mathbf{r},t)\,, \tag{2.5}$$

$$\mathbf{D}(\mathbf{r},t) = \epsilon_0\mathbf{E}(\mathbf{r},t) + \mathbf{P}(\mathbf{r},t)\,, \tag{2.6}$$

where $\mu_0 = 4\pi \times 10^{-7}$ Henry/meter [H/m] and $\epsilon_0 = 8.85419 \times 10^{-12}$ Farad/meter [F/m] are the magnetic permeability and the electric permittivity of vacuum, respectively. $\mathbf{P}$ and $\mathbf{M}$ denote the polarization and magnetization of the medium. Throughout this thesis, unless otherwise stated, it is assumed that the medium is nonmagnetic ($\mathbf{M} = 0$).

2.1.2 Wave equation and time-harmonic fields

In free space we have $\mathbf{P} = \mathbf{M} = 0$ and $\rho = \mathbf{j} = 0$. The wave equation for $\mathbf{E}$ can be derived from Maxwell equations by applying the curl operation $\nabla\times$ to Eq. (2.1) and using the vector identity $\nabla \times (\nabla \times \mathbf{E}) = \nabla(\nabla \cdot \mathbf{E}) - \nabla^2\mathbf{E}$. A similar procedure is carried out for $\mathbf{H}$. The resulting wave equation is given by [20]:

$$\nabla^2 U - \frac{1}{c_0}\frac{\partial^2 U}{\partial t^2} = 0, \tag{2.7}$$

where $c_0 = 1/\sqrt{\epsilon_0\mu_0} = 2.99792458 \times 10^8$ m/s is the speed of light in vacuum. The scalar function, U represents any of the three components (E_x, E_y, E_z) of the $\mathbf{E}$ or (H_x, H_y, H_z) of the $\mathbf{H}$ field. A necessary condition for $\mathbf{E}$ and $\mathbf{H}$ to satisfy the Maxwell equations is that each of their components should satisfy the wave equation, Eq. (2.7). At the boundary between two homogeneous dielectric media and in the absence of free electric charges, the tangential component of the electric and magnetic fields, and the normal components of the electric displacement and magnetic flux densities must be continuous [20, 21].

When the electromagnetic wave is monochromatic, all components of the electric and magnetic fields are harmonic functions of time of the same frequency [20]. A monochromatic field can then be written as [21]

$$\mathbf{E}(\mathbf{r},t) = \frac{1}{2}\mathrm{Re}\big[E_0 e^{i(\mathbf{kr}-\omega t)} + c.c.\big]\,, \tag{2.8}$$

$$\mathbf{E}(\mathbf{r},t) = \frac{1}{2}\mathrm{Re}\big[\mathbf{E}(\mathbf{r})e^{-i\omega t} + c.c.\big]\,, \tag{2.9}$$

where $\mathbf{k}$ is the wave vector and is related to ω by the dispersion relation, $k = \frac{\omega}{c}$. A similar expression as Eq. (2.9) can be written for the $\mathbf{H}$ field as well. Substituting, $\frac{\partial}{\partial t} = -i\omega$, in the Maxwell equations (2.1) to (2.4), we obtain

$$\nabla \times \mathbf{E}(\mathbf{r}) = i\omega \mathbf{B}(\mathbf{r}) \,, \tag{2.10}$$

$$\nabla \times \mathbf{H}(\mathbf{r}) = -i\omega \mathbf{D}(\mathbf{r}) + \mathbf{j}(\mathbf{r}) \,, \tag{2.11}$$

$$\nabla \cdot \mathbf{D}(\mathbf{r}) = \rho(\mathbf{r}) \,, \tag{2.12}$$

$$\nabla \cdot \mathbf{B}(\mathbf{r}) = 0. \tag{2.13}$$

2.1.3 Polarization of dielectric media

The electric field of the optical signal oscillating at frequency ω polarizes the atoms of a medium by displacing an electron with respect to the nucleus. This creates electric dipole oscillations which can be either resonant or non-resonant with respect to one of the natural frequencies of the atom ω_0 [23]. Resonant oscillations, $\omega = \omega_0$ result in energy transfer and hence the medium absorbs the energy from light. If the ω does not coincide with any of the resonant frequencies, then the atom will not absorb the light, and hence the medium will be transparent. These non-resonant oscillations of the atoms follow the driving wave with a phase lag, causing reduction of light velocity in the medium [23].

In general, the polarization, $\mathbf{P}$ follows the electric field, $\mathbf{E}$ with a time-delay described by a convolution with a causal response function $\chi(\mathbf{r}, t)$ as

$$\mathbf{P}(\mathbf{r}, t) = \epsilon_0 \int_{-\infty}^{t} \chi(\mathbf{r}, \tau) \mathbf{E}(\mathbf{r}, t - \tau) \, \mathrm{d}\tau \,, \tag{2.14}$$

In the frequency domain, this corresponds to a multiplication with the corresponding complex transfer function $\chi(\mathbf{r}, \omega)$ as

$$\mathbf{P}(\mathbf{r}, \omega) = \epsilon_0 \chi(\mathbf{r}, \omega) \mathbf{E}(\mathbf{r}, \omega) \,, \tag{2.15}$$

where $\chi(\mathbf{r}, \omega)$ is the complex electric susceptibility. The electric field and the polarization have a cause and effect relationship in which the polarization is the response of the medium to the presence of an electric field [16]. A dielectric medium is called *linear* if $\mathbf{P}$ is linearly related to $\mathbf{E}$. If $\mathbf{E}$ and $\mathbf{P}$ are independent of the position vector $\mathbf{r}$, the medium is said to be *homogeneous*. Additionally, if the relationship between $\mathbf{E}$ and $\mathbf{P}$ is independent of the direction of the electric field $\mathbf{E}$, the medium is called *isotropic*.

If the dielectric medium is operated far away from any electronic resonances, the susceptibility term can be assumed to be real and independent of frequency. In this case, the instantaneous polarization is directly related to the electric field, neglecting any memory of the medium as

$$\mathbf{P}(\mathbf{r}, t) = \epsilon_0 \chi(\mathbf{r}) \mathbf{E}(\mathbf{r}, t) \,, \tag{2.16}$$

Inserting Eq. (2.16) into Eq. (2.6), we obtain

$$\mathbf{D}(\mathbf{r},t) = \epsilon_0(1+\chi)\mathbf{E}(\mathbf{r},t)\,,$$
$$\mathbf{D}(\mathbf{r},t) = \epsilon_0\epsilon_r(\mathbf{r})\mathbf{E}(\mathbf{r},t)\,, \tag{2.17}$$

where $\epsilon_r(\mathbf{r})$ is the relative permittivity or dielectric function. Similarly, the magnetic flux density can be written as, $\mathbf{B}(\mathbf{r},t) = \mu_0\mu_r(\mathbf{r})\mathbf{H}(\mathbf{r},t)$. The refractive index of the medium in the general case is, $n(\mathbf{r}) = \sqrt{\epsilon_r(\mathbf{r})\mu_r(\mathbf{r})}$. However, for most dielectric materials of interest the relative permeability $\mu_r(\mathbf{r})$ is close to unity and we may set, $\mathbf{B}(\mathbf{r},t) = \mu_0\mathbf{H}(\mathbf{r},t)$, for simplicity [17]. Therefore, the refractive index can be written as

$$n(\mathbf{r}) = \sqrt{\epsilon_r(\mathbf{r})}. \tag{2.18}$$

In the general case, the dielectric function is a complex function including material dispersion i.e. frequency dependence written as, $\epsilon_r(\mathbf{r},\omega)$. The complex dielectric function is given by

$$\epsilon_r(\mathbf{r},\omega) = \epsilon_1(\mathbf{r},\omega) + i\epsilon_2(\mathbf{r},\omega)\,, \qquad \epsilon_1,\epsilon_2 \in \mathbb{R}. \tag{2.19}$$

For simplicity, let us consider a homogeneous material for which the dielectric function is independent of $\mathbf{r}$. The real ($\epsilon_1(\omega)$) and imaginary ($\epsilon_2(\omega)$) parts of the dielectric function are related by the Kramers-Krönig (KK) relations as

$$\epsilon_1(\omega) - 1 = \frac{1}{\pi}\int_{-\infty}^{\infty} \frac{\epsilon_2(\omega')}{\omega' - \omega} d\omega'\,, \tag{2.20}$$

$$\epsilon_2(\omega) = -\frac{1}{\pi}\int_{-\infty}^{\infty} \frac{[\epsilon_1(\omega') - 1]}{\omega' - \omega} d\omega'. \tag{2.21}$$

This means it is sufficient to measure the real part or the imaginary part over the whole frequency spectrum and calculate the corresponding imaginary or real part of the dielectric function. In order to avoid possible divergences, the integration should stop at $\omega' = \omega - \eta$, and continue at $\omega' = \omega + \eta$, for infinitely small η. This is called the Cauchy principal value integral [18].

The rate at which energy is transported can be determined from the Poynting vector, $\mathbf{S}(\mathbf{r},t)$ as

$$\mathbf{S}(\mathbf{r},t) = \frac{1}{2}\mathrm{Re}\big[\mathbf{E}^*(\mathbf{r},t) \times \mathbf{H}(\mathbf{r},t)\big]. \tag{2.22}$$

The time-average of the poynting vector is referred to as the light intensity (I). It is given by:

$$I = |\langle \mathbf{S}(\mathbf{r},t)\rangle| = \frac{1}{2}c_0\epsilon_0 n E^2. \tag{2.23}$$

The intensity as a function of the travelled distance, z, will follow an exponentially decaying function, given by $I\exp(-\beta_0 z)$, where β_0 is the absorption coefficient of

the material which is related to the imaginary part of the refractive index. The real part of the refractive index on the other hand leads to a decrease in the propagation speed of light in the material, i.e. $c = c_0/n_0$. The complex refractive index can be written as

$$\tilde{n} = n_0 + i\kappa\,, \tag{2.24}$$

where n_0 is the real part of the refractive index and κ is the extinction coefficient representing the imaginary part of the refractive index. Note that the frequency dependence of the refractive index is neglected here for simplicity. Since the electric field, E, changes along the propagation direction following the function $\exp[i2\pi(n_o + i\kappa)z/\lambda]$, and the intensity is proportional to $|E|^2$, it can be found that the extinction ratio is related to the absorption coefficient by $\kappa = \beta_0\lambda/4\pi$ [22]. We can rewrite Eq. (2.24) as

$$\tilde{n} = n_0 + i\frac{\lambda}{4\pi}\beta_0\,, \tag{2.25}$$

where λ is the wavelength of light in the medium. The absorption coefficient, β_0, has dimension of inverse length, and it is usually expressed in the units of cm^{-1} [22].

Note that the word *polarization* is also used to denote the direction of the electric field vector, $\mathbf{E}$, in an electromagnetic wave. In this case, several types of polarization are possible such as linear, circular and elliptical. When the electric field vector points along a constant direction, the light is called linearly polarized. In this thesis, unless otherwise stated, we focus only on linear polarized light.

2.2 Nonlinear optical effects

In nonlinear optics, the relationship between the electric field and polarization is more general than that given in Eq. (2.16). For an isotropic medium, the polarization $\mathbf{P}(t)$ can be written as a power series in the electric field $\mathbf{E}(t)$ as

$$\mathbf{P}(t) = \epsilon_0\big(\chi^{(1)}\mathbf{E}(t) + \chi^{(2)}\mathbf{E}^{2}(t) + \chi^{(3)}\mathbf{E}^{3}(t) + ...\big) \tag{2.26}$$

where $\chi^{(n)}$ are the nth-order optical susceptibilities. These susceptibility terms are tensors of rank $(n+1)$ and describe the relationship between the induced polarization and the incident electric field. The first-order susceptibility term $\chi^{(1)}$ is simply the linear optical effect. It accounts for the dipole excitations of bound and free electrons induced by an incident photon. The real part of $\chi^{(1)}$ is associated with the refractive index of the material, where as the imaginary part describes gain or loss. The higher order susceptibilities give rise to a whole range of nonlinear optical effects. The majority of these phenomena can be attributed to either $\chi^{(2)}$ or $\chi^{(3)}$ terms. In the following subsections we discuss nonlinear effects associated with these coefficients.

2.2.1 Second order nonlinearities ($\chi^{(2)}$)

Consider a nonlinear medium excited by two optical fields, $\mathbf{E}_1$ and $\mathbf{E}_2$, having angular frequencies, ω_1 and ω_2, respectively. Using Eq. (2.9), we can write the total input field as

$$\mathbf{E}(t) = \mathbf{E}_1 + \mathbf{E}_2 = \frac{1}{2}\big[\mathbf{E}_{\omega_1} e^{-i\omega_1 t} + \mathbf{E}_{\omega_2} e^{-i\omega_2 t} + c.c.\big]. \tag{2.27}$$

From Eq. (2.26), the second order nonlinear polarization can be written as:

$$\mathbf{P}^{(2)}(t) = \epsilon_0 \chi^{(2)} \mathbf{E}^2(t). \tag{2.28}$$

Substituting Eq. (2.27) into Eq. (2.28) and rearranging the terms, we obtain

$$\begin{aligned}
\mathbf{P}^{(2)}(t) = {} & \frac{1}{4}\epsilon_0\chi^{(2)}\big[\mathbf{E}^2_{\omega_1} e^{-i2\omega_1 t} + c.c.\big] && \text{SHG} \\
& + \frac{1}{4}\epsilon_0\chi^{(2)}\big[\mathbf{E}^2_{\omega_2} e^{-i2\omega_2 t} + c.c.\big] && \text{SHG} \\
& + \frac{1}{2}\epsilon_0\chi^{(2)}\big[\mathbf{E}_{\omega_1}\mathbf{E}_{\omega_2} e^{-i(\omega_1+\omega_2)t} + c.c.\big] && \text{SFG} \\
& + \frac{1}{2}\epsilon_0\chi^{(2)}\big[\mathbf{E}_{\omega_1}\mathbf{E}^*_{\omega_2} e^{-i(\omega_1-\omega_2)t} + c.c.\big] && \text{DFG} \\
& + \frac{1}{2}\epsilon_0\chi^{(2)}\big[\mathbf{E}_{\omega_1}\mathbf{E}^*_{\omega_1} + \mathbf{E}_{\omega_2}\mathbf{E}^*_{\omega_2}\big] && \text{OR.}
\end{aligned} \tag{2.29}$$

The nonlinear medium radiates waves at the sum and difference frequencies of the input fields leading to the sum frequency generation (SFG) and difference frequency generation (DFG) processes. When the input frequencies are the same, i.e. $\omega_1 = \omega_2$, the sum frequency component is doubled. This effect is called frequency doubling or second-harmonic generation (SHG) since the radiated field has twice the input frequency. On the other hand, the difference frequency becomes zero. This effect is known as optical rectification (OR) which refers to the phenomenon by which a static electric field is generated from input fields at optical frequencies. The reverse of this process is the linear electro-optic effect also known as the Pockels effect [23].

The nonlinear frequency mixing process can also be performed in the opposite way i.e. an input field at frequency ω propagating through a second-order nonlinear medium can create two new photons at ω_1 and ω_2, where $\omega = \omega_1 + \omega_2$. This process is known as down conversion and can be used to amplify a weak signal through a process known as parametric amplification. In the presence of a strong pump field at frequency ω_{pump}, a weak probe signal can be amplified through the generation of an idler field at $\omega_{\text{idler}} = \omega_{\text{pump}} - \omega_{\text{probe}}$. This in turn generates more photons of the probe signal by mixing with the pump signal in a repetitive process.

For these nonlinear processes to work, the phases of the nonlinear signals generated in the nonlinear medium must be the same [18]. This ensures that conservation

of momentum is achieved in the nonlinear processes. In general, when a photon of wave vector $\mathbf{k}$ is generated by mixing two photons with wave vectors $\mathbf{k}_1$ and $\mathbf{k}_2$, the phase-matching condition requires that:

$$\mathbf{k} = \mathbf{k}_1 + \mathbf{k}_2. \tag{2.30}$$

In this case, phase matching can only be achieved if the nonlinear crystal is oriented in a very precise direction compared to the propagation direction of light, and in general crystal symmetries should also be considered. In centrosymmetric crystals such as silicon which posses inversion symmetry, the second order susceptibility terms vanish [24]. However, for non-centrosymmetric crystals which possess zinc-blende structure like indium phosphide (InP), due to the absence of inversion symmetry, non-zero second order susceptibility coefficients exist. For example, at a wavelength of 1.5 μm, InP has a nonlinear optical coefficient, $d = \epsilon_0\chi^{(2)} \approx -1.45$ pm/V [25, 26].

2.2.2 Third order nonlinearities ($\chi^{(3)}$)

Consider a nonlinear medium excited by three optical fields, $\mathbf{E}_1$, $\mathbf{E}_2$, and $\mathbf{E}_3$, having angular frequencies ω_1, ω_2, and ω_3, respectively [24]. The total field can be written using Eq. (2.9) as

$$\mathbf{E}(t) = \sum_{k=1}^{3} \mathbf{E}_k = \frac{1}{2}\sum_{k=1}^{3}\Big[\mathbf{E}_{\omega_k} e^{-i\omega_k t} + c.c.\Big]. \tag{2.31}$$

From Eq. (2.26), the third order nonlinear polarization can be written as:

$$\mathbf{P}^{(3)}(t) = \epsilon_0\chi^{(3)}\mathbf{E}^3(t). \tag{2.32}$$

Inserting Eq. (2.31) into Eq. (2.32) we obtain [24]:

$$\begin{aligned}
\mathbf{P}^{(3)}(t) = {} & \frac{3}{4}\epsilon_0\chi^{(3)}\big[|\mathbf{E}_{\omega_1}|^2\mathbf{E}_1 + \therefore\big] && \text{SPM} \\
& + \frac{6}{4}\epsilon_0\chi^{(3)}\big[(|\mathbf{E}_{\omega_2}|^2 + |\mathbf{E}_{\omega_3}|^2)\mathbf{E}_1 + \therefore\big] && \text{XPM} \\
& + \frac{1}{4}\epsilon_0\chi^{(3)}\big[(\mathbf{E}^3_{\omega_1} e^{-i3\omega_1 t} + c.c.) + \therefore\big] && \text{THG} \\
& + \frac{3}{4}\epsilon_0\chi^{(3)}\big[\frac{1}{2}\big(\mathbf{E}^2_{\omega_1}\mathbf{E}_{\omega_2} e^{-i(2\omega_1+\omega_2)t} + c.c.\big) + \therefore\big] && \text{FWM} \\
& + \frac{3}{4}\epsilon_0\chi^{(3)}\big[\frac{1}{2}\big(\mathbf{E}^2_{\omega_1}\mathbf{E}^*_{\omega_2} e^{-i(2\omega_1-\omega_2)t} + c.c.\big) + \therefore\big] && \text{FWM} \\
& + \frac{6}{4}\epsilon_0\chi^{(3)}\big[\frac{1}{2}\big(\mathbf{E}_{\omega_1}\mathbf{E}_{\omega_2}\mathbf{E}^*_{\omega_3} e^{-i(\omega_1+\omega_2-\omega_3)t} + c.c.\big) + \therefore\big] && \text{FWM} \\
& + \frac{6}{4}\epsilon_0\chi^{(3)}\big[\frac{1}{2}\big(\mathbf{E}_{\omega_1}\mathbf{E}_{\omega_2}\mathbf{E}_{\omega_3} e^{-i(\omega_1+\omega_2+\omega_3)t} + c.c.\big) + \therefore\big] && \text{FWM},
\end{aligned} \tag{2.33}$$

where the symbol $\therefore$ stands for all possible combinations of the frequencies ω_1, ω_2 and ω_3. The first term in Eq. (2.33) corresponds to self-phase modulation (SPM) which is the result of dipole excitations induced by three photons at the same angular frequency (e.g. ω_1), cf. Fig. 2.1(a). SPM is a nonlinear optical Kerr effect in which the incident wave field modulates its own phase through intensity-dependent refractive index change. Combining Eq. (2.26) and Eq. (2.6), we get

$$\mathbf{D}(t) = \epsilon_0\big(1 + \chi^{(1)} + \chi^{(2)}\mathbf{E}(t) + \chi^{(3)}\mathbf{E}^{^2}(t) + ...\big)\mathbf{E}(t)\,, \tag{2.34}$$

$$\mathbf{D}(t) = \epsilon_0\epsilon_r^{NL}\mathbf{E}(t)\,, \tag{2.35}$$

where the nonlinear relative permittivity is given by $\epsilon_r^{NL} = \epsilon_r + \Delta\epsilon$, in terms of the relative permittivity in linear regime ϵ_r, and the change in the relative permittivity induced by the nonlinear process $\Delta\epsilon$. Restricting our discussion to centrosymmetric systems, $\chi^{(2)} = 0$, and comparing with the first term of Eq. (2.33), the change in relative permittivity can be written as $\Delta\epsilon = \frac{3}{4}\chi^{(3)}|\mathbf{E}_{\omega_1}|^2$. Using Eq. (2.18) and Taylor expansion by assuming $\Delta\epsilon \ll \epsilon_r$, we may write:

$$n = (\epsilon_r + \Delta\epsilon)^{\frac{1}{2}} = \sqrt{\epsilon_r} + \frac{\Delta\epsilon}{2\sqrt{\epsilon_r}} \equiv n_0 + \Delta n. \tag{2.36}$$

The above equation can further be simplified as:

$$n = n_0 + \frac{3\chi^{(3)}E^2}{8n_0}. \tag{2.37}$$

Substituting Eq. (2.23) into the above equation, we get

$$n(I) = n_0 + n_2 I\,, \tag{2.38}$$

where n_2 is the Kerr coefficient and is given by:

$$n_2 = \frac{3\chi^{(3)}}{4c_0n_0^2\epsilon_0}. \tag{2.39}$$

This shows that the change in refractive index scales with the intensity of the input light. The phenomenon that the refractive index has the form in Eq. (2.38) is called the **optical Kerr effect**.

The second term in Eq. (2.33) represents cross-phase modulation (XPM), in which the first signal at ω_1 modulates the phase of a second signal at ω_2 or ω_3 using Kerr effect, cf. Fig. 2.1(b). The refractive index change induced by XPM is twice as large as the refractive index change induced by SPM, as can be seen from the coefficients of the respective terms in Eq. (2.33).

The third term in Eq. (2.33) represents third harmonic generation (THG), in which three photons of the same frequency, ω_1 combine to induce excitations

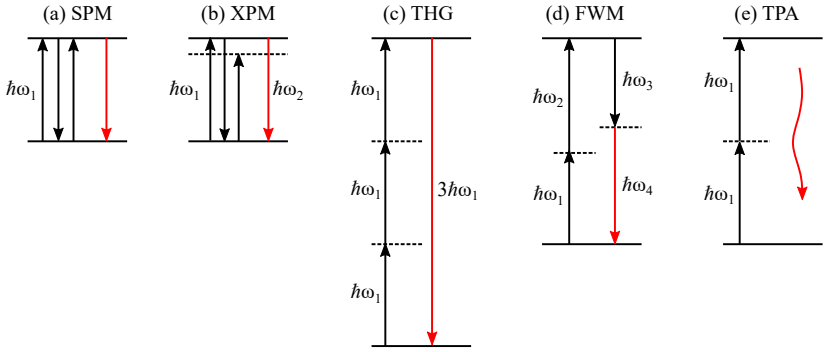

Figure 2.1: Third-order nonlinear dipole transitions and possible energy level diagrams. (a) Self-phase modulation (SPM), (b) Cross-phase modulation (XPM), (c) Third harmonic generation (THG), (d) Four-wave mixing (FWM), (e) Two-photon absorption (TPA). Input waves and output waves are illustrated in black and red arrows, respectively. The energy levels are indicated by horizontal solid lines.

leading to generation of one photon at frequency of $3\omega_1$ as shown schematically in Fig. 2.1(c).

The remaining terms in Eq. (2.33) represent the generation of new waves through four wave mixing (FWM) in which three incident photons generate a fourth photon at an idler frequency ω_4 as shown in Fig. 2.1(d). When the incident two photons are degenerate, the optical Kerr effect is known as degenerate four wave mixing (DFWM). This is an ultrafast process that alters the refractive index instantaneously as a function of the intensity of the input light. Equation 2.38 can be written in a general complex form using Eq. (2.25) as:

$$n(I) = n_0 + n_2 I + i\frac{\lambda}{4\pi}(\beta_0 + \beta_2 I)\,, \tag{2.40}$$

where $\beta_2 = \beta_{\mathrm{TPA}}$ is the two-photon absorption (TPA) coefficient. The two photons that excite an electron from the valence band to the conduction band in the DFWM process can also lead to absorbing excitations which generate free carriers in the conduction band. This process is known as **two-photon absorption**, cf Fig. 2.1(e). The density of free-carriers produced by TPA is given by [27]:

$$N = \tau\frac{\beta_{\mathrm{TPA}} I^2}{2\hbar\omega}\,, \tag{2.41}$$

where τ is the carrier recombination lifetime. The lifetime of these free electrons in the conduction band determines the speed of photonic devices which exploit Kerr effects [24]. A figure of merit (FoM) is often defined to compare the magnitude of the Kerr coefficient (n_2) to the strength of the TPA coefficient β_{TPA} [24]:

$$\mathrm{FoM} = \frac{1}{\lambda}\frac{n_2}{\beta_{\mathrm{TPA}}}. \tag{2.42}$$

In order to avoid TPA-related speed limitations, a material with a large Kerr nonlinear coefficient and a small TPA coefficient is often desired. From Table 2.1, it can be inferred that InP based devices have lower performance as optical Kerr effect based modulators. On the other hand, exploiting the large TPA coefficient, carrier-induced nonlinearities can be suitable for realization of InP based all-optical devices [28].

Table 2.1: Comparison of commonly used semiconductor materials in terms of Kerr and TPA coefficients. The FoM indicates the efficiency of the device as Kerr effect all-optical modulator around 1.55 μm.

Material	Kerr coefficient (n_2) [$\times 10^{-17}\,\mathrm{m^2/W}$]	TPA Coefficient (β_{TPA}) [cm/GW]	FoM	Ref.
Si	0.45 ± 0.15	0.8	0.37	[29, 30]
GaAs	1.6	10.2	0.1	[30]
InP	3 ± 1.5	24	0.08	[31, 32]
AlGaAs	3.8	0.4	6	[33]

2.2.3 Free-carrier-induced nonlinearities

Carrier-induced third-order optical nonlinearities in direct band gap semiconductors are caused by the promotion of carriers from their equilibrium states to other states, introducing changes to the complex dielectric function [34]. Such processes involve excitation of carriers, i.e. a flow of energy from the incident light to the nonlinear medium. These transitions can be divided into three separate processes [35]. Firstly, the direct and indirect transitions from the valence band to conduction band. Secondly, the free-carrier intraband transition, and the final process is the intervalence band transition. For simplicity, we skip the intervalence band absorption which is difficult to estimate, but accounts for no more than 10 to 20 percent of the refractive index change induced by the intraband transitions [28]. The first process, i.e. the transition from the valence band to the conduction band in InP material systems with bandgap of $E_{\mathrm{g}} = 1.34\,\mathrm{eV}$, operating at telecom wavelength of around $1.55\,\mu$m, or $0.8\,\mathrm{eV}$, is only possible through TPA processes described above. This generates free-carrier concentration in the valence and conduction bands.

These accumulated free-carriers give rise to a change in the complex refractive index via three main nonlinear processes: band-filling effects, band-gap shrinkage and free-carrier absorption (FCA) [28].

Free-carrier absorption (FCA)

A free electron can absorb a photon and move to a higher energy state within the conduction band. This intraband free carrier absorption can be described using the Drude model [28]. The equation of motion for a free-electron of charge e and mass m_e driven by a monochromatic light of angular frequency ω can be written as

$$m_e(\ddot{x} + \gamma\dot{x}) = -eE_0e^{-i\omega t}\,, \tag{2.43}$$

where γ is the damping rate and E_0 is the amplitude of the incident light. The terms on the left hand side represent acceleration of the electron and the frictional damping force of the medium. The term on the right hand side is the driving force due to the incident light wave. We look for solutions of the form $x(t) = x_0e^{-i\omega t}$. This gives

$$x_0 = \frac{eE_0}{m_e}\frac{1}{\omega^2 + i\gamma\omega}\,. \tag{2.44}$$

The displacement of electrons from their equilibrium position produces a time varying dipole moment $p(t) = -ex(t)$. For N number of electrons per unit volume, the induced polarization is given by $P(t) = -Nex(t)$. Substituting this into Eq. (2.16), we obtain

$$\chi = -\frac{Ne^2}{m_e\epsilon_0}\frac{1}{\omega^2 + i\gamma\omega}\,. \tag{2.45}$$

The complex dielectric function using Eq. (2.17) becomes:

$$\epsilon_r(\omega) = 1 - \left(\frac{Ne^2}{m_e\epsilon_0}\right)\frac{1}{\omega(\omega + i\gamma)}\,. \tag{2.46}$$

Using Eq. (2.19), the real and the imaginary parts of the dielectric function can be written as

$$\epsilon_1(\omega) = 1 - \frac{\omega_p^2}{\omega^2 + \gamma^2}\,. \tag{2.47}$$

$$\epsilon_2(\omega) = \frac{\gamma\omega_p^2}{\omega(\omega^2 + \gamma^2)}\,, \tag{2.48}$$

where $\omega_p^2 = Ne^2/m_e\epsilon_0$ is the plasma frequency. In the case of weak damping limit ($\gamma = 0$), using the relation $2\Delta n = \Delta\epsilon$ from Eq. (2.36), we can obtain the change in the refractive index as:

$$\Delta n = -\frac{Ne^2\lambda^2}{8\pi^2 n\epsilon_0 c_0^2 m_e}\,, \tag{2.49}$$

where λ is the wavelength of the incident light. This change in refractive index due to free-electrons is known as **plasma dispersion**. Note that the sign of Δn is always negative and it is proportional to the carrier concentration and the square of the wavelength of incident light. This change is opposite to the refractive index change, $n_2 I$, resulting from the Kerr effect discussed in the previous section. A similar effect can be observed for holes in the valence band. However, due to the much larger effective mass of holes relative to that of electrons, we have neglected it [36].

Band-filling effects

A decrease in absorption for photon energies slightly above the fundamental band gap can be observed for several semiconductors when they are doped or when a large number of free-carriers are generated through optical excitations. With the lowest energy states in the conduction band filled, electrons from the valence band require energies greater than the fundamental bandgap to be optically excited into the conduction band. Therefore, there is a decrease in the absorption coefficient at energies above the bandgap. This phenomena is known as the **Moss-Burstein shift** or the band-filling effect [28].

The transition rate for absorption of a photon of energy $\hbar\omega$ larger than the band-gap energy, i.e. $\hbar\omega > E_{\mathrm{g}}$, is given by Fermi's golden rule as [23]

$$W_{i-f} = \frac{2\pi}{\hbar}|M|^2 g(\hbar\omega)\,, \tag{2.50}$$

where M is the matrix element given by $M = \langle f|\, H^{'}\, |i\rangle$ and $g(\hbar\omega)$ is the density of states (DoS). $H^{'}$ is the perturbation associated with the photon. The matrix element describes the effect of the external perturbation caused by the incident photon for exciting an electron from its initial state, i, to a final state, f. The DoS describes the distribution of states within the bands.

Using Eq. (2.50) the optical absorption near the bandgap of a direct-gap intrinsic semiconductor is given by [28]:

$$\alpha_0(\hbar\omega) = \frac{C}{\hbar\omega}\sqrt{\hbar\omega - E_{\mathrm{g}}}\,, \tag{2.51}$$

where C is a constant involving material parameters, matrix elements, and fundamental constants [28]. When free-carriers are present, there is a finite probability that a state in the conduction band will be occupied by an electron and a state in the valence band will be empty. If we denote an energy in the valence band by E_v and an energy in the conduction band by E_c, then the absorption can be written as:

$$\alpha(N, \hbar\omega) = \alpha_0(\hbar\omega)[f_v(E_v) - f_c(E_c)]\,, \tag{2.52}$$

where $f_c(E_c)$ is the probability of a conduction band state of energy E_c being occupied by an electron, and $f_v(E_v)$ is the probability of a valence band state of energy E_v being occupied by an electron. The probabilities f_v and f_c are the Fermi Dirac distribution [28]. The optical absorption can now be written as:

$$\alpha(N, \hbar\omega) = \alpha_0(\hbar\omega) + \Delta\alpha(N, \hbar\omega)\,, \tag{2.53}$$

where $\Delta\alpha(N, \hbar\omega)$ is the band-filling induced change in absorption. By combining Eq. 2.52 and Eq. (2.51), we get

$$\Delta\alpha(N, \hbar\omega) = \frac{C}{\hbar\omega}\sqrt{\hbar\omega - E_g}\Big[f_v(E_v) - f_c(E_c) - 1\Big]\,. \tag{2.54}$$

For intrinsic semiconductors with no optical excitation, the change in absorption, $\Delta\alpha(N, \hbar\omega)$ vanishes because $f_v(E_v)$ is nearly one and $f_c(E_c)$ is nearly zero. However, when free-carriers are present, $f_v(E_v)$ becomes smaller than one and $f_c(E_c)$ becomes larger than zero. This results in a net decrease in the absorption coefficient according to Eq. (2.54). Using the KK relations of Eq. (2.21), the change in the real part of the refractive index $\Delta n(N, \hbar\omega)$ can be calculated from Eq. (2.54). In analogy with Eq. (2.53), we can define

$$n(N, \hbar\omega) = n_0(\hbar\omega) + \Delta n(N, \hbar\omega)\,. \tag{2.55}$$

Note also that the change in refractive index induced by band-filling effects is negative following the decrease in the absorption.

Bandgap Shrinkage

As discussed above, the generated free-electrons will occupy states at the bottom of the conduction band. If the concentration is large enough, the electron wave functions will overlap forming a gas of interacting particles [28]. The electrons will repel each other by Coulomb forces resulting in screening of electrons and hence lowering the energy of conduction band edge by [28]

$$\Delta E_{\mathrm{g}}(N) = -\frac{e}{2\pi\epsilon_0\epsilon_r}\left(\frac{3}{\pi}\right)^{\frac{1}{3}} N^{\frac{1}{3}}\,. \tag{2.56}$$

The estimated bandgap shrinkage is proportional to the cube-root of the carrier concentration. Using Eq. (2.51) and Eq. (2.53), the change in absorption due to bandgap shrinkage is predicted to be [28]:

$$\Delta\alpha(N, \hbar\omega) = \frac{C}{\hbar\omega}\sqrt{\hbar\omega - E_{\mathrm{g}} - \Delta E_{\mathrm{g}}(N)} - \frac{C}{\hbar\omega}\sqrt{\hbar\omega - E_{\mathrm{g}}}\,. \tag{2.57}$$

As can be seen from Eq. (2.57), the change in the absorption coefficient and hence the change in refractive index is positive for carrier concentrations larger

than a critical concentration level. In fact, bandgap shrinkage partly compensates the change in refractive index induced by band-filling effects.

For our material of choice, InP, operating around the telecom wavelength ($1.55\,\mu$m), free-carrier absorption and band-filling effects are much stronger than bandgap shrinkage effects as shown in Fig. A.1(a). Note that band-filling effects and bandgap shrinkage based changes in refractive indices are stronger for photon energies closer to the bandgap, cf. Fig. A.1(a).

2.2.4 Thermo-optic effects

Another contribution to the change in the refractive index of optical devices comes from the temperature dependent refractive index. The TPA and FCA effects discussed above not only induce transition of electrons from their initial state to the final state, but also contribute to the kinetic energy of the electrons hence thermal energy [27, 36]. Thermal effects can be described mathematically as [18]:

$$n = n_0 + n_T \Delta T\,, \tag{2.58}$$

where the quantity $n_T = dn/dT$ describes the temperature dependence of the refractive index. For InP around $1.55\,\mu$m a value of $n_T = 2.01 \times 10^{-4}\,\mathrm{K}^{-1}$ have been reported at room temperature [37]. We assume that the induced change in temperature ΔT is a function of space and time, i.e. $\Delta T(x, y, z, t)$, and obeys the heat-transport equation [18]:

$$\rho_0 C \frac{\partial \Delta T}{\partial t} - \kappa \nabla^2 \Delta T = q_T\,, \tag{2.59}$$

where ρ_0 denotes the material density, C is heat capacity per unit mass, κ denotes thermal conductivity of the material, and q_T is the heat source term in units of $\mathrm{W/m^3}$. The Laplace operator is the divergence of the gradient of a function f, given by $\Delta f = \nabla^2 f = \nabla \cdot \nabla f$. Equation (2.59) can be solved as a boundary value problem. The response time, τ, associated with the change in temperature can then be calculated which is the measure of the time taken for the temperature distribution to reach its new steady state after excitation by an input light beam.

In Chapter 4, we further discuss the interplay of these nonlinear effects which provide enabling features to the photonic devices investigated in this thesis.

2.3 Photonic crystal slabs

Photonic crystals are a broad class of artificial materials that exploit scattering and resonance in periodically patterned structures to control propagation of electromagnetic energy. The pattern with which these arrangements are repeated in space is called the crystal lattice. In much the same way as ionic lattices affect the motion of electrons in solids, photonic crystals affect the motion of photons [17].

It can have 1, 2 or 3D periodicity. The discussion in this section is based on the book by Joannopoulos et al. [17].

We start by restricting our discussion to linear and lossless materials which are simpler and provide excellent foundations suitable for the scope of this thesis. Additionally, we have assumed that the dielectric medium is transparent which means that we treat $\epsilon_r(\mathbf{r})$ as being positive and independent of frequency. Therefore, the divergence Maxwell equations, Eqs. (2.12) and (2.13), can be written as

$$\begin{aligned} \nabla \cdot \mathbf{H}(\mathbf{r}) &= 0\,, \\ \nabla \cdot [\epsilon_r(\mathbf{r})\mathbf{E}(\mathbf{r})] &= 0\,. \end{aligned} \tag{2.60}$$

Equation 2.60 requires that the field configurations follow transverse electromagnetic mode of propagation where the electric and magnetic fields are all restricted to directions normal to the direction of propagation [17]. The curl Maxwell equations, Eqs. (2.10) and (2.11), can be written as

$$\begin{aligned} \nabla \times \mathbf{E}(\mathbf{r}) - i\omega\mu_0\mathbf{H}(\mathbf{r}) &= 0\,, \\ \nabla \times \mathbf{H}(\mathbf{r}) + i\omega\epsilon_0\epsilon_r(\mathbf{r})\mathbf{E}(\mathbf{r}) &= 0\,. \end{aligned} \tag{2.61}$$

A master equation entirely in $\mathbf{H}(\mathbf{r})$ can be written in the form of an eigenvalue problem using Eq. (2.61) as [17]

$$\nabla \times \left(\frac{1}{\epsilon_r(\mathbf{r})} \nabla \times \mathbf{H}(\mathbf{r}) \right) = \left(\frac{\omega}{c_0} \right)^2 \mathbf{H}(\mathbf{r})\,. \tag{2.62}$$

Here, the strategy is that for a given structure defined by $\epsilon_r(\mathbf{r})$, we solve the master equation (2.62) to find the modes of $\mathbf{H}(\mathbf{r})$ and the corresponding frequencies subject to transversality requirement, Eq. (2.60). The second equation from Eq. (2.61) can be used to calculate $\mathbf{E}(\mathbf{r})$.

Much can be inferred about the behaviour of a photonic crystal just from knowing the symmetry of the structure. Here, we are interested in investigating structures with 2D periodicity but having a finite thickness known as photonic crystal slabs. Figure 2.2 shows such a membrane structure composed of hexagonally (or triangularly) arranged airholes suspended in air. Even though 3D photonic crystal that can confine light in all three directions is desired, the actual fabrication of such structures still remains difficult. Nevertheless, hybrid systems such as photonic crystal slabs, which uses in-plane 2D periodicity combined with vertical index-guiding can easily be fabricated to confine light in all the three dimensions. The vertical confinement, or index guiding, is due to total internal reflection. Light rays within the slab (higher refractive index) that strike the interface with air (lower refractive index) at an incident angle smaller than the critical angle are totally reflected and remain confined to the slab. These type of photonic crystals are sometimes termed as quasi-3D structures [17].

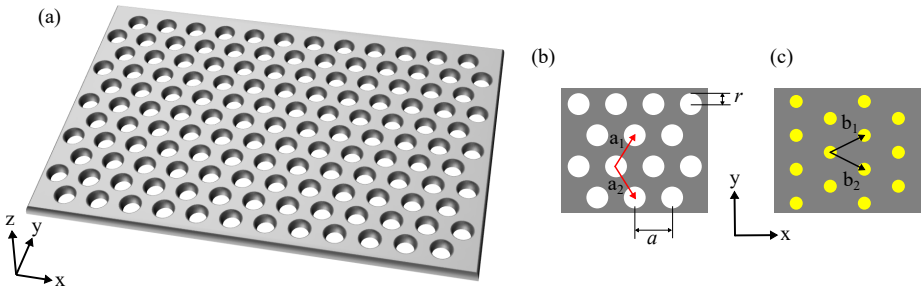

Figure 2.2: (a) Photonic crystal dielectric slab with hexagonal lattice of airholes having two-dimensional periodicity (in the xy direction) and index-guiding in the vertical (in the z direction). (b) A top view of the hexagonal lattice indicating the network of lattice points in real space with the primitive lattice vectors $\mathbf{a}_1 = a(\hat{\mathbf{x}} + \hat{\mathbf{y}}\sqrt{3})/2$, and $\mathbf{a}_2 = a(\hat{\mathbf{x}} - \hat{\mathbf{y}}\sqrt{3})/2$. The structure has a lattice constant of a and the radius of the airholes is r. (c) The corresponding reciprocal lattice in k-space with the reciprocal lattice vectors $\mathbf{b}_1 = (2\pi/a)(\hat{\mathbf{x}} + \hat{\mathbf{y}}/\sqrt{3})$, and $\mathbf{b}_2 = (2\pi/a)(\hat{\mathbf{x}} - \hat{\mathbf{y}}/\sqrt{3})$.

Let us now introduce briefly the concepts of unit cells, primitive lattice vectors, reciprocal lattice vectors, Bloch modes, and Brillouin zone. These concepts are then used to explain the physics of photonic crystals. A unit cell is the smallest group of dielectric material arrangement which has the overall symmetry of the crystal and from which the entire lattice can be built up by repetition, cf. Fig. 2.3(b). The primitive axis vectors ($\mathbf{a}_1$ and $\mathbf{a}_2$) point along the edges of a unit cell in the direction of the lattice axes as shown in Fig. 2.2(b). The magnitude of these vectors is called the lattice constant (a). Primitive axis vectors describe the size and the orientation of the crystal in the unit cell but do not completely describe the symmetry. For this purpose, reciprocal lattices are often used. As with primitive vectors which connect direct lattice (*real* space) points, reciprocal vectors connect reciprocal lattice points in the unit cell. Reciprocal space is often called "k-space" and it is often preferred to analyse photonic crystals because of the elegant relation between wave vectors and lattice vectors. Wave vectors and lattice vectors both have a magnitude equal to 2π divided by a length.

In a periodic medium, having discrete translational symmetry, the propagation of electromagnetic waves is modulated by a periodic envelope function having the same periodicity as the crystal [17]. This is known as the Bloch-Floquet theorem which states that solutions to the eigenvalue problem of Eq. (2.62) can take the Bloch form

$$\mathbf{H}(\mathbf{r}) = \mathbf{u}_{\mathbf{k}}(\mathbf{r}) \exp(i\mathbf{k} \cdot \mathbf{r}) = \mathbf{u}_{\mathbf{k}}(\mathbf{r} + \mathbf{R}) \exp(i\mathbf{k} \cdot \mathbf{r}) \,, \tag{2.63}$$

with eigenvalues or Bloch modes of $\omega_n(\mathbf{k})$. In Eq. (2.63), $\mathbf{u_k}(\mathbf{r})$ is a periodic function on the lattice: $\mathbf{u_k}(\mathbf{r}) = \mathbf{u_k}(\mathbf{r} + \mathbf{R})$, where the $\mathbf{R}$ lattice vector can be expressed as any linear combination of the primitive lattice vectors. An important feature of the Bloch states is that different values of $\mathbf{k}$ do not necessarily lead to different modes. Specifically, a mode with wave vector $\mathbf{k}$ and a mode with wave vector $\mathbf{k} + \mathbf{G}$ are the same mode if $\mathbf{G}$ is a reciprocal lattice vector. This means that there is a redundancy in $\mathbf{k}$ which can be reduced to what is called the first Brillouin zone, shown by the hexagonal shape in Fig. 2.3(c).

Due to rotational symmetry in the Brillouin zone, there is redundancy (degeneracy) in eigen modes, $\omega_n(\mathbf{k})$. Therefore, the problem can further be reduced by eliminating these redundant regions which results in the smallest area called the irreducible Brillouin zone (IBZ), shown by the triangular wedge in Fig. 2.3(c).

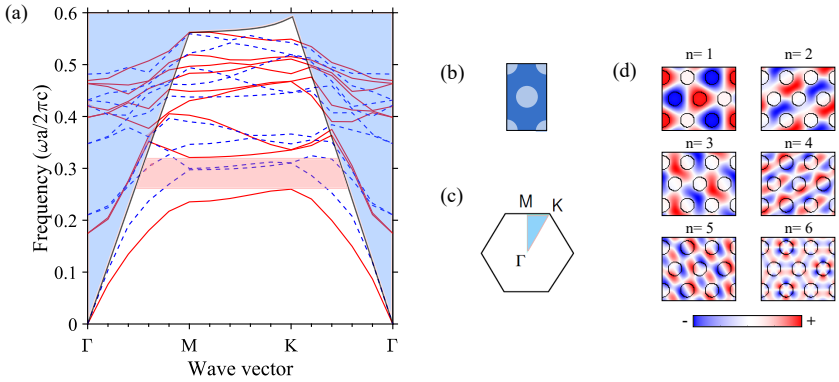

Figure 2.3: (a) Band structure of a hexagonal photonic crystal slab of airholes ($\epsilon_r = 1$) in dielectric ($\epsilon_r = 10.0489$). TE-like modes are shown in red lines while TM-like modes are indicated in dashed blue lines. (b) A unit cell of the hexagonal lattice. (c) The first Brillouin zone, hexagonal shape and the irreducable Brillouin zone (IBZ), shaded region. (d) Magnetic fields at the K-point of TE-like modes of the photonic crystal slab. The position of the airholes are indicated by the black circles and the colors indicates the amplitude of the magnetic field.

We start by describing the electromagnetic modes supported by the crystal. These modes can be written in the Block form as

$$\mathbf{H}_{(n,k_z,\mathbf{k}_{||})}(\mathbf{r}) = e^{i\mathbf{k}_{||}\cdot\boldsymbol{\rho}} e^{ik_z z} \mathbf{u}_{(n,k_z,\mathbf{k}_{||})}(\boldsymbol{\rho})\,, \tag{2.64}$$

where $\boldsymbol{\rho}$ is the projection of $\mathbf{r}$ in the xy plane and $\mathbf{u}(\boldsymbol{\rho})$ is a Bloch function, $\mathbf{u}(\boldsymbol{\rho}) = \mathbf{u}(\boldsymbol{\rho} + \mathbf{R})$, in which $\mathbf{R}$ is any linear combination of the primitive lattice vectors, $\mathbf{a}_1$

and $\mathbf{a}_2$, as shown in Fig. 2.2. The band number, n, denotes the modes in the order of increasing frequency. With discrete translational symmetry in two directions, the in-plane Bloch wave vector $\mathbf{k}_{||} = (k_x, k_y)$ is conserved while k_z is not conserved. By applying Bloch's theorem, we can focus our attention on the values of $\mathbf{k}_{||}$ that are in the Brillouin zone.

Here we restrict our discussion to the in-plane propagation case where $k_z = 0$. Additionally, the structure in Fig. 2.2 is symmetric under the mirror plane $z = 0$, i.e. the mid-plane of the slab. This allows us to classify the modes into even and odd modes. Exactly at the mirror plane, these even and odd modes are purely transverse electric (TE) and transverse magnetic (TM) polarized, respectively. TE modes have $\mathbf{H}$ normal to the plane and $\mathbf{E}$ in the plane while TM modes have $\mathbf{E}$ normal to the plane and $\mathbf{H}$ in the plane direction. If we look away from the mirror plane, then by continuity the fields should be *mostly* TE-like and TM-like, as long as the slab thickness is smaller than the wavelength [17]. In order to keep this symmetry, the slab is preferred to be a suspended membrane structure so that TE/TM-like modes can be considered separately. Otherwise, the symmetry is broken with the presence of an asymmetric substrate.

If we make a plot of the in-plane wave vector ($\mathbf{k}_{||}$) versus mode frequency for the structure, the different bands correspond to different lines that rise uniformly in frequency. This is called the band structure or band diagram or dispersion relation, shown in Fig. 2.3. It is computed by solving the master equation (2.62). It is usually enough to calculate the eigen frequencies along the special symmetry points of the IBZ where the maxima and minima of a band usually occurs. The three special points in the IBZ are Γ, M, and K and correspond to $\mathbf{k}_{||} = 0$, $\mathbf{k}_{||} = \hat{\mathbf{y}}/\sqrt{3}$, and $\mathbf{k}_{||} = \hat{\mathbf{x}}/3 + \hat{\mathbf{y}}/\sqrt{3}$, respectively, in units of $2\pi/a$. It can be seen from Fig. 2.3 that there is a gap in the band structure where no electromagnetic modes are allowed to propagate. This means that no purely real wave vector exists for any mode in that frequency range. Instead, the wave vector is complex and the wave evanescently decays into the crystal. This frequency range is known as the photonic band gap.

The structure should be optimized for maximum band gap by iterating through a range of r/a values for which a is in the order of the wavelength of light in the dielectric medium. Even though r/a values around 0.45 give larger band gaps for TE-like modes, one has to consider the limitations in fabrications such that these large airholes could be connected to each other during various lithography and etching processes. For our devices, we have found that the optimum radius to lattice constant ratio is around $r/a = 0.28$.

Consider the magnetic field distributions for bands, n= 1 and n=2, at the K-point of the TE-like modes shown in Fig. 2.3(d). These bands corresponds to the bands above (n=2) and below (n=1) the bandgap (shaded region) in Fig. 2.3(a). The white regions in Fig. 2.3(d) are locations where the electric-field energy is concentrated, i.e. along the nodal planes of the magnetic field. The

n=1 band is concentrated within the dielectric material, while the n=2 band is concentrated in air. Due to this, the former is known as the dielectric band while the latter is called the air band. According to the electromagnetic variational theorem, the field concentrated at higher-ϵ regions lies at a lower frequency, while the field concentrated at lower-ϵ regions lies at a higher frequency. This opposite shifting of the bands creates a bandgap. The band gap for our photonic crystal is shown by the shaded red in Fig. 2.3(a). Generally, the larger the dielectric contrast the larger the band gap. A useful measure of the size of the band gap is the gap-midgap ratio, $\Delta\omega/\omega_m$ which is calculated to be 28% for our design. Also note that our choice of hexagonal lattice of airholes over that of the square lattice of airholes is simply because the former gives maximum opening of the photonic band gap.

A primary difference between the case of a 2D slab and that of a truly 2D photonic crystal, infinite in z direction, is that the band diagram of the slab has a light cone, the shaded region in Fig. 2.3, which indicates the extended states in air at every ω. The presence of these extended modes means that if the translational symmetry is completely broken, then vertical radiation losses are inevitable. A secondary difference is that a complete photonic band gap, for both even and odd modes, does not exist in the case of 2D slab.

Ideal slab thickness is approximately half the wavelength of light which is thick enough for the fundamental mode to be well confined, but thin enough to prevent higher-order modes from fitting within the slab. Here, the wavelength of light in the effective medium is considered. The calculation of the effective dielectric constant depends on the spatial dielectric profile and the field mode profile which in turn depends on polarization. Therefore, the optimal slab thickness is strongly related to polarization. For supporting TE-like modes in the slab of airholes, smaller slab thickness is enough compared to that of supporting TM-like modes at the same wavelength [17]. In our case, we have used slab thickness of $\sim 340\,\text{nm}$ for devices operating at 1550 nm.

In chapter 3, we will extend these basic concepts to discuss the design and realizations of waveguides and cavities in the photonic crystal membrane structure by introducing defects into the band gaps.

2.4 Optical communication systems

In the following subsections, we briefly describe some of the basic optical communication terms that are frequently used throughout this thesis. These include on-off keying (OOK) binary modulation, non-return-to-zero (NRZ) and return-to-zero (RZ) modulation formats, bit-error ratio (BER) and extinction ratio (ER).

2.4.1 On-off keying (OOK) modulation

The term OOK modulation refers to the process of converting a particular input data, sequence of 0 and 1 bits, into patterns of signals with and without amplitude. Two of the commonly used OOK modulation formats are NRZ and RZ. In both formats a 0 bit is represented by low signal level while a 1 bit is represented by high signal level. In NRZ-OOK format, a string of consecutive 1s or 0s is represented by no signal level change. On the other hand, a signal in RZ-OOK format occupies only a certain percentage of the bit slot as illustrated in Fig. 2.4. Commonly used duty cycles for RZ-OOK are 33%, 50% and 67%.

The NRZ-OOK format can be generated in two methods. The first method is by directly modulating a laser diode while the other method is by externally modulating a continuous wave (CW) laser. At bit rates of 5 Gbit/s or higher, frequency chirp due to direct modulation becomes large enough that it results in signal distortion [19]. For higher speed operation, external modulation of a constantly biased CW laser is often implemented.

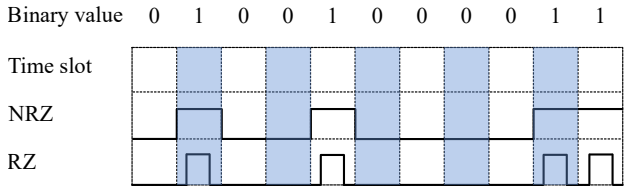

Figure 2.4: Comparison between return-to-zero (RZ) and non-return-to-zero (NRZ) modulation types.

The commonly used technique for generating RZ-OOK format is to start from a CW laser and encode input data first into the NRZ format and then using a second modulator to carve RZ signal out of the NRZ signal [19]. Alternatively, one could start with pulsed laser source and modulate the input data using only one modulator to generate RZ-OOK signal. This is the method that we have used frequently for most of the work presented in this thesis.

RZ-OOK modulation format has several advantages over NRZ-OOK signals due to improved receiver sensitivity, less inter-symbol interference, and lower average power [2, 38]. On the other hand, NRZ format occupies smaller signal bandwidth due to fewer on-off transitions [19].

2.4.2 Bit-error ratio (BER)

Bit-error ratio (BER) is a commonly used performance metric which describes the ratio of the number of errors occurred to the total number of transferred bits

[39]. A BER value of, for example, 10^{-9} indicates the probability of detecting 1 erroneous bit out of 10^9 bits. This BER value of 10^{-9} is referred to as *error-free* value throughout this thesis. BER is defined as [19]:

$$\text{BER} = P(0)P(1|0) + P(1)P(0|1)\,, \tag{2.65}$$

where $P(0)$ and $P(1)$ are the probabilities of receiving bits 0 and 1, respectively, $P(0|1)$ is the probability of deciding 0 when 1 is received, and $P(1|0)$ is the probability of deciding 1 when 0 is received. Since 1 and 0 bits are equally likely to occur, $P(0) = P(1) = 1/2$. In terms of complementary error function (erfc), BER can be written using Eq. (2.65) as [19]

$$\text{BER} = \frac{1}{4}\Big[\text{erfc}\Big(\frac{I_1 - I_D}{\sigma_1\sqrt{2}}\Big) + \text{erfc}\Big(\frac{I_D - I_0}{\sigma_0\sqrt{2}}\Big)\Big]\,, \tag{2.66}$$

where σ_0^2 and σ_1^2 are the noise variances for bits 0 and 1 respectively. I_0 and I_1 are the average value of the photocurrent for bits 0 and 1 respectively. I_D is the decision threshold current. In deriving Eq. (2.66), the probability density functions are assumed to have Gaussian distribution. Figure 2.5(a) shows a schematics of received fluctuating signal which is sampled at a decision instant, t_D. The BER can be written in terms of Q-factor as [19]

$$\text{BER} = \frac{1}{2}\text{erfc}\Big(\frac{Q}{\sqrt{2}}\Big) \approx \frac{\exp(-Q^2/2)}{Q\sqrt{2\pi}}\,. \tag{2.67}$$

By increasing the Q-factor the BER can be reduced. The Q-factor is given by:

$$Q = \frac{I_1 - I_0}{\sigma_1 - \sigma_0}\,. \tag{2.68}$$

The Q-factor is a measure which indicates the minimum signal-to-noise (SNR) required to obtain a specific BER for a given signal. Note that our notation Q-factor here should not be confused with the quality factor (Q-factor) of a cavity that we used throughout this thesis.

The effect of any signal impairment is to increase the overlap between the probability density functions by making them wider or by moving them closer together, and hence increase the BER. Another measure of the separation of the signal levels is the extinction ratio (ER). It is defined as the average received power ratio between logical bits '1' and '0'. The larger the ER, the better the signal quality. It is usually expressed in dB scale. In Chapter 6, we will discuss signal regenerators which help to counteract signal degradation by *cleaning-up* the signal hence keeping the BER low.

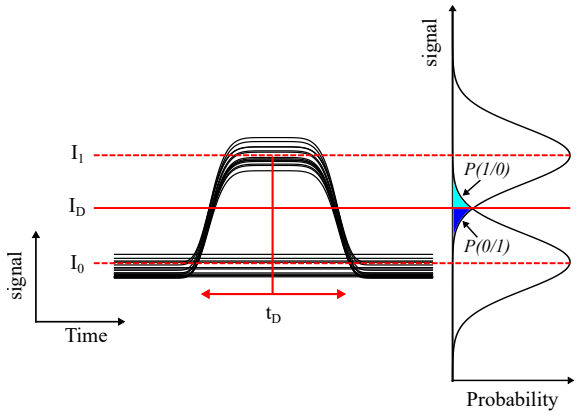

Figure 2.5: Eye diagram of received signal (left). Gaussian probability density distributions of '1' and '0' bits (right). Decision current and decision time are denoted by I_D and t_D, respectively.

Chapter 3

Device design and fabrication

This chapter describes the device platform investigated in this thesis. Particularly, the indium phosphide photonic crystal (PhC) platform incorporating nanocavities, waveguides and grating couplers. The design and rationale of using these device components as well as their fabrication processes are explained.

3.1 Photonic crystal device platform

In chapter 2 section 2.3, we discussed that no modes are allowed to exist within the photonic crystal band gap. In this section, we discuss the creation of localized modes that have frequencies within the gap by introducing defects or perturbations in the photonic crystal lattice. We have considered two types of defects, namely point-defect and linear line-defect.

3.1.1 Point-defect cavities

By removing a single airhole or simply shifting a few airholes, it is possible to create a point defect in the photonic crystal slab to form a cavity [17]. If the cavity has the proper size to support a mode, then the mode will be confined in the band gap. In this work, we have investigated *H0*-defect type which are suitable for achieving small mode volumes [15]. Figure 3.1(a) shows the shifting of the airholes to form the cavity. The H_z field profile of the resonant mode around the cavity is shown in Fig. 3.1(b).

The energy storage capacity and its dissipation rate in optical cavities is often quantified by the quality-factor (Q-factor) which is defined as

$$Q = \frac{\omega_0}{\Delta\omega} = \omega_0 \tau_p \,, \tag{3.1}$$

where ω_0 is the angular resonance frequency ($\omega_0 = 2\pi f_0$), f_0 is the resonance frequency, τ_p is the photon life time in the cavity, and $\Delta\omega$ is the full width at half

maximum (FWHM) of the resonance intensity spectrum. The time-domain signal of the resonant field is described by $E(t) = E_0(t)\exp[-(i\omega_0 + \gamma)t]$, where γ is the decay rate. The resonant field in the frequency domain, $E(\omega)$ can be obtained by taking the Fourier transform of $E(t)$. The absolute square of $E(\omega)$ can be written as

$$|E(\omega)|^2 = \frac{1}{\gamma^2 + (\omega - \omega_0)^2}\,. \tag{3.2}$$

At resonance, i.e. $\omega = \omega_0$, we find that $|E(\omega)|^2$ attains its maximum value of $1/\gamma^2$. We can also determine the frequencies at which the half maximum values occur by using Eq. (3.2) as

$$\frac{1}{2\gamma^2} = \frac{1}{\gamma^2 + (\omega - \omega_0)^2}. \tag{3.3}$$

After simplifying Eq. (3.3), we get $\omega = \omega_0 \pm \gamma$. For Lorentzian lineshape, as given in Eq. (3.2), the FWHM is therefore $\Delta\omega = 2\gamma$. The FWHM of the resonance is also known as the linewidth of the resonance spectrum. Substituting this result into Eq. (3.1) and solving for γ gives

$$\gamma = \frac{\omega_0}{2Q}. \tag{3.4}$$

The Q-factor is a dimensionless quantity and is defined as the number of optical periods that elapse before the energy in the cavity decays by $e^{-2\pi}$ [17].

This decay rate indicates the rate of energy decay in the out-of-plane direction of the photonic crystal nanocavity since the mode is confined in the in-plane direction by the photonic band gap. Hence, it is called intrinsic decay rate (γ_{in}) and the corresponding Q-factor is referred as intrinsic Q-factor (Q_{in}). It is always desirable to design a cavity with large intrinsic Q-factors. This helps to minimize radiation losses in addition to allowing efficient light matter interaction in small volumes [8]. When additional decay channels, for example waveguides, are introduced around the cavity, the Q-factor reduces significantly due to larger decay rate. In such cases, we refer to the total Q-factor (Q_t) of the system given by

$$Q_t = \frac{\omega_0}{2(\gamma_{in} + \gamma_v)}\,, \tag{3.5}$$

where γ_v is the cavity field decay rate into the additional decay channel, e.g. waveguide.

The intrinsic Q-factor of our cavity is optimized using finite difference time domain (FDTD) simulations involving parameter scans for airholes shifts $C1$, $C2$, and $C3$, as shown in Fig. 3.1(a). Reasonably large Q_{in} is obtained when $C1 = 0.16\,a$, $C2 = 0.15\,a$ and $C3 = 0.074\,a$, where the lattice constant $a = 447$ nm. Figure 3.1(c) shows the resonance spectra of the *H0* nanocavity for three photonic crystal airhole radii values. Intrinsic Q-factors around 105,000, 82,000, and 35,000 have been

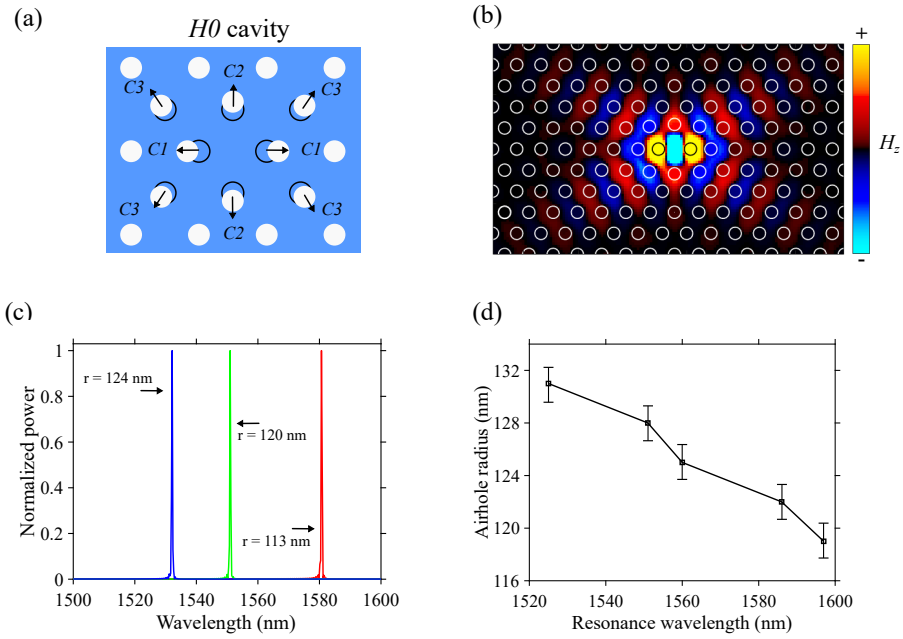

Figure 3.1: *H0*-type photonic crystal nanocavity and its resonance. (a) The cavity structure illustrating the shifting of the airholes away from the cavity center, where $C1 = 0.16a$, $C2 = 0.15a$ and $C3 = 0.074a$. The black circles indicate the location of the airholes if they were to keep the crystal lattice. The arrows indicate the direction of the corresponding shift. (b) FDTD calculated H_z field distribution at the resonance frequency of the *H0* cavity showing monopole cavity mode. (c) FDTD calculated cavity spectrum indicating the resonance peaks at 1532 nm, 1550 nm and 1580 nm for airhole radius of 124 nm, 120 nm and 113 nm respectively. (d) Measured *H0* nanocavity resonance peak spectral position as a function of the photonic crystal airhole radius.

obtained for airhole radius of 124 nm, 120 nm and 113 nm at resonance wavelengths of 1532 nm, 1550 nm and 1580 nm, respectively. The tunability of the resonance frequency with increasing or decreasing airhole radius, while still maintaining large quality factors, provides good tolerance to fabrication imperfections. A cavity having larger airholes has lower resonance wavelength. This is because an increase in airhole radius leads to cavity volume reduction this results in lower wavelength fundamental mode. The decrease in the intrinsic Q-factors for the airhole radius of 120 nm and 113 nm is due to non-optimized cavity structure. The cavities in this case can be optimized by adjusting the shifts of the airholes around the cavity

for large intrinsic Q-factors. The measured resonance wavelength versus airhole radius is shown in Fig. 3.1(d). It can be inferred that the resonance wavelength decreases with increasing airhole radius. The error bars indicate an uncertainty of about 3 nm in the measured airhole radius.

3.1.2 Line-defect waveguides

By introducing a linear defect into the periodic structure, we can create a waveguide mode that propagates along the defect. Such a linear defect could be a single row of missing airholes or multiple missing rows. In our hexagonally arranged airholes in the photonic crystal slab, we introduced a single row of missing airholes in the Γ-K direction which forms a $W1$-type single mode waveguide. The coefficient, n in Wn stands for the missing number of rows [17]. By increasing the number of missing rows, multimode photonic crystal waveguides can be designed [17, 40]. Figure 3.2(a) shows a schematic of a line-defect photonic crystal waveguide. Due

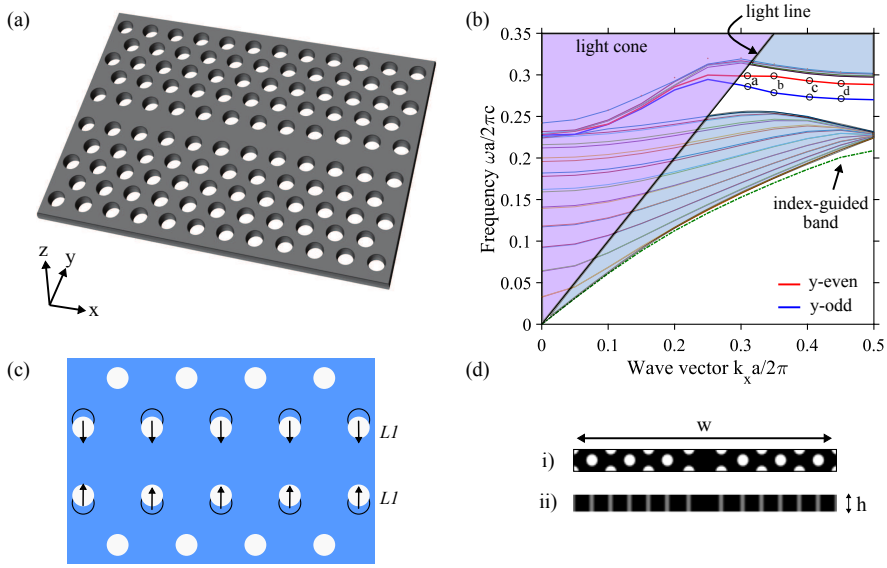

Figure 3.2: (a) Schematic of a line-defect photonic crystal waveguide (PhCW). (b) Band structure of the PhCW showing two gap bands, index guided band, the light cone and extended states. (c) Schematic diagram illustrating the shifting of the inner most rows of airholes to the waveguide center by an amount $L1 = 0.1208\,a$. (d) The super cell (i) top view, and (ii) side view, used for the calculation of the band structure of the PhCW using plane wave expansion methods in [41, 42]. The dimensions are h $= 0.76\,a$ and w $= 7\sqrt{3}\,a$.

to this line-defect, translational symmetry exists only in the x-direction parallel to the defect. The band structure of the photonic crystal slab has to be projected onto the new Brillouin zone in the k_x-path and is shown in Fig. 3.2(b). Note that the inner most rows of airholes are shifted towards the waveguide center by an amount $L1 = 0.1208\,a$ as illustrated in Fig. 3.2(c). The super cell used for calculating the band structure using plane wave expansion method of the MIT's free software package (MPB) [43] is shown in Fig. 3.2(d).

The light blue shaded region of Fig. 3.2(b) corresponds to the continuum of projected bands of the photonic crystal slab, and the light purple shaded region corresponds to the light cone ($\omega \geq c\mathrm{k}_x$). It can be seen that there is a TE-like band gap in the frequency range from $(0.26 - 0.3) \times 2\pi c/a$, where two defect states are located. These states are confined in the in-plane direction by the photonic crystal band gap and by index guiding in the out-of-plane direction. The light line $\omega = c\mathrm{k}_x$ (black line in Fig. 3.2(b)) separates the modes that are oscillatory in the slab from those that are evanescent in the slab. Above the light line these defect modes are still guided in the plane along the line-defect but they are lossy in the vertical direction [40]. Additionally. the band structure shows that there exists an all-index-guided mode (dashed-green line) due to a larger effective refractive index of the photonic crystal slab compared to its surrounding. Figure 3.2(c) shows the schematic of our $W1$ photonic crystal waveguide structure airholes arrangement. In addition to removing a single row of airholes, we have moved the inner most rows of airholes towards the waveguide center in order to obtain a high transmission bandwidth between 1530 nm and 1580 nm [44]. A similar effect can also be obtained by reducing the radius of the airholes adjacent to the waveguide [45].

The effect of shifting the inner most row of airholes on the waveguide performance can further be understood by looking at the modal field distribution. Since all the guided modes are TE-like and have no nodes in the z direction, we can visualize them by plotting the H_z-field in the $z = 0$ plane. Figure 3.3 shows the H_z-field patterns for the two defect-guided modes at labelled k_x positions (a, b, c and d) in the projected band structure of Fig. 3.2(b). The mode at the top is the fundamental mode while the bottom mode is the higher order mode. Because the system is invariant under reflections in the $y = 0$ plane, we can further classify these modes as either y-odd or y-even, where the fundamental mode is y-odd and the higher order mode is the y-even mode. Here, we focus our attention on the y-odd modes, because they can most easily be excited by a photonic wire waveguide modes [17]. The group refractive indices for the y-odd mode are calculated to be 4.4, 7.1, 15.8 and 28 at k_x points a, b, c and d indicated in Fig. 3.3(b) respectively. The y-odd mode at k_x points of a and b is well confined in the waveguide core without penetrating into the PhC cladding. Therefore, it is dependent on the parameters of the first row of airholes. In slow-light regimes (points c and d), the parameters of the second row of airholes are additionally important as the mode extends further into the PhC [45].

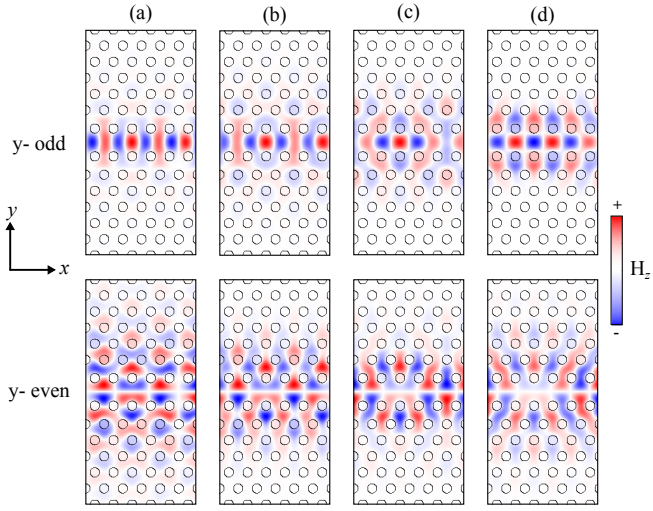

Figure 3.3: H_z field cross section for the designed line-defect waveguide, with (a-d) corresponding to the labelled circles of Fig. 3.2. The modes at the top corresponds to the y-odd modes while y-even modes are shown at the bottom. The calculations are based on PWE methods in [41, 42].

A scanning electron microscope (SEM) image of the fabricated photonic crystal waveguide is shown in Fig. 3.4(a). The measured transmission spectrum of the waveguide normalized to its peak is shown in Fig. 3.4(b) for TE-polarized input light. It shows only $\sim$ 2.5 dB transmission variation between 1540 nm and 1560 nm making it suitable for applications in the telecommunication C-band.

3.1.3 Grating couplers on indium phosphide (InP)

Here, light coupling mechanism into and out of the photonic crystal waveguides is discussed. In general, coupling light from a single mode optical fiber into nanophotonic waveguides and vice versa is a challenge mainly due to large refractive index and physical size differences which lead to mode profile mismatch and hence low coupling efficiency [46].

Several research groups have proposed various ways of coupling light between optical fibres and nanophotonic waveguides. The most common scheme is butt-coupling of cleaved waveguide facet with fibre. For improved coupling efficiencies, butt-coupling can be used with focusing objective lens or lensed fibre or integrated spot-size converters. Inverse tapers can also be used in combination with lensed fibre [47]. On the other hand, vertical coupling scheme can be implemented using grating couplers [46]. All of these possibilities have their own advantages and disad-

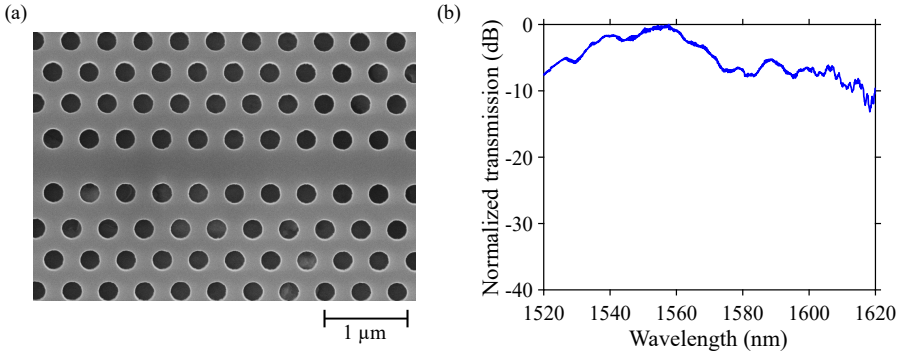

Figure 3.4: InP photonic crystal $W1$ waveguide. (a) Scanning electron microscope (SEM) image of the fabricated PhCW. (b) Measured transmission spectrum of the waveguide normalized to its peak.

vantages such as bandwidth limitation, alignment tolerance, fabrication complexity and yield. Therefore, one has to take these issues into account before choosing one.

In the early stages of this work and previous work [48], inverse tapered couplers with lensed fibres have been used for coupling light into the photonic crystal waveguides. Figure 3.5(a) shows the SEM image of the fabricated inverse taper. The E_y field distribution indicating the mode field expansion around the tip of

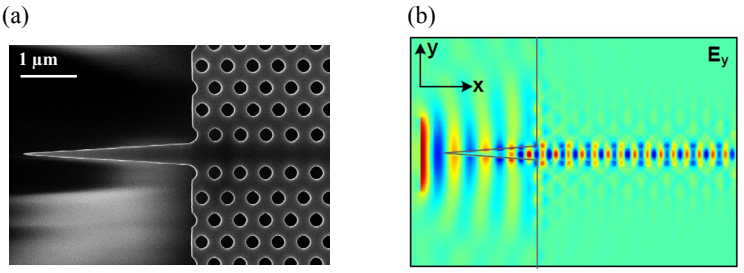

Figure 3.5: Inverse tapered couplers. (a) SEM image of the fabricated inverse tapered coupler. (b) Electric field (E_y) distribution around the inverse taper and the PhC interface (simulation taken from [48]).

the taper is shown in Fig. 3.5(b). With this scheme fibre-to-fibre insertion losses

around 20 dB have been measured. However, the final step in the device preparation which involves sample cleaving significantly reduces the device fabrication yield. Sometimes this results in cleaved waveguide facets instead of the inverse tapers making the insertion losses higher. The requirement of having inverse tapers at both ends of the PhCW also limits the minimum waveguide length to around 750 μm so that the sample can be handled with tweezers. Finally, with the aim for hybrid integration of InP to Si substrates, sample cleaving is less practical due to the difference in the crystal axis directions of the two material systems. Due to these issues, implementation of grating couplers is desired. Generally, the use of grating couplers helps to avoid sample cleaving making wafer scale tasting and low-cost packaging possible with relatively high coupling efficiencies [49, 46].

Taillaert, D. et al. [46] experimentally demonstrated grating coupling efficiency $> 30\%$ with 1 dB bandwidth of 40 nm on silicon-on-insulator (SOI). Uniform fully-etched photonic crystal airhole grating couplers in the SOI platform were demonstrated by Liu, L. et al. [50] with coupling efficiency of 42% and 1 dB bandwidth of 37 nm. Ding, Y. et al. [49] have experimentally demonstrated apodized grating couplers using fully etched photonic crystals on SOI with coupling efficiency of 67% and a 3 dB bandwidth of 60 nm. Most of these efficient grating couplers reported are implemented on silicon-on-insulator (SOI) substrates which is suitable for making waveguides completely surrounded by low-index materials such as air and silica. Grating coupler implementations on InP device layers is particularly challenging since they are usually grown on either InP or indium gallium arsenide (InGaAs) substrates which have similar refractive indices. This reduces the mode confinement in the waveguide leading to increased power leakage into the substrate resulting in high insertion loss waveguides and low efficiency grating couplers. Nevertheless, several efforts have been attempted at the realization of grating couplers on InP. For example, Van Laere, F. et al. [51] demonstrated a polarization diversity grating with 47% coupling efficiency on a benzocyclobutene (BCB) bonded InP membrane. This approach involves a complicated sample alignment technique as the grating couplers are patterned before the sample is bonded to the substrate. Using a suspended InGaAsP grating coupler Chen, L. et al. [52] demonstrated coupling efficiency of 40% with 3 dB bandwidth of 45 nm. These gratings, on the other hand, have mechanical disadvantage as the suspended membrane can easily be damaged by a coupling fibre during sample characterization.

To address these issues, we have implemented BCB wafer bonding of InP to Si wafer with silica on top as the initial process step. This insures that the InP device layer is completely surrounded by low-index materials i.e. air on top and silica underneath. Details of the device fabrication is presented in section 3.2. Next, we set the main design requirement to be a single dry-etch fabrication step to define the photonic crystal structure and the grating couplers. Since the InP device layer consisting of a photonic crystal has to be full-etched, airholes based grating couplers become a better choice than the shallow etched grating bars in [46].

A grating coupler should be able to couple guided modes to radiation modes using periodic perturbation of the refractive index [46]. The propagation constant of the guided mode is given by $\beta_{\text{guid}} = n_{\text{eff}} k_0$, where $k_0 = 2\pi/\lambda$ is the wave vector of light in air and n_{eff} is the effective refractive index of the guided mode in the waveguide before the grating coupler. The propagation constant of the radiation mode can be written as $\beta_{\text{rad}} = n_{\text{clad}} k_0 \sin\theta$, where n_{clad} is the refractive index of the top cladding material and θ is the coupling angle of the fibre as shown in Fig. 3.6. In this case, the top cladding material is air. The grating layer consists of a finite

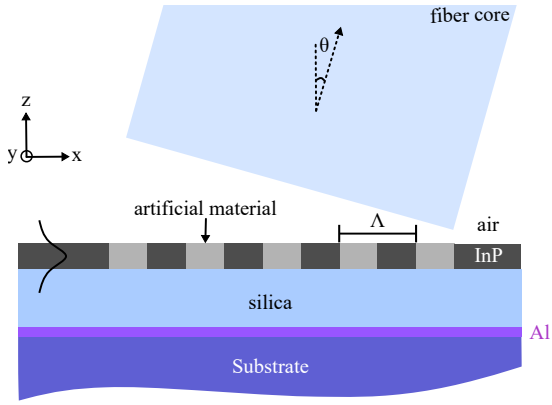

Figure 3.6: Schematic diagram of the grating coupled to a fibre at an incidence angle of θ. The grating layer (340 nm thick) is made of alternating InP and 'artificial' material. Below the grating layer is a 1.52 μm thick silica on top of Aluminium bottom reflecting mirror with thickness of 130 nm.

number of periodically alternating InP and 'artificial' material with grating period of Λ as shown in Fig. 3.6. The spatial wave vector of the grating can be defined as $K = 2\pi/\Lambda$. The two modes with propagation constants, β_{guid} and β_{rad}, are most effectively coupled by the spatial frequency component K that corresponds to

$$\beta_{\text{guid}} - \beta_{\text{rad}} + qK \approx 0\,, \tag{3.6}$$

where q is an integer number indicating the diffraction order. First-order grating ($q = \pm 1$) at a coupling angle of $\theta = 12^\circ$ is chosen to avoid back reflection into the waveguide [46]. The $q = -1$ order radiates parallel to the coupling fibre where as $q = 1$ order radiates into the substrate. In order to increase the coupling efficiency, a bottom reflecting aluminium mirror is implemented as shown in Fig. 3.6. Therefore, Eq. (3.6) can be rewritten for the case of $q = -1$ as

$$\Lambda = \frac{\lambda}{n_{\text{eff}} - n_{\text{clad}} \sin\theta}\,, \tag{3.7}$$

where λ is the central wavelength. For the typical case of operation at $\lambda = 1.55\,\mu$m with effective refractive index $n_{\text{eff}} = 2.42$ and coupling angle $\theta = 12°$, we obtain a grating period of 690 nm.

The SEM image in Fig. 3.7(a) shows the top view of the grating structure formed by periodically removing columns of airholes from hexagonally arranged photonic crystal. The missing airholes are indicated by the yellow circles. Here, we used the term 'artificial' material to denote the columns consisting of airholes since the effective refractive index is lower than InP but higher than air due to the inclusion of airholes. The red box shows the unit cell used for the calculation of grating parameters. The schematic diagram below the SEM image of Fig. 3.7(a) shows the grating layer consisting of periodic regions of InP and 'artificial' material with lattice period $\Lambda = 3a$, where $a = 230$ nm is the photonic crystal lattice constant. Assuming an infinitely long structure in the y-direction, the effective refractive index of the 2D artificial region (n_{art}) can be estimated as [49]

$$\frac{n_{\text{art}}^2}{n_{\text{air}}^2} = \frac{n_{\text{InP}}^2(1+f) + n_{\text{air}}^2(1-f)}{n_{\text{InP}}^2(1-f) + n_{\text{air}}^2(1+f)}\,, \tag{3.8}$$

where f is the volume filling fraction of the cylindrical inclusions given by [49]

$$f = \frac{3\sqrt{3}\pi D^2}{16b^2}\,, \tag{3.9}$$

where D is diameter of the airholes and b is the width of the artificial region which is equal to half of the grating period since the grating duty cycle is 50 %.

The electric field distribution, E_y, around the grating coupler at 1550 nm is calculated using the eigenmode expansion method with perfectly matched layers (PML) boundary conditions by the free software package called CAvity Modelling FRamework (CAMFR) [53] is shown in Fig. 3.7(b). It shows that the radiated field is vertically coupled out. In these 2D simulations, the bottom reflecting Al mirror is omitted because of convergence problems. Figure 3.7(c) shows the coupling efficiencies of the waveguide mode to upward radiated power (green line), to a single mode fibre (blue line) at coupling angle of $\theta = 12\,°$. The maximum coupling efficiency is -3.6 dB. It also shows that the back-reflected power (red line) is below 1 % around 1550 nm. These results are obtained for an optimized airhole radius $r = 89$ nm.

The optimized silica glass thickness for maximum coupling efficiency at 1550 nm is found to be around 1520 nm, as shown by the peak coupling efficiency of Fig. 3.7(d). The cross-sectional image of the wire waveguide leading to the grating coupler region indicating the different layers is shown in Fig. 3.7(e). The top layer is a 160 nm thick silicon nitride film used as hardmasking material for dry etching of InP. Below the silicon nitride mask is a 340 nm thick InP device layer sitting on top of a 1.5 μm thick silica glass layer, as shown by the zoomed-in SEM image (left) of Fig. 3.7(e). Underneath the glass layer is a 130 nm thick aluminium

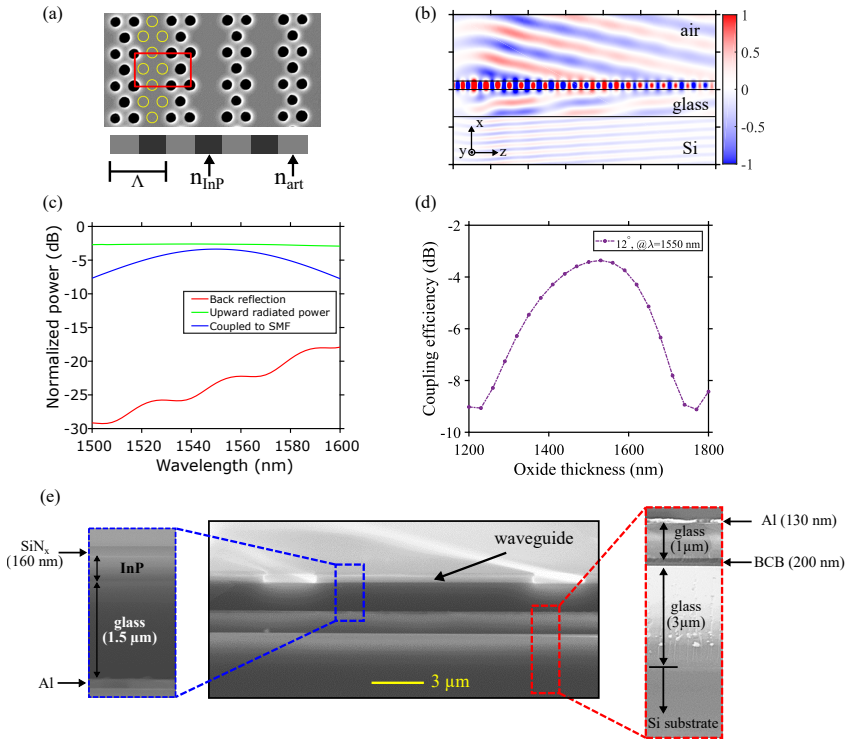

Figure 3.7: InP grating coupler structure, design and device layers. (a) SEM image of the fabricated photonic crystal grating. The yellow circles indicate the missing airholes. The red box indicates the unit cell considered for effective refractive index calculations. (b) E_y field distribution around the grating coupler. Each of the tick marks are separated by 2 μm. (c) Simulated upward radiated (green) power. The peak value of the upward radiated power coupling efficiency is -2.6 dB. The coupling efficiency (blue) indicates fraction of the radiated power coupled to a single mode fibre (SMF) at 12 °. The red line indicates back-reflected light from the grating coupler into the input waveguide. (d) The calculation of the silica glass thickness underneath the InP layer required for maximum coupling efficiency. With glass thickness around 1520 nm, it is possible to reduce the coupling losses down to -3.6 dB without using bottom reflector mirror. (e) SEM images showing the different layer compositions around the 340 nm thick InP wire waveguide.

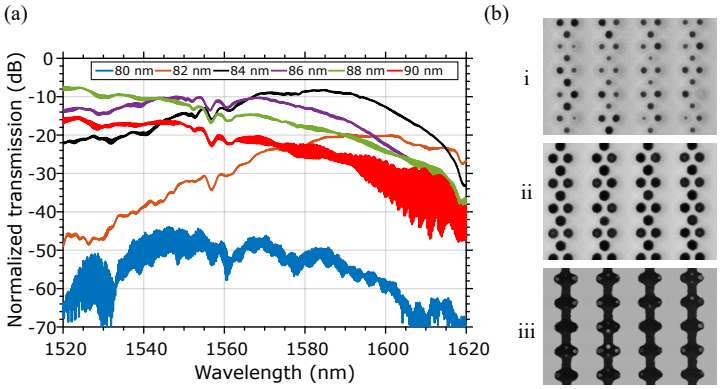

Figure 3.8: PhC grating coupler airhole variation vs coupling efficiency. (a) Transmission measurements using on-chip waveguides with grating coupler airholes radius varying from 80 nm to 90 nm. (b) SEM image of the grating couplers with airhole radius of 80 nm region (i), 88 nm region (ii), and 100 nm region (iii). The fabrication of these samples involves 31 dry etching cycles. All measurements were carried out using reference waveguides which are 3 μm wide and 1.9 mm long with input and output coupling angles of 15 °.

bottom reflecting mirror. The zoomed-in SEM image (right) of Fig. 3.7(e) shows the cross-section of a 200 nm thick BCB bonding interface between two layers of silica glass, one on the silicon substrate side while the other on the InP side.

Transmission measurements using input and output grating couplers and a 3 μm wide waveguide in between for varying airhole radius is shown in Fig. 3.8(a). The highest coupling efficiency around 1550 nm is obtained for airhole radius around 88 nm. The SEM images in Fig. 3.8(b) shows that narrower airholes, $r = 80$ nm in region (i), are difficult to etch through whereas wider airholes, $r = 100$ nm in region (iii), result in connected airholes. Therefore, it is desirable to use optimal airhole radius that can be uniformly and fully etched in order to obtain good coupling efficiency. In this case, we have found that airhole radius around 88 nm, Fig. 3.8(b) region (ii), is optimal.

Input coupling angle dependence of the grating couplers is shown in Fig. 3.9 (a) using transmission measurements while keeping the output coupling angle at 17 °. The highest transmission around 1550 nm is obtained at input coupling angle of 15 °. Similarly, output coupling angle dependence of the grating couplers is shown in Fig. 3.9(b) by setting the input coupling angle at the optimized value of 15 °. In this case, the peak transmission is measured to be −7.4 dB around 1530 nm for output coupling angle of 19 °. At 1550 nm, the maximum transmission (-8

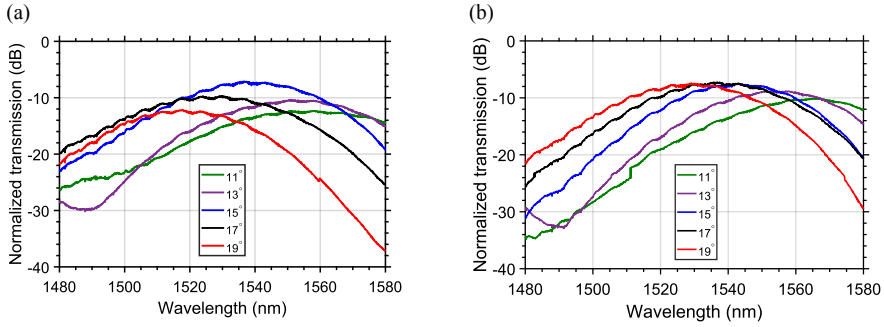

Figure 3.9: Coupling angle dependence of the PhC grating couplers. (a) Input coupling angle variation while the output coupling angle is kept at 17 °. (b) Output coupling angle variation while the input coupling angle is kept at 15 °. All the measurements were performed using a reference waveguide 12 μm wide and 1.9 mm long. The normalized transmission values indicate the input coupling loss, the output coupling loss, and transmission loss of the waveguide.

dB) is found for output coupling angle of 15 °. The transmission peak wavelength dependence on the coupling angle can be explained using Eq. (3.7). Increased coupling angles result in larger value of $\sin\theta$, hence the central wavelength shifts to the lower wavelengths.

The photonic crystal based grating coupler that we have described so far is known as a uniform grating coupler. This is because of the uniform design of the radius of the constituting airholes, as shown in Fig. 3.10(a). One of the limitation of such a uniform grating coupler is field profile mismatch between the radiated field, cf. Fig. 3.7(b), and the Gaussian mode profile of a single mode fibre. Better coupling efficiency can be achieved by tailoring the radius of the airholes so that the radiated field have Gaussian profile [49, 46]. Such a grating design is called nonuniform grating or apodized grating coupler. We have attempted to fabricate these apodized photonic crystal grating couplers, shown in Fig. 3.10(b). However, the nonuniform design of the airholes radius was not achieved with the desired accuracy. It can be seen in Fig. 3.10(b) that some columns of airholes are missing while larger airholes appears to be connected to each other. Therefore, further optimization on the electron beam lithography and subsequent dry-etching steps is required in order to realize this type of grating couplers.

Since our main aim of implementing grating couplers is to couple light efficiently into our photonic crystal waveguide with core widths of around 420 nm, the waveguide section connecting the grating coupler and this photonic crystal waveguide has to be tapered down from the 12 μm wide grating coupler to 420 nm. Figure 3.11(a) shows a schematic of three types of test waveguide structures investigated. The

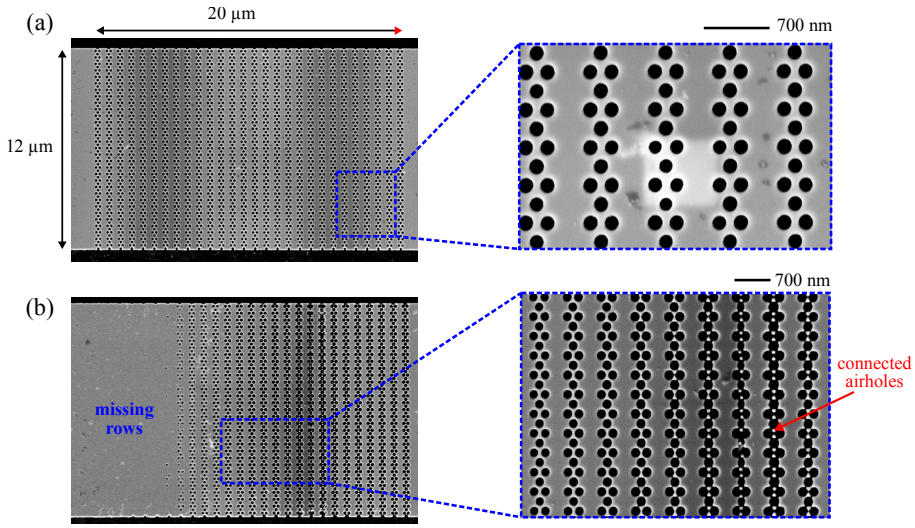

Figure 3.10: Uniform and apodized PhC grating couplers on InP. (a) SEM image of the fabricated uniform grating coupler. The inset shows a zoomed-in view of the grating structure. (b) SEM image of the fabricated apodized grating coupler having 8 missing rows. The inset shows a zoomed-in view of the grating illustrating the airholes connected to each other.

first waveguide, as shown in region (i), is 12 μm in width and connects the input and output grating couplers directly without tapering. The second waveguide, as shown in region (ii), includes a tapered section with the narrowest waveguide width corresponding to 3 μm. The third waveguide, as shown in region (iii), includes a tapered section with the narrowest waveguide width of 420 nm. The transmission measurements using these waveguides are shown in Fig. 3.11(c). It can be seen that the 12 μm and the 3 μm wide waveguides have similar transmission whereas the 420 nm narrow waveguide has large propagation loss. This may be due to significant overlap of the waveguide mode to the rough side walls shown in Fig. 3.11(b).

The final device structures and fibre coupling scheme is shown in Fig. 3.12. Part (a) and (b) show optical microscope images of the wire waveguide and the photonic crystal membrane embedded in the middle of the wire waveguide, respectively. The fabricated devices are typically 1.9 mm long. This length is chosen so as to allow enough space to couple two fibres during measurement. The InP wire waveguides are used for reference measurements including calibration of the grating coupler efficiencies and optimization of the coupling angles. Part (c) shows a photograph of

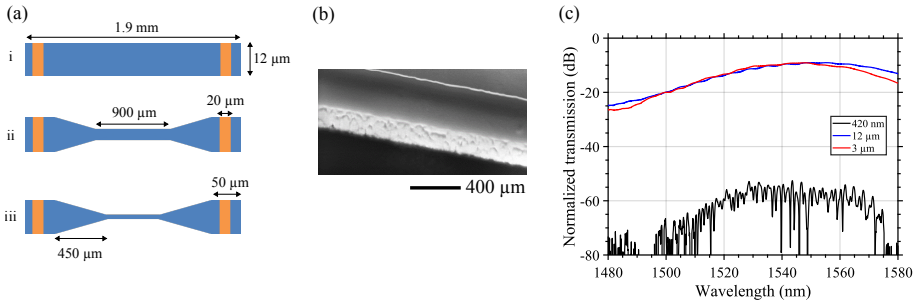

Figure 3.11: Different types of InP strip waveguides and their transmission spectra. (a) Schematics of 1.9 mm long waveguides with 12 μm region (i), 3 μm region (ii), and 420 nm region (iii) wide. The orange areas indicate the grating couplers. (b) SEM image showing the side view of the 420 nm wide waveguide. It can be seen that the side walls have significant roughness. (c) Transmission measurements for the three waveguides shown in part (a). Waveguides with 12 μm and 3 μm widths have almost equal insertion loss while the waveguide with 420 nm width has large insertion loss. All waveguides have input and output PhC grating couplers. Additionally, all the structures have a thin layer of silicon nitride (160 nm) on top of the InP device layer.

the typical fibre-to-chip coupling setup. Part (d) shows transmission measurements using the devices in part (a) and (b). The total insertion losses are -7 dB and -12 dB for the InP wire waveguide and PhCW, respectively. The extra 5 dB insertion loss in the PhCW case is mainly due to wire waveguide-PhCW interfaces at both ends of the photonic crystal membrane. The lowest insertion loss measured during this work is around 11 dB. Further optimization on the design of these interfaces is required for low-loss transmission. In the next section, we discuss the device fabrication steps.

3.2 Device fabrication

The device fabrication starts by preparing 2-inch silicon and InP wafers. The silicon wafer is typically single-side polished with 3 μm thick thermally grown silicon dioxide layer on top. The InP wafer consists of 340 nm InP device layer grown on top of a 1 μm thick indum galium asenide (InGaAs) wet-etch stop layer. Underneath the wet-etch stop layer is the InP substrate. This InP wafer is grown using metal organic vapour phase epitaxy (MOVPE) system available in-house. The next step is the deposition of 1.5 μm thick silica glass layer on top of the InP wafer using plasma enhanced chemical vapour deposition (PECVD). This layer will act as

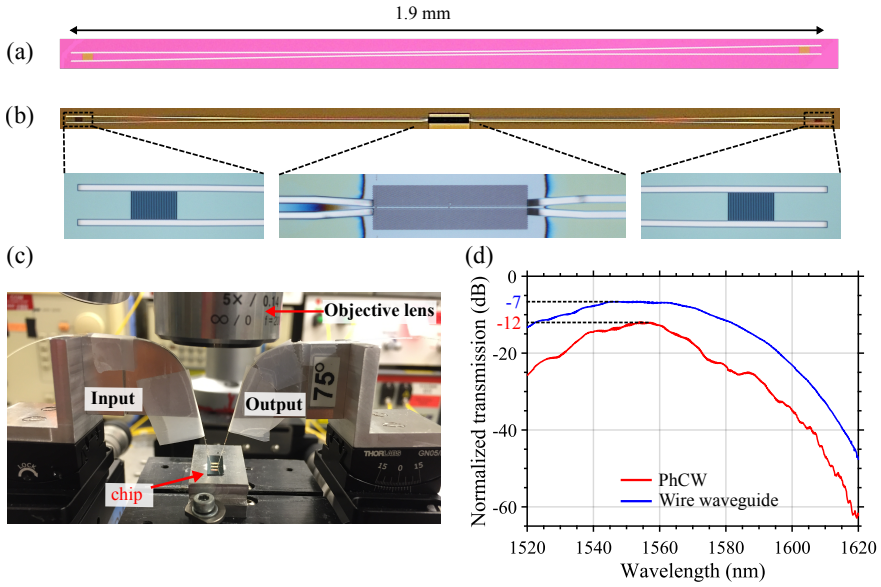

Figure 3.12: Optical microscope images, photograph of the fibre-to-chip coupling scheme and transmission measurements. (a) Reference InP waveguide consisting of input and output grating couplers. (b) The device consisting of PhC membrane section embedded in the middle and grating couplers. The insets show zoomed-in view of these sections. The photonic crystal is 50 μm long and 20 μm wide. (c) Photograph of the coupling scheme showing the input and output coupling fibres coupled at 12 ° to the grating couplers on the chip. (d) Transmission measurements using the devices in part (a) and (b). The transmission is normalized to the input power. The peak transmission of the wire waveguide is -7 dB while for the device consisting of the PhCW is -12 dB at around 1550 nm.

the bottom cladding material in the final device. On top of this glass, we deposit a 100 nm thick aluminium (Al) bottom reflecting mirror using standard electron-beam evaporation technique. This Al layer is then encapsulated using 1 μm thick silica glass deposited using PECVD. This step finalizes the InP wafer preparation.

The next process is BCB wafer bonding of these two wafers, both having silica glass layer on top. Adhesion promoter (AP3000, Dow chemicals) is spin coated, at 2000 rpm for 60 seconds, on both wafers and then baked at 160 °C for 1 minute. The silicon wafer is then spin coated with BCB (3022-46, Dow chemicals) at 5500 rpm for 60 seconds, and prebaked at 90 °C for 5 minutes. The InP wafer is then carefully placed upside down on top of the silicon wafer, cf. Fig. 3.13(a), inside the wafer bonding chamber (EVG Nanoimprint Lithography system). During the wafer bonding process, the sample is heated up to 250 °C and a force of 750 N is applied before cooling it down to room temperature. Now that we have a bonded sample, the following step is to remove the InP substrate by placing it in hydrofluoric (HF) acid (37%) solution for approximately one hour. The InGaAs wet-etch stop layer is then removed by a solution of sulphuric acid (10%) and hydrogen peroxide in 1:1 ratio. This step delivers the 340 nm thick InP (refractive index, $n \approx 3.17$) device layer sitting on low refractive index silica glass layer ($n \approx 1.45$), cf. Fig. 3.13(b). The wafer is then cleaved into small chips of dimension 1.5 cm $\times$ 1.5 cm for further processing.

A 200 nm thick silicon nitride (SiN_x) hard mask is then deposited on the chip using PECVD technique. On top of the SiN_x, a positive e-beam resist ZEP-520A is spin coated at 2600 rpm for 1 minute followed by baking at 160 °C for 5 minutes, resulting in a thickness of around 500 nm. Following this, all the device structures including the photonic crystal, the grating couplers, and the wire waveguides are patterned using electron-beam (e-beam) lithography (JEOL JBX-9500FS), cf. Fig. 3.13(c). After e-beam exposure, the resist is developed using ZED N50 (ZEON corporation) for 2 min. After resist development, the pattern is transferred onto the silicon nitride hard mask by a mixture of trifluoromethane and oxygen (CHF_3/O_2) gases in a reactive-ion etching (RIE, PLASSYS) process. Then, the resist is removed using remover (1165, Dow chemicals). The pattern is further transferred to the InP layer by RIE cyclic dry-etching process using CH_4/H_2 mixture, cf. Fig. 3.13(d). Here, it is worth noting that a single InP dry-etch step is used to fabricate all the device components greatly reducing the fabrication complexity.

The final step in the fabrication is the selective membranization of the photonic crystal structure. A positive photoresist, AZ5214E, MicroChemicals, is spin coated at 4000 rpm and baked for 90 seconds at 90 °C resulting in thickness of $\sim 1.4\,\mu$m. A membranization window around the photonic crystal membrane, cf. Fig. 3.12(b), is then formed using standard photolithography process involving Süss MicroTec MA6 aligner and resist development using tetramethylammonium hydroxide (TMAH) for 60 seconds. The photonic crystal is then membranized using SiO etch solution for 6 minutes. This step etches away both the SiN_x hardmask

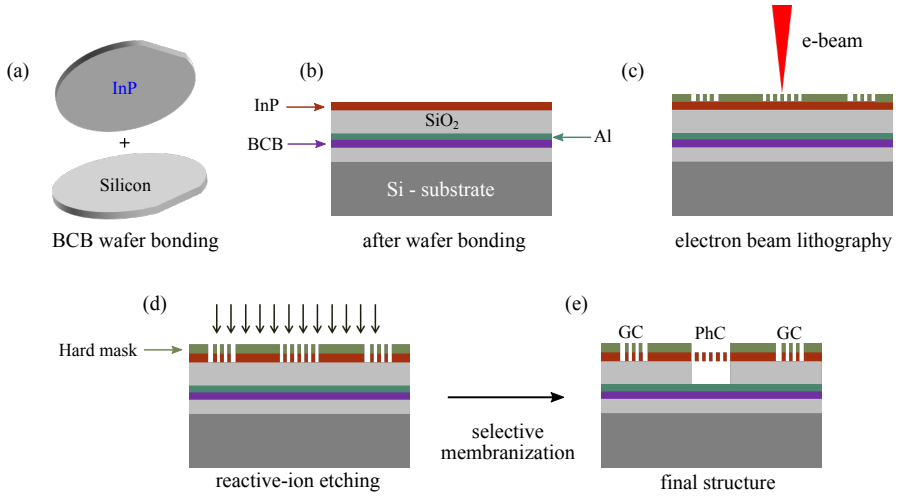

Figure 3.13: Summary of the fabrication processes. (a) BCB bonding of InP and silicon wafers. (b) layer compositions of the bonded wafer after substrate removal process. It consists of InP device layer, silica glass layer and aluminium bottom reflecting mirror. (c) electron beam lithography process for patterning all device components. (d) pattern transfer to the InP device layer through reactive-ion etching process by using silicon nitride as a hard mask. (e) the final device structure after selective membranization process resulting in a suspended InP PhC membrane, and grating coupler (GC) sections.

and the silica glass underneath the photonic crystal structure by flowing through the airholes leaving a photonic crystal membrane suspended in air. Because of the selective membranization, the wire-waveguides and the grating couplers are still supported by the silicon oxide layer underneath, cf. Fig. 3.13(e). After the photoresist is stripped away, the sample is then ready for measurement. A brief summary of the fabrication processes is shown in Fig. 3.13.

Scanning electron microscope (SEM) images showing parts of the fabricated device are presented in Fig. 3.14. Part (a) shows the top view of the PhC membrane with input and output wire waveguides connected to it. Part (b) shows a cross-sectional image of the photonic crystal cleaved in the direction x-x shown in part (a). Note that the membrane was damaged during cleaving process. However, it can clearly be seen that silica glass underneath the photonic crystal is completely etched away. The inset shows a close-up view of the airhole profiles. It is observed that the airholes have rough side walls and are slightly 'V-shaped' instead of having straight side walls. Various optimizations on the e-beam lithography, resist development, and subsequent dry-etching processes are required to obtain high quality PhC.

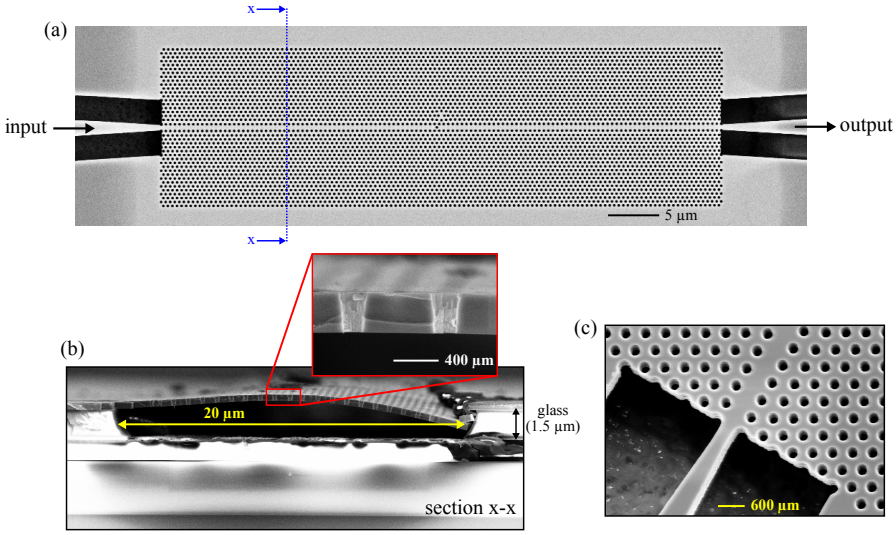

Figure 3.14: SEM images of the InP photonic crystal membrane device. (a) Top view of the PhC membrane. (b) Cleaved cross-section of the PhC membrane showing successful membranization. Note that the membrane is damaged due to the cleaving process. The inset shows zoomed-in view of the airholes profile across the membrane. (c) Angled view of the wire waveguide to PhC waveguide interface.

Chapter 4

Fano resonances in photonic crystal structures

In this chapter, we discuss the basic geometries of devices consisting of a waveguide side-coupled to a single mode cavity. The general property of the structures is presented using coupled mode theory. For the realization of these structures we have chosen the photonic crystal platform, discussed in chapter 3, which provides inherent design flexibility, optimal control over the input and output signals, and facilitates further large scale integration [54]. One of the great advantages of using photonic crystal cavities is the enhancement of nonlinear optical processes, which significantly reduces the frequency shift required for on/off switching in microcavity structures [55].

Two of the structures that are considered in this thesis are shown in Fig. 4.1 and consist of a cavity side-coupled to a waveguide. For the structure in Fig. 4.1(a) coupling to the output port is only possible through the cavity. On the other hand, for the structure in Fig. 4.1(b) there is also a direct path to the output port through the waveguide. The transmission through the waveguide is determined by the transmission coefficient (t_B) of the partially transmitting element (PTE). Based on the resonance lineshape observed in the transmission spectrum of the coupled system, we refer to the structures in Fig. 4.1(a) and Fig. 4.1(b) as Lorentzian and Fano structures, respectively.

4.1 Coupled-mode theory

We will now, based on Ref. [17, 55, 56, 57], derive a set of equations describing the coupling of the cavity to the waveguide, in terms of the field amplitudes in the waveguide and cavity. Consider the cavity-waveguide coupled system shown in Fig 4.1(b). The cavity supports a single mode with resonance frequency ω_0. The waveguide is assumed to support a continuum of modes around the resonance

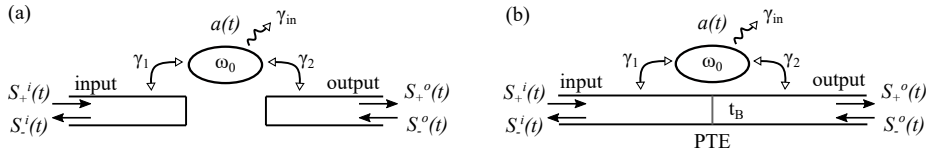

Figure 4.1: Waveguide-cavity coupled systems consisting of forward and backward propagating fields of the waveguide and the field amplitude in the cavity. The cavity mode decay rates into the input and output port are γ_1 and γ_2, respectively. The out-of-plane decay rate is γ_{in}. (a) A schematic of the Lorentzian structure. (b) A schematic of the Fano structure consisting of a partially transmitting element (PTE) with transmission coefficient of t_B placed in the middle of the waveguide.

frequency of the cavity. Note that the structure in Fig. 4.1(a) can be modelled as as special case of Fig. 4.1(b) in which $t_B = 0$. The cavity field can be written as

$$A(t) = a(t)\exp(-i\omega_0 t)\,, \tag{4.1}$$

where $a(t)$ is the cavity field amplitude and $|A(t)|^2$ is the electromagnetic energy stored in the cavity. When the structure is excited with light of angular frequency ω_s, the signal field in the waveguide can be written as

$$S_y^x(t) = s_y^x(t)\exp(-i\omega_s t)\,, \tag{4.2}$$

where the power of the signal in the waveguide is $|S_y^x(t)|^2$, with $x = i$ or $x = o$ representing the signal field at the input or output ports, respectively. The forward and the backward propagating fields are denoted by $y = +$ and $y = -$, respectively.

Let us now calculate the complex coupling coefficients between the waveguide and the cavity using conservation of energy. Suppose that there is no input energy to the system, i.e. $S_+^i(t) = S_-^o(t) = 0$, and consider the simplified case where the intrinsic losses of the cavity are neglected, i.e. $\gamma_{in} = 0$. Furthermore, assume that the output waveguide from Fig. 4.1(a) is removed so that the only field decay possible from the cavity is to the input port. The cavity mode, Eq. (4.1), decays exponentially as $A(t) = a(t)\exp[-i\omega_0 t - \gamma_1 t]$, where γ_1 is the decay rate of the field into the input port. Thus, the cavity energy $|A(t)|^2$ is decreasing and it is going into the input waveguide. This can be written as [17]

$$-\frac{d|A(t)|^2}{dt} = 2\gamma_1|A(t)|^2 = |S_-^i(t)|^2\,, \tag{4.3}$$

$$S_-^i(t) = \sqrt{2\gamma_1}A(t). \tag{4.4}$$

Substituting Eqs. (4.1) and (4.2) into the above equation, we have

$$s_{-}^{i}(t) = \sqrt{2\gamma_1}a(t). \tag{4.5}$$

Since the phase of $s_{-}^{i}(t)$ is arbitrary, as it represents the field amplitude anywhere along the waveguide depending on the choice of reference plane and instance of time [17], we can define the coupling coefficient in terms of the decay rates as $d_1 = \sqrt{2\gamma_1}e^{i\theta_1}$. Similarly, the coupling coefficient to the output port can be written as $d_2 = \sqrt{2\gamma_2}e^{i\theta_2}$. Here, θ_1 and θ_2 denote the phase factors of the coupling coefficients.

The rate of change of the cavity field for the structure in Fig. 4.1(b) in the presence of an intrinsic decay rate can be written as [57]

$$\dot{A}(t) = (-\gamma_v - \gamma_{in} - i\omega_0)A(t) + \begin{bmatrix} d_1 & d_2 \end{bmatrix} \begin{bmatrix} S_{+}^{i}(t) \\ S_{-}^{o}(t) \end{bmatrix}. \tag{4.6}$$

The structure is excited with light of angular frequency ω_s, this implies that the field everywhere oscillates as $\exp(-i\omega_s t)$ [17]. Substituting this into Eq. (4.1), and using Eq. (4.2), we can rewrite Eq. (4.6) as

$$\dot{a}(t) = \big(- \gamma_v - \gamma_{in} - i(\omega_0 - \omega_s)\big)a(t) + \begin{bmatrix} d_1 & d_2 \end{bmatrix} \begin{bmatrix} s_{+}^{i}(t) \\ s_{-}^{o}(t) \end{bmatrix}, \tag{4.7}$$

where, ω_0 is the resonance frequency of the cavity, γ_{in} is the intrinsic loss of the cavity given by $\gamma_{in} = \omega_0/(2Q_{in})$, and γ_v is the cavity field decay rate into the input and output ports i.e. $\gamma_v = \gamma_1 + \gamma_2$.

The input energy from $s_{+}^{i}(t)$ can couple into the cavity, be transmitted to the output port or be reflected back to the input port. Using the scattering matrix formalism, the field amplitudes in the waveguide can be written as [56, 57]

$$\begin{bmatrix} s_{-}^{i}(t) \\ s_{+}^{o}(t) \end{bmatrix} = \begin{bmatrix} r_B & -it_B \\ -it_B & r_B \end{bmatrix} \begin{bmatrix} s_{+}^{i}(t) \\ s_{-}^{o}(t) \end{bmatrix} + \begin{bmatrix} d_1 \\ d_2 \end{bmatrix} a(t)\,, \tag{4.8}$$

where r_B and t_B are the amplitude reflection and transmission coefficients of the PTE, respectively. For a lossless system, r_B and t_B are real and positive with $r_B^2 + t_B^2 = 1$.

Using the coupled-mode equations (4.7) and (4.8), we can now calculate the transmission spectrum of the cavity-waveguide systems in Fig. 4.1 when the input power from the right is zero, i.e. $s_{-}^{o}(t) = 0$ and the frequency of the input signal from left is ω_s. In steady-state, $\dot{a}(t) \approx 0$, Eqs. (4.7) and (4.8) will be reduced to

$$0 = [-\gamma_v - \gamma_{in} - i(\omega_0 - \omega_s)]a(t) + d_1 s_{+}^{i}(t)\,, \tag{4.9}$$

$$s_{-}^{i}(t) = r_B s_{+}^{i}(t) + d_1 a(t)\,, \tag{4.10}$$

$$s_{+}^{o}(t) = -it_B s_{+}^{i}(t) + d_2 a(t). \tag{4.11}$$

The amplitude transmission of the system can be found by dividing Eq. 4.11 with $s_+^i(t)$ and substituting $a(t)$ from Eq. (4.9) as

$$t(\omega_s) = \frac{s_+^o(t)}{s_+^i(t)} = -it_B + \frac{2\sqrt{\gamma_1\gamma_2}e^{i(\theta_1+\theta_2)}}{\gamma_1+\gamma_2+\gamma_{in}+i(\omega_0-\omega_s)}. \tag{4.12}$$

For Fano structures ($0 < t_B < 1$), the phase term $e^{i(\theta_1+\theta_2)}$ can be calculated from the values of t_B, γ_1 and γ_2 using the requirements of energy conservation and time-reversal symmetry [48, 58] as

$$e^{i(\theta_1+\theta_2)} = it_B\sqrt{\frac{\gamma_2}{\gamma_1}}\left[\frac{1}{r_B e^{-i2\theta_1}+1}\right], \tag{4.13}$$

$$\cos(2\theta_1) = \frac{(\gamma_2-\gamma_1)t_B^2 - 2\gamma_1 r_B^2}{2\gamma_1 r_B}. \tag{4.14}$$

For Lorentzian structures ($t_B = 0$), the electromagnetic flux leaking into the input and output ports are the same, i.e. $\gamma_1 = \gamma_2 = \gamma_v/2$. Additionally, the phase factors θ_1 and θ_2 fulfill the relations $\theta_1 + \theta_2 = (2n+1)\pi$ and $\theta_1 + \theta_2 = 2n\pi$ for even and odd cavity modes respectively [57]. Therefore, the transmission of the system can be written as

$$t(\omega_s) = \pm\frac{\gamma_v}{\gamma_v+\gamma_{in}+i(\omega_0-\omega_s)}, \tag{4.15}$$

where the negative (positive) sign corresponds to a cavity mode, E_y-field profile, that is even (odd) with respect to the mid-plane passing through the cavity center. The power transmission, $T(\omega_s) = |t(\omega_s)|^2$ spectra for the Lorentzian and Fano structures in Fig. 4.1(a) and (b) are plotted in Fig. 4.2.

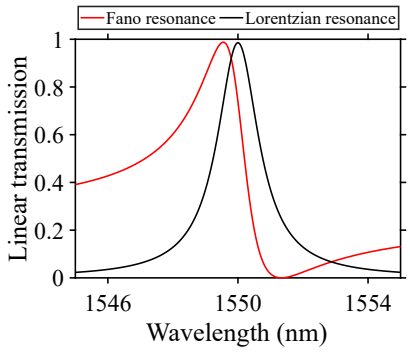

Figure 4.2: Lorentzian and Fano resonance lineshapes. The parameters used are $Q_t = 1000, Q_{in} = 1.2\times10^5, t_B = 0.5, \gamma_1 = \gamma_2, \lambda_0 = 1550$ nm.

As can be inferred from Fig. 4.2, the transmission spectrum of the Lorentzian structure exhibits symmetric lineshape with peak transmission around the resonance frequency of the cavity and zero transmission elsewhere. On the other hand, the transmission spectrum for the Fano structure shows an asymmetric lineshape characterized by having a maximum and a minimum transmission which are located in close spectral range. The cavity only supports a few discrete cavity modes while the waveguide supports a continuum of guided modes [17, 55]. The interference between these two optical paths creates an asymmetric Fano resonance lineshape as shown in Fig. 4.2 [54, 55, 59]. Recently, such resonances have found several applications in nanophotonics, such as in switching [60], lasing [61, 62, 63, 64], nonreciprocal transmission [65], and sensing [66].

4.2 Photonic crystal Fano structures

Our platform for the realization of Fano resonances is an InP photonic crystal membrane structure, composed of hexagonally arranged airholes as discussed in chapter 3. The fabricated photonic crystal Fano structure, cf. Fig. 4.3(a), consists of an *H0* nanocavity [15] side-coupled to a line-defect waveguide. All airholes have a radius of 125 nm except the PTE airhole which has a radius of 123 nm.

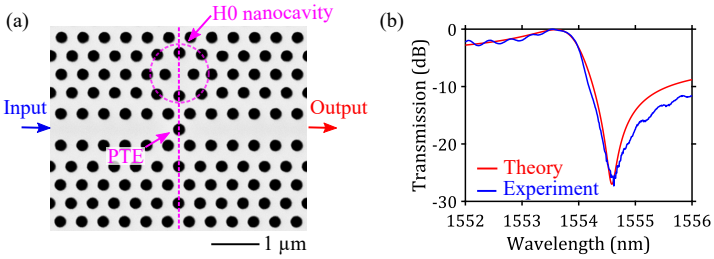

Figure 4.3: (a) Scanning electron microscope (SEM) image of the fabricated InP photonic crystal Fano structure. It consists of a *H0* nanocavity, a line-defect PhC waveguide and a partially transmitting element (PTE) airhole placed in the middle of the waveguide at the mid-plane passing through the center of the nanocavity. (b) Measured and fitted transmission spectra of the device showing an asymmetric Fano resonance lineshape.

The PTE airhole controls the amplitude of the continuum contribution in addition to controlling the phase of the coupling according to Eqs. (4.13) and (4.14). This gives rise to a characteristic asymmetric Fano lineshape as shown in Fig. 4.3(b). The blue line shows the experimentally measured transmission, while the red line shows a CMT fit to the measurement. The total Q-factor of the cavity

and the amplitude transmission coefficient of the PTE extracted from the CMT fit are $Q_t \sim 1700$ and $t_B = 0.55$. For these theoretical fits the intrinsic quality factor of the cavity is fixed at 1.2×10^5 estimated using finite difference time domain (FDTD) simulations.

In order to estimate the transmission coefficient of the PTE, we have investigated a waveguide structure without a side-coupled cavity. Figure 4.4(a) shows the fabricated PhC waveguide with PTE for characterization of the transmission properties. The transmission coefficient of the PTE airhole can be estimated experimentally from the measurement in Fig. 4.4(b) by comparing the waveguide transmission without PTE with that of the transmission with PTE. It can be seen that the transmission drops by 2 dB around 1550 nm for the case where the PTE is blocking the waveguide. In this case, the radius of the PTE airhole was the same as all other airholes ($r = 125$ nm). This corresponds to an amplitude transmission coefficient value of ~ 0.79. The noise ripples that appear in the spectrum of the

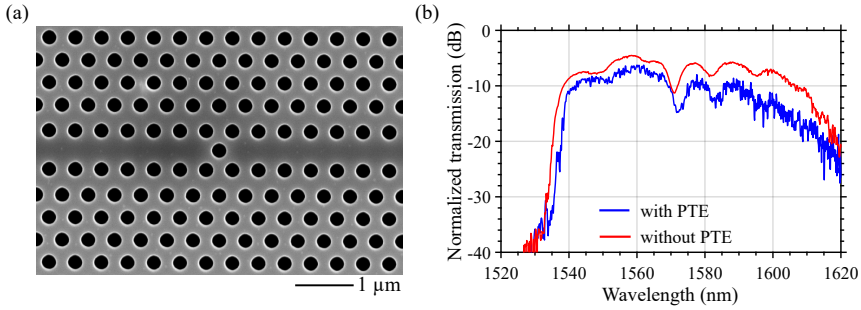

Figure 4.4: Photonic crystal waveguide with partially transmitting element (PTE) airhole (a) SEM image of the fabricated photonic crystal waveguide with a PTE placed in the middle. (b) waveguide transmission spectra with and without PTE.

waveguide consisting of the PTE is due to the Fabry-Perot cavity formed between the PTE, and the interface between the PhCW and the strip waveguide, cf. Fig. 3.14(a).

The normalized E_y-field distributions for the Fano resonance structure obtained from 3D FDTD simulations are shown in Fig. 4.5. The photonic crystal device structure is overlapped with the field distribution for better illustration. The field distribution determined at the transmission peak is shown in Fig. 4.5(a). On the other hand, the E_y field profile at the transmission minimum, cf. Fig. 4.5(b), indicates very low transmission to the output port since most of the power is reflected back to the input port due to destructive interference.

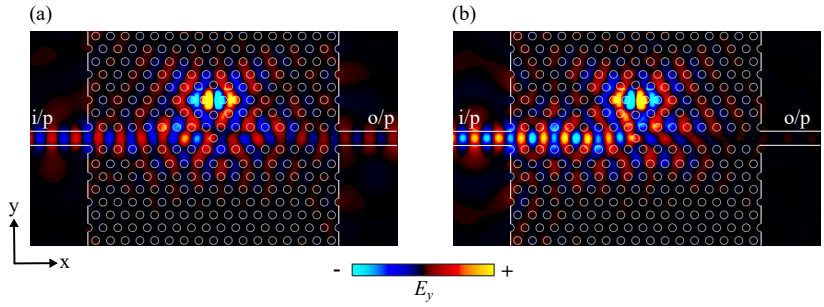

Figure 4.5: Normalized E_y-field distribution for Fano resonance structure. (a) At transmission peak. (b) At transmission minimum.

4.2.1 Fano resonance extrema separation

One of the key features of the asymmetric Fano resonance is the existence of maximum and minimum transmission points with small spectral separation, cf. Fig. 4.2, which makes it suitable for ultrafast optical switching [54, 55, 59, 67, 60]. In this subsection we derive an analytical expression governing the spectral separation between the peak and minimum transmission for the mirror symmetric case in which the PTE is placed at the symmetry plane.

In the mirror symmetric case, the decay rates from the cavity to the input and output ports are equal, i.e. $\gamma_1 = \gamma_2 = \gamma_v/2$. Equation (4.14) will reduce to $\cos(2\theta_1) = -r_B$. Substituting this result into Eq. (4.13), we have $e^{i(\theta_1+\theta_2)} = -r_B + it_B$. Substituting this phase term into Eq. (4.12), we get

$$t(\omega_s) = -it_B - \frac{\gamma_v(r_B - it_B)}{\gamma_v + \gamma_{in} + i(\omega_0 - \omega_s)}. \tag{4.16}$$

For simplicity of calculation, the out-of-plane decay rate from the cavity is neglected ($\gamma_{in} = 0$), which is a good approximation when the nanocavity is strongly coupled to the waveguide. In order to find the local minima and maxima, we take the partial derivative of Eq. (4.16) with respect to ω_s. This gives the values of the maximum and minimum, which are

$$\omega_s = \left\{\omega_0 - \tfrac{t_B}{r_B}\gamma_v, \quad \omega_0 + \tfrac{r_B}{t_B}\gamma_v\right\}. \tag{4.17}$$

The spectral separation between these Fano extrema points is calculated to be

$$\Delta\omega = \frac{\gamma_v}{t_B r_B}. \tag{4.18}$$

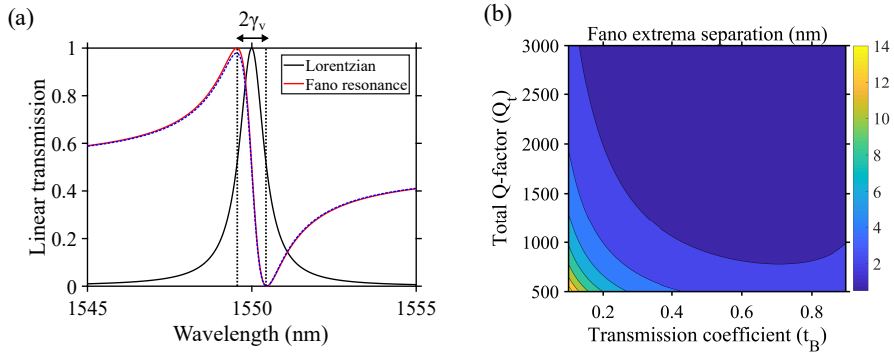

Figure 4.6: Separation between the extrema of Fano resonance for symmetric placement of the PTE. (a) For a given Q-factor, the minimum spectral separation between the minimum and the maximum transmission of the Fano resonance (red line) is equal to the linewidth of the Lorentzian resonance (black line), $2\gamma_v$, when $t_B = 1/\sqrt{2}$. Here, a Q_t value of 1700 is used in the simulations. The dashed blue line shows the Fano resonance for the case of finite out-of-plane decay rate. Note that the inclusion of a vertical decay rate results in a slightly lower peak transmission without affecting the extrema separation. (b) Contour plot of Fano extrema separation in nanometers as a function of total Q-factor and amplitude transmission coefficient. Extrema separations smaller than 2 nm are achieved for Q_t values greater than 1000, and $0.45 < t_B < 0.8$.

It is often desirable to calculate the minimum extrema separation that can be achieved for a given Q-factor of the cavity. This can be calculated by taking the first derivative of Eq. (4.18) with respect to t_B and solving for t_B. We obtain that the transmission coefficient t_B has to be equal to $1/\sqrt{2}$, for achieving the minimum separation, irrespective of the decay rate. Substituting this result into Eq. (4.18), we get

$$(\Delta\omega)_{min} = 2\gamma_v. \tag{4.19}$$

Therefore, the smallest spectral separation between the transmission maximum and minimum of an asymmetric Fano resonance is equal to the linewidth of the Lorentzian resonance corresponding to the decay rate $2\gamma_v$, as illustrated in Fig. 4.6(a). The dashed blue line in Fig. 4.6(a) shows the case in which a finite vertical decay rate is assumed. It can be observed that the inclusion of a vertical decay rate results in a slightly lower peak transmission without affecting the extrema separation. This peak transmission value is $T = (1 - Q_t/Q_{in})^2 \approx 0.97$, assuming $\gamma_1 = \gamma_2$ [68].

The contour plot in Fig. 4.6(b) shows the Fano resonance extrema separation in nanometers as function of the total Q-factor, $Q_t = \omega_0/2\gamma_t$. As before, we have set $\gamma_{in} = 0$, so that $\gamma_t = \gamma_v$. It can be seen that for Q_t greater than 1000, amplitude transmission coefficients in the range between 0.45 and 0.8 give extrema separations less than 2 nm. This is particularly advantageous in providing large fabrication tolerance for the PTE airhole dimension which is the key element in realization of asymmetric Fano resonance.

4.2.2 Parity control of Fano resonances

The parity of a Fano resonance expresses whether the transmission minimum is red-shifted (red-parity) or blue-shifted (blue-parity) compared to the transmission maximum [69], as shown in Fig. 4.8. In literature [54, 70], the blue (red) parity Fano resonances are denoted using positive (negative) values of the asymmetry parameter of the Fano lineshape, where the asymmetry parameter describes the ratio between the resonant and non-resonant transmission amplitudes in the scattering process. The accurate control of the parity of Fano resonances is essential for optical signal processing applications requiring specific switching order, i.e. either on-off or off-on, when a resonance shift is triggered.

Let us consider the system in Fig. 4.7(a) which consists of a waveguide-cavity coupled structure with the PTE placed far away from the cavity. Here, we assume

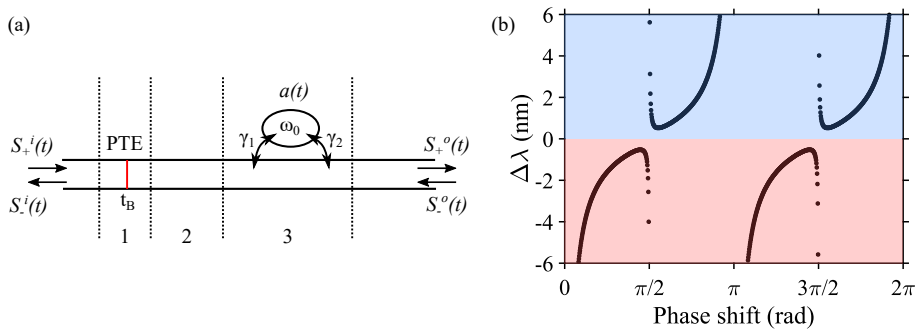

Figure 4.7: (a) A schematic of the model used for a transfer-matrix (T-matrix) analysis of the system. The structure is divided into three sections consisting of the PTE section, coupled-cavity waveguide section, and a waveguide section between the PTE and the cavity. (b) Wavelength difference between the transmission maximum and minimum of the Fano resonance as a function of the phase shift induced in the waveguide section. Red-parity and blue-parity corresponds to $\Delta\lambda < 0$, and $\Delta\lambda > 0$, respectively. The parameters used in this simulation are $Q_{in} \approx 1.2 \times 10^5$, $Q_t \approx 1000$, $t_B = 1/\sqrt{(2)}$, and $\gamma_1 = \gamma_2$.

that the evanescent fields from the cavity completely decay before reaching the PTE region. Therefore, we can separate the system into three sections defined by individual transfer (T) matrices based on the model in Ref. [55]. These sections are indicated by the regions 1, 2 and 3 in Fig. 4.7(a). The T-matrices are denoted by T_{PTE}, T_{wg} and T_c corresponding to the PTE section, the waveguide between the PTE and the cavity, and the coupled cavity-waveguide section, respectively. The T-matrices for these three sections can be written as [55]

$$\begin{bmatrix} s_+^o \\ s_-^o \end{bmatrix} = \begin{bmatrix} \frac{-\gamma_v}{\gamma_{in}+i(\omega_0-\omega)} - 1 & \frac{\gamma_v}{\gamma_{in}+i(\omega_0-\omega)} \\ \frac{-\gamma_v}{\gamma_{in}+i(\omega_0-\omega)} & \frac{\gamma_v}{\gamma_{in}+i(\omega_0-\omega)} - 1 \end{bmatrix} \begin{bmatrix} s_+^i \\ s_-^i \end{bmatrix}, \tag{4.20}$$

$$\begin{bmatrix} s_+^o \\ s_-^o \end{bmatrix} = \frac{1}{-it_B} \begin{bmatrix} 1 & -r_B \\ r_B & 1 \end{bmatrix} \begin{bmatrix} s_+^i \\ s_-^i \end{bmatrix}, \tag{4.21}$$

$$\begin{bmatrix} s_+^o \\ s_-^o \end{bmatrix} = \begin{bmatrix} e^{i\theta} & 0 \\ 0 & e^{-i\theta} \end{bmatrix} \begin{bmatrix} s_+^i \\ s_-^i \end{bmatrix}, \tag{4.22}$$

where $\gamma_1 = \gamma_2 = \gamma_v/2$, and θ is the phase change that the waveguide mode accumulates when propagating between the PTE and the cavity. Equations (4.20), (4.21) and (4.22) represent the T-matrices for the cavity-waveguide, PTE section, and the waveguide section between the PTE and the cavity, respectively. The total T-matrix of the system can then be obtained by $T = T_{PTE}T_{wg}T_c$ as

$$\begin{bmatrix} s_+^o \\ s_-^o \end{bmatrix} = \begin{bmatrix} T_{11} & T_{12} \\ T_{21} & T_{22} \end{bmatrix} \begin{bmatrix} s_+^i \\ s_-^i \end{bmatrix}. \tag{4.23}$$

Note that the order of the matrix is different from our previous definition in Eq. (4.8). This is due to the use of T-matrix instead of the scattering matrix formalism [71]. The amplitude transmission of the system can then be calculated using $t(\omega_s) = 1/T_{11}$, where

$$T_{11} = \frac{1}{-it_B}\left[\frac{\gamma_v(r_B e^{-i\theta} - e^{i\theta})}{\gamma_{in} + i(\omega_0 - \omega)} - e^{i\theta}\right]. \tag{4.24}$$

Depending on the value of the phase change (θ), the transmission of the system can be designed for a lineshape with either red or blue-parity. Figure 4.7(b) shows the wavelength difference in nanometers between the transmission maximum and minimum of the Fano resonance as a function of the phase shift. Positive wavelength difference corresponds to blue-parity while a negative value indicates the occurrence of red-parity Fano resonance. Note that the transmission spectrum becomes Lorentzian when the phase change is an integer multiple of $\pi/2$, corresponding to a transition from red-parity to blue-parity, and vice versa.

While the model presented above is suitable to explain the basic mechanism of parity change of asymmetric Fano resonances, it is not applicable for cases where the PTE is placed in close proximity to the cavity. In such cases, the system

cannot be separated into different sections. Therefore, a rigorous numerical model taking into account the actual device geometry has to be implemented as reported in Ref. [69] for photonic crystal based cavity-waveguide structures. An alternative approach would be to simulate the transmission of the system using a 3D FDTD model, which allows easy control of the position of the PTE airhole in a trial-and-error approach. A PTE airhole placed one lattice constant to the left from the mid-plane passing through the waveguide center results in blue-parity Fano resonance [69, 60]. On the other hand, we have shown in Fig. 4.3 that a PTE placed in the waveguide at the mid-plane passing through the cavity center results in red-parity Fano resonances. We use these results for the realization of our asymmetric Fano resonances [72]. Figure 4.8 shows a summary of the structures and the lineshapes for Lorentzian, red and blue-parity Fano resonances.

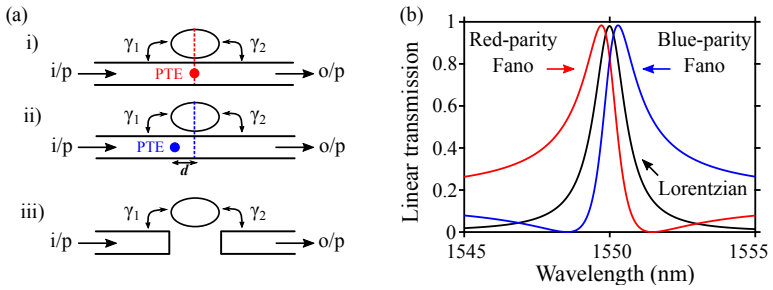

Figure 4.8: Comparison of Lorentzian and Fano resonance structures and their corresponding lineshapes. (a) A schematic of the structures for realizing red-parity Fano (i), blue-parity Fano (ii), and Lorentzian (iii) resonances. (b) Red and blue-parity Fano resonances compared with Lorentzian resonance lineshape. All resonances have the same intrinsic and total quality factors Q_{in}, and Q_t of 1200, and 1.2×10^5, respectively. Also, the resonance wavelength of the cavities are 1550 nm. Here, $Q_t = \omega_0/(2\gamma_t)$, where $\gamma_t = \gamma_1 + \gamma_2 + \gamma_{in}$, and $\gamma_1 = \gamma_2$. The amplitude transmission coefficient of the PTE is 0.4 for both the red and blue-parity Fano resonances.

4.3 Resonance shift of InP photonic crystal cavities

In this section, we discuss different physical mechanisms that can be used for changing the complex refractive index of the nanocavity, which in turn is the basis for using the Fano device as a switch. The discussion is based on the works reported in [36, 56, 73, 74]. This change in the complex refractive index leads to a resonance shift, as shown in Fig. 4.9, that trigger the switch-on or the switch-off action. Figure 4.9(a) shows illustration of the resonance blue-shift for the red-parity Fano

resonance, while Fig. 4.9(b) shows for the case of blue-parity Fano resonance. The dashed black lines, cf. Fig. 4.9, illustrate the resonance blue-shift due to nonlinear optical effects in the case of a decrease of the refractive index by $\Delta n/n \approx 10^{-3}$ [56, 60, 72].

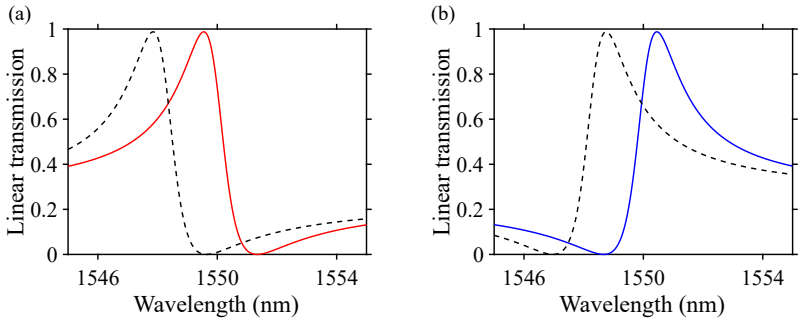

Figure 4.9: Fano resonance blue-shift. (a) Red-parity Fano resonance (red line) and illustration of resonance blue-shift (dashed black line) induced by a decrease of the refractive index by $\Delta n/n \approx 10^{-3}$. (b) Blue-parity Fano resonance (blue line) and illustration of resonance blue-shift (dashed black line).

The resonance shift can be included in the dynamic equation for the cavity field of Eq. (4.7), excited by a forward propagating signal $s_+^i(t)$ injected from the input port, as

$$\dot{a}(t) = (-\gamma_v - \gamma_{in} - i(\omega_0 + \Delta\omega(t) - \omega_s))a(t) + \sqrt{2\gamma_1}e^{i\theta_1}s_+^i(t)\,, \tag{4.25}$$

where $\Delta\omega(t)$ is the complex resonance shift. When the cavity is excited close to its resonance frequency, a highly localized intensity is built up in the nanocavity, leading to a change in the refractive index. Several nonlinear processes discussed in section 2.2 contribute to the change in the complex refractive index of InP around the nanocavity region. The corresponding complex resonance shift can be written as [36, 56]

$$\Delta\omega(t) = -\big(K_{kerr}|a(t)|^2 - K_{car}N_c(t) + K_{th}\Delta T\big) - i\big(K_{TPA}|a(t)|^2 + K_{FCA}N_c(t)\big)\,, \tag{4.26}$$

where $N_c(t)$ is the effective carrier density in the region defined by the cavity resonant mode profile. The coefficients K_{kerr}, K_{car}, K_{th}, K_{TPA}, and K_{FCA} represent contributions from Kerr effect, carrier-induced effects, thermo-optic effects, two-photon absorption (TPA) and free-carrier absorption (FCA), respectively. Using the relation, $\Delta\omega/\omega = \Delta n/n$, and Eq. (2.25), the complex resonance frequency

change due to these nonlinear processes is related to the refractive index change and decay rate as [36, 73]

$$\Delta\omega = -\frac{\omega_0}{n}\Delta n - i\frac{\gamma}{2}. \tag{4.27}$$

Kerr effects

One of the nonlinear processes occuring in the nanocavity is the Kerr effect, which scales with the intensity of the light in the cavity as given by Eq. (2.38). The energy stored in the cavity, $|a(t)|^2$, is related to the intensity of the light, I, in the cavity as [74]

$$I = \frac{c_0}{nV_{kerr}}|a(t)|^2\,, \tag{4.28}$$

where c_0 is the speed of light in vacuum, n is the refractive index of InP, V_{kerr} is the effective mode volume associated with Kerr effects. Using Eq. (2.38) the modal refractive index change for the PhC cavity due to the Kerr effect can be written as [73]

$$\Delta n_{kerr} = \frac{\Gamma_{kerr}c_0 n_2}{nV_{kerr}}|a(t)|^2\,, \tag{4.29}$$

where n_2 is the Kerr coefficient, Γ_{kerr} is the confinement factor associated with Kerr effects. As both the Kerr effect and TPA share the same dependence on field strength, the confinement factors and the effective mode volumes are equal, i.e. $\Gamma_{kerr} = \Gamma_{TPA}$ and $V_{kerr} = V_{TPA}$ [73]. Since nearly all the light is confined in the membrane area, we assume the confinement factors to be close to unity [56]. Using Eq. (4.27) and (4.29), and comparing to Eq. (4.26), we obtain

$$K_{kerr} = \frac{\omega_0 c_0 n_2}{n^2 V_{kerr}}. \tag{4.30}$$

Two-photon absorption (TPA)

A rather dominant effect in InP-based photonic crystal cavities is the two-photon absorption, cf. Table 2.1. The highly localized intensity in the nanocavity allows for generation of free-carriers by absorption of two photons according to Eq. (2.41). Here, we restrict our attention to the case of below-bandgap excitation, where linear absorption can be neglected. The effective modal TPA decay rate for PhC cavities is given by [73, 74]

$$\gamma_{TPA} = \frac{c_0}{n}\beta_{\mathrm{TPA}} I\,, \tag{4.31}$$

$$\gamma_{TPA} = \frac{\beta_{\mathrm{TPA}} c_0^2}{n^2 V_{TPA}}|a(t)|^2\,, \tag{4.32}$$

where β_{TPA} is the two-photon absorption coefficient. Comparing Eq. (4.32) to (4.26) and using Eq. (4.27), we obtain

$$K_{TPA} = \frac{\beta_{\mathrm{TPA}} c_0^2}{2n^2 V_{TPA}}. \tag{4.33}$$

Carrier-induced change in refractive index

While the TPA contributes to the change in the imaginary part of the refractive index, the generated free-carriers induce further changes in the refractive index. These are known as the carrier-induced refractive index changes which include plasma dispersion, band filling effects and bandgap shrinkage. [28, 36]. The refractive index change due to the plasma effect can be written using Eq. (2.49) as

$$\Delta n_{plas} = -\frac{e^2}{2m_e \epsilon_0 n \omega_s^2} N_c(t)\,, \tag{4.34}$$

where e is the elementary electric charge, m_e is the effective electron mass, and ω_s is the angular frequency of the input light. Here, the contribution of holes is neglected due to the much smaller effective mass of electrons in InP. Band filling effects cause a reduction in the refractive index, while band-gap shrinkage causes an increase in the refractive index, as discussed in section 2.2.3, [28]. Including the contributions from plasma dispersion, band filling effects and bandgap shrinkage, the coefficient K_{car} is estimated to be $1.95 \times 10^{-12}\mathrm{m}^2/\mathrm{s}$ [28, 56].

Free-carrier absorption (FCA)

A free electron can absorb a photon and move to a higher energy state within the conduction band. This intraband absorption is called free-carrier absorption. The optical decay rate due to free-carrier absorption is given by [73]

$$\gamma_{FCA} = \frac{c_0 \sigma}{n} N_c(t)\,, \tag{4.35}$$

where $N_c(t)$ is the effective carrier density in the cavity region generated by TPA given by Eq. (2.41) and σ is the absorption cross-section for $N_c(t)$. Comparing Eq. (4.35) to (4.26) and using Eq. (4.27), we obtain

$$K_{FCA} = \frac{c_0 \sigma}{2n}. \tag{4.36}$$

Thermo-optic effects

So far, we have discussed that the highly confined optical power in the PhC cavities results in two-photon and free-carrier absorption processes. It is important to notice that a significant fraction of this absorbed power is converted to kinetic

energy of electrons leading to heating [36, 56, 73]. The fraction of the absorbed power contributing to heating of the nanocavity, $P_{abs}(t)$, can be written as [56, 73]

$$P_{abs}(t) = (\gamma_{FCA} + \eta\gamma_{TPA})|a(t)|^2 \,. \tag{4.37}$$

Here, η is the fraction of the energy of the two-photon converted to kinetic energy of electrons, and is given by

$$\eta = \frac{2\hbar\omega_s - E_g}{2\hbar\omega_s} \,, \tag{4.38}$$

where $2\hbar\omega_s$ is the energy of the two-photon. For light of wavelength around 1550 nm in InP with bandgap energy $E_{\mathrm{g}} = 1.34\,\mathrm{eV}$, we have $\eta \approx 17\,\%$. The change in temperature $\Delta T(t)$ between the cavity and the neighbouring region induced by heating due to the input signal can be approximated according to Ref. [56] as

$$\Delta\dot{T}(t) = -\gamma_{th}\Delta T(t) + P_{abs}(t)/C_{\mathrm{InP}} \,, \tag{4.39}$$

where γ_{th} is the thermal relaxation rate, and C_{InP} is the thermal capacitance of the InP photonic crystal membrane. Due to high thermal resistance in photonic membranes, thermal effects are very important and need to be carefully evaluated for applications [36].

The heat source term of Eq. (2.59) at steady state can be found by $q_T = P_{abs}(t)/V_{th}$, where V_{th} is the effective thermal volume, which roughly corresponds to the cavity volume [36]. From the mode distribution, the maximum increase in temperature, ΔT, in the cavity can be calculated using the finite element method (FEM) by solving the two-dimensional heat diffusion equation, Eq. (2.59) [56]. This temperature distribution is then set as initial distribution in Eq. (2.59), with $q_T = 0$, to determine the relaxation time required to reach a steady state value [56, 48]. The temperature decay rate is then fitted with an exponential function with a single time constant (τ) [56], and the thermal capacitance is approximated as $C_{th} = \tau/R_{th}$, where R_{th} is the thermal resistance of the photonic crystal cavity calculated using $R_{th} = \Delta T/P_{abs}(t)$. For better modelling of these thermal effects of photonic crystal cavities, two exponential time scales shall be used as reported in Ref. [36]. Using Eqs. (4.27) and (2.58), the thermal coefficient of Eq. (4.26) can be written as

$$K_{th} = \omega_0 n_T/n \,, \tag{4.40}$$

where n_T is the temperature dependent refractive index of indium phosphide related to the background refractive index by Eq. (2.58).

4.3.1 Free-carrier dynamics

In this subsection, we discuss the dynamics of the free-carriers generated in the PhC cavity. Particularly, the physical mechanisms leading to carrier relaxation,

and the rate equations governing their dynamics are discussed based on the works reported in [56, 36, 12, 75].

The initial carrier distribution in the cavity, generated by TPA, shows spatial and temporal variation due to carrier diffusion and recombination processes. Carriers are assumed to spread and distribute homogeneously within the membrane. Here, the rate of diffusion of electrons and holes is assumed the same, i.e. ambipolar diffusion. On the other hand, the recombination or relaxation of carriers includes contributions from bulk and surface recombinations. Bulk recombination, due to radiative and Auger recombinations, is a slow process which has typical values spanning from tens to several hundreds of nanoseconds [56, 76]. A rather dominant carrier relaxation process in PhC, owing to their large surface area to volume ratio, is the surface recombination [12]. At the surface of a semiconductor the atomic lattice is abruptly interrupted. This results in dangling bonds, unpaired outer-shell electrons, which introduces surface states that can trap charge carriers enhancing electron-hole recombination [77]. For InP *H0* PhC cavities, the initial fast change of the carrier distribution is related due to carrier diffusion, while surface recombination takes over at the latter stages of the process [68, 75].

Therefore, the effective carrier lifetime, τ_{car}, is given by [56, 12]

$$\frac{1}{\tau_{\mathrm{car}}} = \frac{1}{\tau_{\mathrm{rec}}} + \frac{S}{L}\,, \tag{4.41}$$

where τ_{rec} is the bulk recombination rate, S is the surface recombination velocity, and L is the maximum distance to the top or bottom surface of the photonic crystal. For PhC membrane structures, $L = h/2$, where h is the PhC membrane thickness. Surface recombination velocity in InP, $S = 10^4$ cm/s, is much slower than in GaAs, $S = 10^7$ cm/s [12, 68].

Assuming a train of pulses exciting the cavity, the effective carrier density builds up depending on the simple rate equation [36, 12]

$$\dot{N}_{\mathrm{eff}}(t) = -N_{\mathrm{eff}}(t)/\tau_{\mathrm{car}} + G(t)\,, \tag{4.42}$$

where $G(t)$ is the carrier generation rate related to the duration of the excitation pulse. Here, it is worth mentioning that if the carrier lifetime is too short, carriers cannot accumulate in the cavity region and hence carrier-induced refractive index changes will be weak. On the other hand, if the carrier lifetime is long, the recovery time of the switch increases. An optimal choice for fast all-optical signal processing would be carrier lifetimes close to the duration of the excitation [12].

In order to describe experimentally observed non-exponential relaxation of carriers dynamics in InP photonic crystal nanocavities [56], the simple rate equation (4.42) can be expanded into three coupled rate equations with three characteristic time constants [56]

$$\dot{N}_c(t) = -\big(N_c(t) - N_2(t)\big)/\tau_1 - N_c(t)/\tau_3 + G(t)\,, \tag{4.43}$$

$$\dot{N}_2(t) = -\big(N_2(t) - N_3(t)\big)/\tau_2 + \big(N_c(t) - N_2(t)\big)/\tau_1 \times R_{12} - N_2(t)/\tau_3\,, \quad (4.44)$$

$$\dot{N}_3(t) = \big(N_2(t) - N_3(t)\big)/\tau_2 \times R_{23} - N_3(t)/\tau_3\,. \quad (4.45)$$

Here, $N_c(t)$ is the effective carrier density in the region defined by the cavity resonant mode profile, cf. Fig. 4.10(a). The carrier density $N_c(t)$ couples with a short time constant τ_1 to $N_2(t)$ defined as the carrier density in the immediate neighbouring region of the cavity, cf. Fig. 4.10(b). This mainly accounts for the initial decay of $N_c(t)$ due to fast diffusion [56]. Similarly, the carrier density $N_2(t)$ couples with time constant τ_2 to $N_3(t)$, which is an even larger neighbouring region around the cavity, cf. Fig. 4.10(c). The longest time constant τ_3 is associated with bulk and surface recombination which affect all the carrier populations. The R_{12} and R_{23} represent the ratios between the carrier volume of $N_c(t)$ and $N_2(t)$, and $N_2(t)$ and $N_3(t)$, respectively, and indicate the conservation of carriers when they are exchanged between the different volumes [56]. The carrier generation rate, $G(t)$, due to TPA can be obtained from Eq. (2.41) and Eq. (4.28) as [56]

$$G(t) = \frac{\beta_{\mathrm{TPA}} c_0^2 |a(t)|^4}{2\hbar\omega_s n^2 V_{FCA}^2}\,, \quad (4.46)$$

where V_{FCA} is the effective free-carrier absorption mode volume characterizing the mode averaged free-carrier density generated by TPA [56].

Figure 4.10 shows the time evolution of the carrier distribution around the *H0* cavity determined by the resonance cavity mode profile calculated using 2D finite element simulation [56]. Note that the carriers diffuse in all directions into the regions around the cavity.

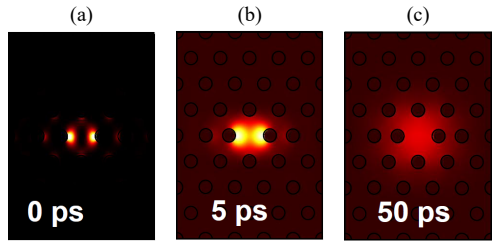

Figure 4.10: The time evolution of the carrier density distributions of the *H0* photonic crystal cavity at (a) 0 ps, (b) 5 ps, and (c) 50 ps. Higher carrier density is indicated by the bright yellow color. Figure taken from [56].

4.3.2 Summary

Even though the instantaneous Kerr effects and thermal effects cause changes in the local refractive index of the cavity, it is the decrease in the refractive index by the plasma effect which dominates in magnitude in InP for photon energies much below the bandgap. This results in a blue-shift of the photonic crystal cavity resonance. The recovery of this shifted resonance is then determined by the dynamics of the generated free-carriers, which is mainly governed by the diffusion and the recombination rates of the carriers.

Our model involves solving the differential equations of (4.25), (4.39), (4.43), (4.44) and (4.45) numerically using the MATLAB built in function *ode45*. The output power of the waveguide-cavity coupled system including the nonlinear effects can then be calculated using Eq. (4.11). The parameters used in these simulations are listed in Table 4.1. This model is used in the following chapters for simulations of pulse carving, signal reshaping and all-optical switching applications using Fano resonances.

Table 4.1: Parameters used in the coupled-mode theory (CMT) model for simulation of transmission properties of InP PhC Fano structures involving resonance shifts as a result of various nonlinear optical processes triggered by the injected optical signals.

Parameter	Symbol	Value	Ref.
Intrinsic Q-factor	Q_{in}	120000	FDTD
Total Q-factor	Q_t	1000	Meas. fit
Amplitude transmission coeff.	t_B	0.5	Meas. fit
Refractive index of InP	n	3.17	[37]
TPA volume	V_{TPA}	0.21 μm^3	[56]
FCA volume	V_{FCA}	0.13 μm^3	[56]
FCA cross section	σ	4.5×10^{-21} m^2	[78]
Thermo-optic coefficient	n_T	2.01×10^{-4} K^{-1}	[37]
TPA coefficient	β_{TPA}	24 cm/GW	[32]
Kerr coefficient	n_2	16.5×10^{-18} m^2/W	[56]
Carrier effects coefficient	K_{car}	1.95×10^{-12} m^2/s	[56, 28]
Thermal capacitance	C_{InP}	3.6×10^{-13} J/K	[56]
Thermal relaxation rate	γ_{th}	1.6×10^{8} s^{-1}	[56]
Carrier lifetime in region 1	τ_1	3 ps	[56]
Carrier lifetime in region 2	τ_2	85 ps	[56]
Carrier lifetime in region 3	τ_3	180 ps	[56]
Carrier vol. ratio b/n region 1 & 2	R_{12}	0.5	[56]
Carrier vol. ratio b/n region 2 & 3	R_{23}	0.4	[56]

Chapter 5

Pulse carving using Fano resonances

In this chapter, we present applications of the red-parity Fano resonance for processing pulses, i.e. RZ signals encountered in on-chip optical communication systems. As mentioned in Chapter 2, RZ signals have several advantages over NRZ signals due to improved receiver sensitivity, less inter-symbol interference and low average power [2, 38]. For on-chip and chip-to-chip interconnects, larger receiver sensitivity can enable the system to be operated at lower power budget, leading to reduced thermal effects, thus creating opportunities for higher density of integration [2]. Generating short pulses or low duty cycle RZ signals is interesting for applications requiring sharp raising and falling edges such as for synchronization and clocking [2]. Furthermore, a simple pulse-edge detection scheme is desirable for applications that require precise information about the time of arrival of a signal [2]. Conventional pulse carving employs active radio frequency (RF) clock signal for modulation, where the input signal (usually NRZ) is carved into RZ signal [38, 79].

The main content of this chapter is based on our work [72] which reports the use of an asymmetric Fano resonance in combination with strong nonlinear optical effects in a nanocavity that allows the carving of a short pulse from a long input pulse without the need for an additional control signal as shown schematically in Fig. 5.1.

5.1 Principle of pulse carving

Here, we present the theoretical model and simulation results for nonlinear pulse carving of input pulses whose shape and pulse widths corresponds to the experimentally investigated pulses. The input waveguide field amplitudes $s_+^i(t)$ of Eq. 4.2 takes on the waveform of a higher-order Gaussian pulse or super-Gaussian pulse train given in the general case as:

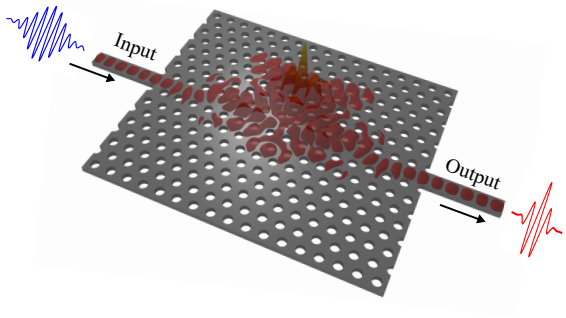

Figure 5.1: Device schematic illustrating short pulse output from long input pulse using InP photonic crystal membrane consisting of a nanocavity side-coupled to a line-defect waveguide. FDTD simulated out-of-plane magnetic field profile (H_z) is overlapped with the device structure.

$$s_{+}^{i}(t) = A_o \sum_{m=-\infty}^{+\infty} \exp\left[-\left(2\ln 2 \left(\frac{t - mT_r}{\tau_w} \right)^2 \right)^n \right], \tag{5.1}$$

where:

- A_o is the amplitude of the pulse
- τ_w is the FWHM of the intensity profile of the Gaussian pulse when $n = 1$
- n is the order of the super-Gaussian pulse ($n = 1, 2, 3, ...$)
- T_r is the temporal pulse spacing related to pulse repetition rate as $f_r = 1/T_r$
- m is an integer number in the range $(-\infty, \infty)$

The photon life time, $\tau_p = 1/\gamma_t$, in the photonic crystal cavity for typical Q_t values around 1000 is $\sim 1\,\text{ps}$. This is much shorter than the duration of the input pulse ($> 90\,\text{ps}$) that we are investigating here. Therefore, the change in the cavity field amplitude for the duration of the input pulse is assumed negligible and hence adiabatic elimination ($a(t) \approx 0$) can be used similar to Eq. 4.9. The amplitude transmission through the Fano structure, cf. Fig. 4.2(b), can be written by using Eq. 4.12 as:

$$t_{\text{Fano}}(\omega_s, t) = -it_B + \frac{2\sqrt{\gamma_1\gamma_2}e^{i(\theta_1+\theta_2)}}{\gamma_1 + \gamma_2 + \gamma_{in} + i(\omega_0 + \Delta\omega(t) - \omega_s)}, \tag{5.2}$$

where $\Delta\omega(t)$ is the complex resonance shift caused by the input pulse at time t given by Eq. 4.26, and ω_s is the angular frequency of the input pulse.

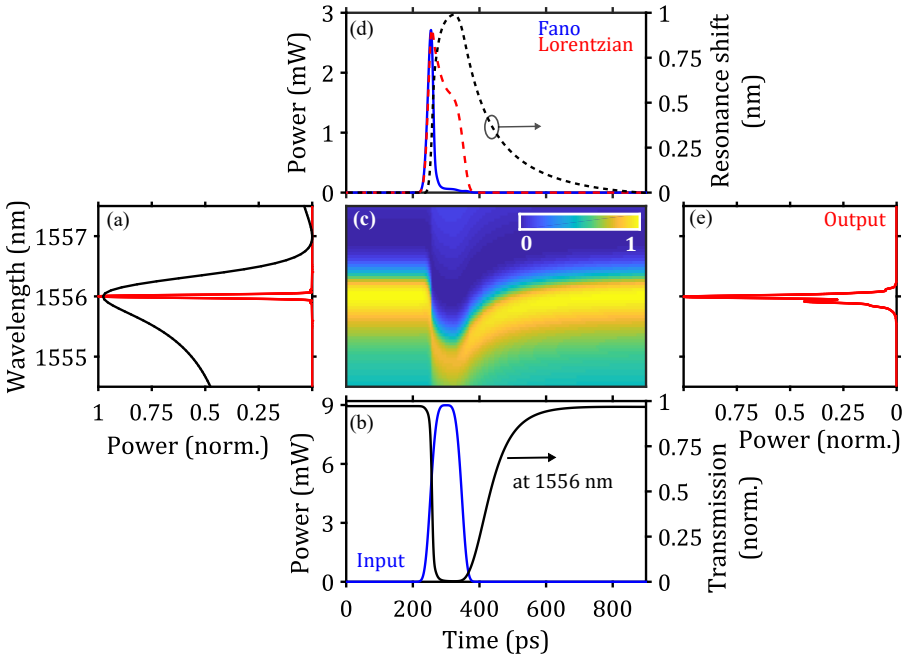

Figure 5.2: Basic principle of pulse self-carving using Fano resonance. (a) Fano lineshape (black, linear scale) with resonance peak at 1556 nm and input pulse spectrum (red). (b) Super Gaussian input pulse (blue) with a width of 93 ps and transmission (black) at 1556 nm as a function of time. (c) Contour plot of the time evolution of linear transmission spectrum given the input in (a) and (b). (d) Self-carved pulse (blue) with width of $\sim$ 20 ps using Fano resonance, partially carved pulse (dashed red) using Lorentzian resonance, and resonance blue shift (dashed black) induced by the input pulse. (e) Spectrum of the output pulse.

The basic principle of self-carving using an asymmetric red-parity Fano resonance is illustrated in Fig. 5.2 using coupled-mode theory (CMT) simulations [58, 80]. The parameters used in these simulations are shown in Table 4.1. The intrinsic Q-factor of the nanocavity calculated using FDTD and the total Q-factor estimated from theoretical fits are 1.2×10^5 and 1700, respectively. In addition, the amplitude transmission coefficient of the PTE, $t_B \approx 0.55$ is estimated from the fit to the measured resonance transmission of the device shown in Fig. 4.3(b). The transmission spectrum of the device shows a Fano resonance (black line in

Fig. 5.2(a)), with a transmission peak at 1556 nm. The input signal is a 93 ps long super Gaussian pulse of order 2 and with a peak power of 9 mW. Its temporal pulse shape is shown as the blue curve in Fig. 5.2(b) and the corresponding spectrum is shown as the red curve in Fig. 5.2(a), which is centered around the peak of the resonance. The contour plot in Fig. 5.2(c) depicts the time-evolution of the linear transmission spectrum of the PhC system due to the presence of the input pulse calculated using Eq. 5.2. At 0 ps, the input power of the pulse is zero and the contour plot exhibits the initial transmission spectrum of the system. As the amplitude of the input pulse starts to increase, the output pulse amplitude increases until 255 ps, cf. Fig. 5.2(d), after which the intra-cavity field, reflecting the power coupled from the leading pulse edge, becomes high enough that a large number of free-carriers is generated due to two-photon absorption. This changes the refractive index of the nanocavity and hence shifts the resonance towards shorter wavelengths. The resonance shift as a function of time shown in Fig. 5.2(d) (black dashed curve) displays a maximum blue shift of $\sim$ 1 nm corresponding to the spectral separation between the transmission maximum and minimum of the Fano resonance (Fig. 4.3(b)). Therefore, the input pulse, which is centered at the peak of the resonance, encounters a large transmission suppression and the output pulse amplitude reaches its minimum. Because of this, a short pulse of $\sim$ 20 ps (shown in Fig. 5.2(d) by blue solid line) is carved-out of the 93 ps input pulse. For comparison, we also simulated pulse carving using a structure based on Lorentzian resonance with the same Q-factor (red dashed line in Fig. 5.2(d)). However, it displays only partial pulse carving under the same conditions. In contrast, the asymmetric Fano resonance shows complete pulse carving due to the steep slope between the transmission extrema. The spectrum of the pulse carved using the Fano resonance, obtained by taking the Fourier transform of the output temporal pulse, is depicted in Fig. 5.2(e), showing some spectral broadening.

5.2 Experimental investigations of pulse carving

Figure 5.3 shows the experimental and theoretical results for the output pulse at different power levels of the input pulse. In addition to the pulse shape, the input power level is important since it determines the magnitude of the resonance shift and hence the output pulse width and shape. The input (dashed line) is a 93 ps long Gaussian pulse and corresponding calculated output pulses (solid lines) are shown in Fig. 5.3(a) for power levels increasing from -8 dBm to 2 dBm. For clarity, the output power is normalized to unity at the peak. It is seen that at 0 dBm, a short pulse is generated with its center positioned at the leading edge of the input pulse. Fig. 5.3(b) shows the calculated output-to-input pulse peak power ratio for increasing average input power. This ratio decreases for increasing average input power due to the resonance shift induced at the leading edge of the input pulse, which results in suppressed transmission for a major part of the input pulse.

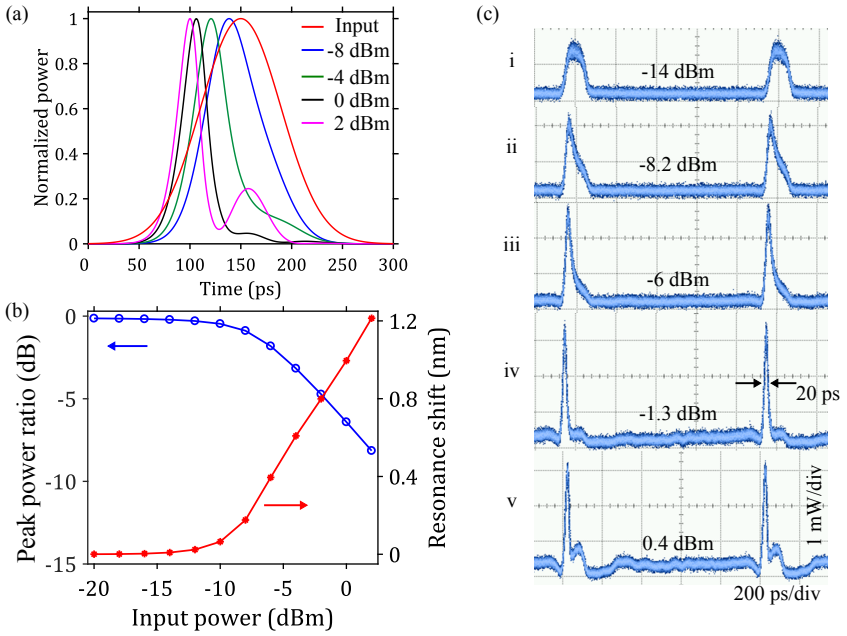

Figure 5.3: Self-carving theory and experiment. (a) Calculated power vs time for a Gaussian input pulse and the carved output pulses for different average input power levels. (b) Calculated output-to-input pulse peak power ratio (blue) and resonance shift (red) for increasing input power. (c) Measured output pulses for average input power increasing from −14 dBm to 0.4 dBm showing different stages of the self-carving process.

Additionally, Fig. 5.3(b) shows the resonance shift for increasing average input power level. This is useful in order to calculate the required input power to shift from the transmission maximum of the Fano resonance to the minimum. Output pulses from the Fano carver measured using a sampling oscilloscope are shown in Fig. 5.3(c). The input pulse train, with 1 GHz repetition rate, is centered at the peak of the Fano resonance (Fig. 4.3(b)). The output pulse at an average input power of -14 dBm is shown in Fig. 5.3(c-i). This pulse has a width close to the input pulse as the input power is low and cannot induce a shift of the resonance. For input power levels of -8.2 dBm and -6.0 dBm, partial pulse carving is observed (ii and iii). In these cases, the resonance shift is not large enough to bring the minimum of the Fano resonance to the spectral position of the input signal. However, by gradually increasing the average input power of the pulse, it is possible to carve-out a pulse with width of $\sim$ 20 ps as shown in Fig. 5.3(c-iv) for

an input power of -1.3 dBm. Furthermore, Fig. 5.3(a) predicts that for an input power of 2 dBm, a side peak appears. This is the result of a large resonance shift, where the minimum of the Fano resonance passes beyond the wavelength at which the input spectrum is centered and leading to increased transmission for the latter portion of the input pulse. Fig. 5.3(c-v) shows the experimental observation of this side peak for input power of 0.4 dBm.

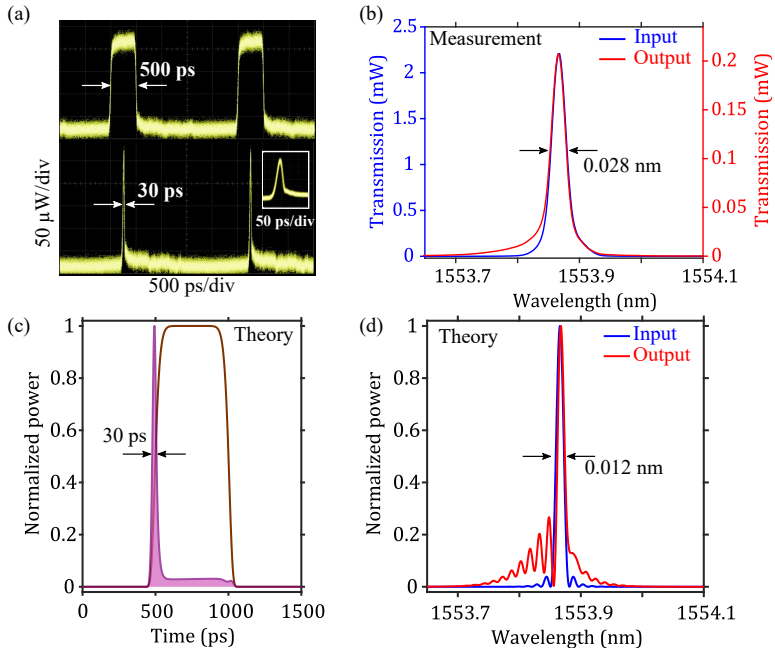

Figure 5.4: Temporal and spectral characterization of self-carving for 500 ps input pulses. (a) Sampling oscilloscope trace of a 500 ps pulse (top) and carved output (bottom) having a width of $\sim$ 30ps for 0 dBm input power. The inset shows a zoom-in view of the output pulse. (b) Measured optical spectra for the input and carved pulses shown in (a). (c) Calculated temporal profile of the input and carved pulse. (d) Simulated optical spectra of the pulses in (c).

Further theoretical and experimental characteristics of self-carved pulses are shown in Fig. 5.4. Sampling oscilloscope traces of 500 ps input pulses (top) and self-carved pulses (bottom), both at 400 MHz repetition rate, are shown in Fig. 5.4(a). When the input power is around 0 dBm, a resonance shift to the minimum of the Fano resonance is possible and hence a short pulse of $\sim$ 30 ps is carved-out of the input pulse. The inset shows a zoomed-in trace of the output pulse. Measured optical spectra of the input and output pulses are presented in Fig. 5.4(b). The full

width at half maximum (FWHM) of the pulses is ~ 0.028 nm, corresponding to a bandwidth of ~ 3.48 GHz at the central wavelength of 1553.86 nm. Note that the measurements are not limited by the resolution of the optical spectrum analyzer (Ando AQ6317B) which is 0.01 nm. The time-bandwidth product (TBP) of the carved pulse is 3.48 GHz $\times$ 30 ps = 0.104. In comparison, a Gaussian chirp-free pulse has a FWHM TBP of ~ 0.44 [81]. To validate the small TBP of the carved pulse, we performed theoretical investigations using CMT. Fig. 5.4(c) shows a 500 ps long super Gaussian flattop input pulse of order 6 and the corresponding self-carved temporal pulse. A super Gaussian pulse is chosen for better agreement with the experiment. The temporal profile of the self-carved pulse shows the generation of a short pulse located at the edge of the input pulse. It can also be observed that the carved pulse has a pulse tail which is not completely suppressed. The power spectrum of these pulses is presented in Fig. 5.4(d). Asymmetric spectral broadening is observed for the self-carved pulse similar to the measured spectrum shown in Fig. 5.4(b). This is because of the mechanism of pulse carving which suppresses the trailing edges of the temporal pulse with less influence on the leading edge. Moreover, the theoretical FWHM for both the input and self-carved output is found to be ~ 0.012 nm and the corresponding TBPs are ~ 0.836 and ~ 0.046 for the input and output pulses, respectively. The small TBP of the output pulse is enabled by the presence of a significant temporal pulse tail which keeps the FWHM spectral bandwidth to remain close to that of input pulse. Further optimization of the slope and transmission contrast of the Fano resonance should be done for complete suppression of pulse tails in which case considerable spectral broadening is expected for the carved pulse.

5.3 Applications of pulse carving

One possible application of such self-carving is for reducing the time slot or duty cycle of RZ-OOK modulated signals. Fig. 5.5(a) shows the eye diagram of a 2 Gbit/s input signal. It is modulated by a PRBS of length of $2^{15} - 1$. It shows that a single channel occupies a time slot of ~ 150 ps and has a pulse width around 100 ps. With the implementation of the Fano resonance based self-carver, it is possible to reduce the time slot to ~ 60 ps and the width to ~ 30 ps (Fig. 5.5(b)). Bit-error-ratio (BER) performance measurements for the reference input and carved output signals as function of received power are shown in Fig. 5.5(c). With an energy consumption down to 1.175 pJ/bit, the carved signal clearly shows error-free performance with a power penalty of ~ 2 dB at the BER of 10^{-9} compared to a 2 Gbit/s input signal measured back-to-back (B2B). The power penalty reflects the additional power required to compensate for the peak power reduction of the carved pulse (cf. Fig. 5.3(b)). These experiments demonstrate that the simple scheme of our Fano structure can be implemented in optical time domain multiplexing systems for achieving high speed on-chip data transmission.

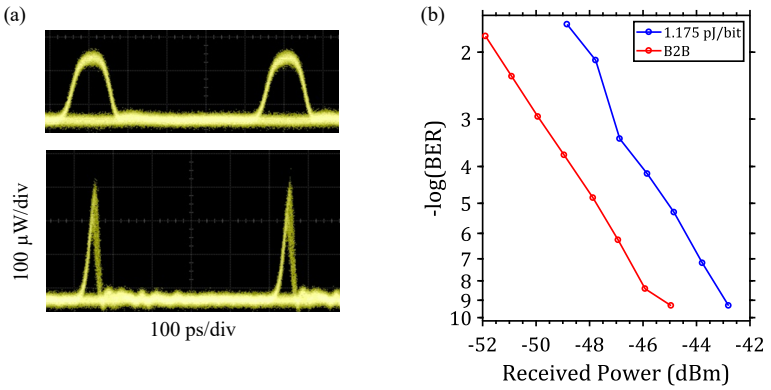

Figure 5.5: Low duty cycle RZ signal generation. (a) Eye diagram of 2 Gbit/s RZ-OOK modulated input signal with a pulse width of $\sim$ 100 ps and duty cycle of $\sim$ 20%. (b) Eye diagram of the carved output RZ signal with a pulse width of $\sim$ 30 ps and duty cycle of $\sim$ 6%. (c) BER performance measurements for the input signal and self-carved low duty cycle RZ signal.

5.4 Limit of pulse carving

Figure 5.6(a) shows that for input pulses with similar rise times ($\sim$ 35 ps) but different widths, the output carved pulses have very similar widths of $\sim$ 20.8 ps. This is because once carrier saturation is achieved in the nanocavity, the resonance will stay at the blue shifted spectral location for the duration of the input pulse which enables the Fano resonance to carve away the remainder part of the pulse regardless of its width. On the other hand, for input pulses having spectral widths larger than the spectral separation of the extrema of the Fano resonance ($\sim$ 1 nm), pulse carving is not effective, as depicted in Fig. 5.6(b). It illustrates the presence of a significant pulse tail corresponding to photons decaying from the cavity hence broadening the output. Therefore, for a Fano resonance with 1 nm separation between the resonance extrema, the shortest input pulse that can be carved is $\sim$ 5 ps.

5.5 Summary

A compact and simple device that carves a short pulse out of a long input pulse without requiring any external modulation is presented. The device relies on the presence of a sharp asymmetric Fano resonance, realized in an InP PhC membrane structure, and a nanocavity-enhanced nonlinear optical effect that shifts the

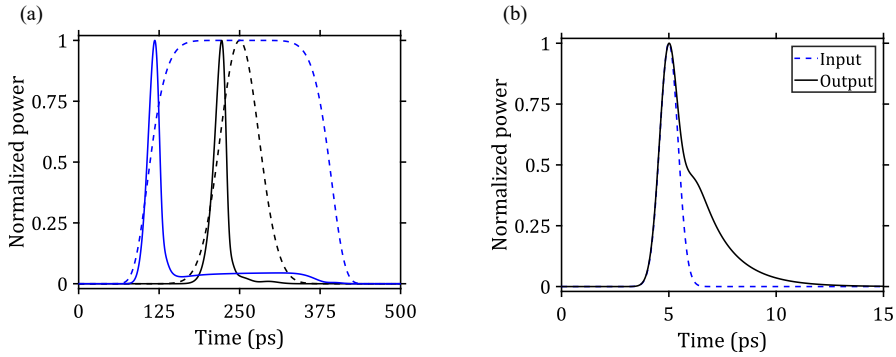

Figure 5.6: Limit of pulse carving. (a) Pulse carving for 50 ps (dashed black) and 118 ps (dashed blue) input pulses to $\sim$ 20.8 ps pulses (solid lines). (b) Device output (solid black) for 1 ps input pulse (dashed blue) with spectral width of ($\sim$ 3.5 nm) at 1550 nm.

Fano resonance to modulate the input pulse itself. Currently, these self-carving experiments are limited to pulse repetition rates less than 5 GHz. This limitation is mainly due to the requirement that a complete recovery of the resonance shift should occur before the next pulse arrives at the nanocavity. For our InP based PhC nanocavities, this recovery time scale is mainly governed by diffusion of charge carriers and the carrier recombination rate [56]. Therefore, to increase the speed, one needs to find ways to increase the rate at which carriers recombine or leave the nanocavity region.

Chapter 6

Signal reshaping and noise-suppression using Fano resonances

6.1 Introduction

This chapter is based on our work reported in [82], and it focuses on applications of Fano resonances for signal regeneration, a process that is used to *clean-up* clean-up a data signal which has been degraded by noise and other signal impairments [83]. It can be performed either electrically or optically. Electrical signal regeneration involves detecting the incoming optical signal and retransmitting it back in the optical domain [19, 7, 84]. Even though electrical regeneration provides very efficient signal regeneration, it consumes high power due to the use of optoelectronic conversion units, which furthermore limit the operation speed leading to transmission bottlenecks [7, 84]. On the other hand, optical regeneration offers substantial benefits due to faster processing speed, while avoiding the use of optoelectronic converters [7, 84, 85].

Complete signal regeneration, for example shown in Fig. 6.1, involves reamplifying, reshaping and retiming hence known as 3R regeneration [83]. For reducing timing jitter of the data signal, clock recovery is first performed followed by transferring the incoming signal to the recovered pulse train [85]. When retiming is absent, the system becomes a 2R regenerator [83]. Reshaping involves signal quality enhancement in terms of noise redistribution, extinction ratio (ER) improvement and pulse compression [83]. Optical amplification used for compensating attenuation and losses is a 1R signal regenerator by itself [19]. An additional class of signal regeneration recently appears due to the development of higher order modulation formats such as quadrature amplitude modulation known as phase regeneration which helps to suppress phase noise of optical signals [84]. Here, we focus on the

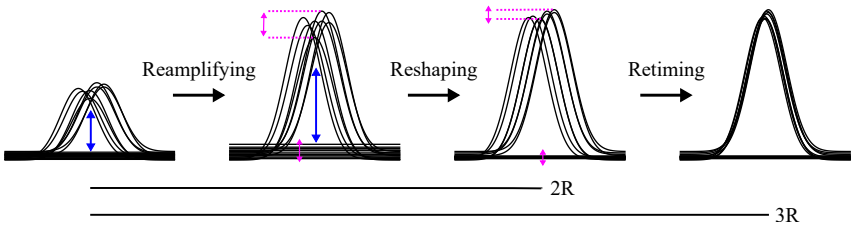

Figure 6.1: Illustration of 3R signal regeneration which involves reamplifying, reshaping and retiming of the input RZ signal. The blue arrows show the extinction ratio of the signal while the purple arrows indicate the amplitude fluctuations.

use of small-footprint and low-energy consumption all-optical devices for signal regeneration, particularly for signal reshaping.

The basic principle of signal reshaping is shown in Fig. 6.2. A noisy data signal having large amplitude fluctuations in the '0' and '1' bit, cf. Fig. 6.2(b), can be improved by a device having an ideal step-like power transfer function shown in Fig. 6.2(a). The resulting clean signal is shown in Fig. 6.2(c) having low amplitude fluctuations and larger extinction ratio (ER) compared to the input noisy signal. In most cases, transfer functions closer to an ideal step functions can be obtained by cascading two or more reshaping stages at the expense of added noise [86]. Each of these stages usually exhibit either one of the power transfer functions shown in Fig. 6.2(d) which are suitable for amplitude fluctuation limiting of the '1' bit [region (i)] and the '0' bit [region (ii)].

Various experimental studies on signal reshaping using integrated photonics have been reported, such as power limiting of 10 Gbit/s non-return-to-zero (NRZ) signals [87] and phase-preserving 20 Gbit/s NRZ quadrature phase-shift keying signals [88] using Lorentzian resonances based on an indium phosphide/silicon (InP/Si) hybrid photonic crystal (PhC) nanocavity. Reshaping, ER improvement, and timing jitter reduction of 10 Gbit/s return-to-zero (RZ) signals have been demonstrated using four-wave mixing in silicon nanowaveguides [89]. Also, ER improvement of a 10 Gbit/s NRZ signal using microdisk lasers integrated on silicon [90], ER improvement up to 2 dB for 1 Gbit/s NRZ signal using a membrane InP switch [91], and reshaping and reamplification of 10 Gbit/s NRZ signals using a semiconductor optical amplifier cascaded with a saturable absorber [92] have been demonstrated.

Here, we demonstrate the use of Fano resonances for all-optical reshaping of RZ data signals. We have experimentally realized two types of Fano resonance lineshapes, i.e. blue and red-parity, whose nonlinear power transfer functions are suitable for suppressing amplitude fluctuations of the '0' and the '1' bit of optical data signals.

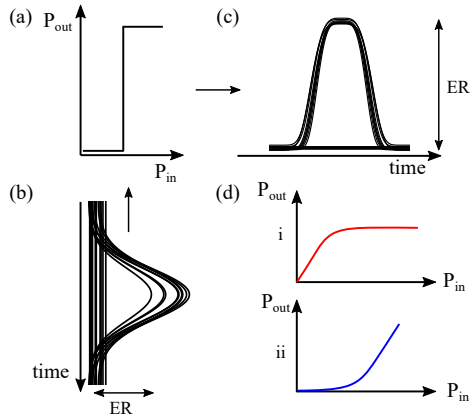

Figure 6.2: Basic principle of signal reshaping. (a) step-like power transfer function of an ideal signal reshaping device. (b) a noisy input optical data signal with small extinction ratio (ER) and large power fluctuations in the '0' and '1' bit levels. (c) reshaped data signal using the transfer function in part (a) resulting in a clean signal with large ER. (d) commonly implemented power transfer functions for suppressing power fluctuations in '1' bit (i) and '0' bit (ii). P_{in} and P_{out} denote input and output powers, respectively.

6.2 Fano structure and resonance lineshapes

The red and blue-parity Fano structures and the resonance lineshapes are shown in Fig. 6.3. As discussed in Chapter 4, red-parity Fano resonance can be realized by placing the PTE airhole in the mid-plane passing through the cavity center, cf. Fig. 6.3(a). On the other hand, blue-parity Fano resonance can be realized by shifting the PTE airhole one lattice constant to the of the mid-plane, cf. Fig. 6.3(c). The total quality (Q) factors of the nanocavities, estimated using coupled-mode theory (CMT) [29] fits to the measurements in Figs. 6.3(b) and 6.3(d), are $Q \approx 1700$ and $Q \approx 1000$ for the red and blue-parity Fano resonances, respectively. The intrinsic Q-factor of the nanocavities calculated using 3D finite-difference time domain simulation is $\sim 1.2 \times 10^5$. The field amplitude transmission coefficient t_B is estimated to be 0.55 and 0.5 for blue and red-parity Fano resonances respectively. Furthermore, the ratio of the decay rates γ_1/γ_2 estimated using CMT fits are 1 and 1.5 for the red and blue-parity Fano resonances, respectively. Other parameters used in the simulation are listed in Table 4.1.

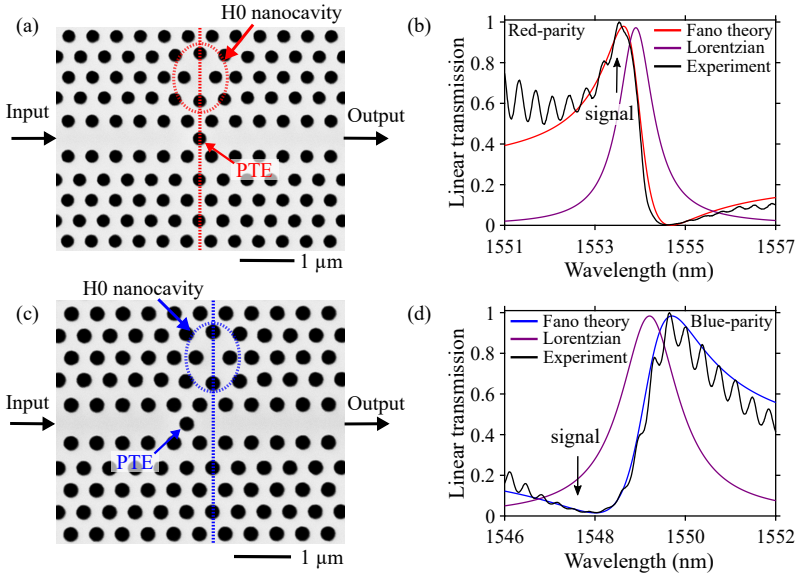

Figure 6.3: Photonic crystal (PhC) Fano structures and resonance lineshapes. (a) Scanning electron microscope (SEM) image of the fabricated PhC with the PTE placed at the mid-plane passing through the cavity center. (b) Measured (black line) and simulated (red) transmission spectrum of the device in part (a) showing a red-parity Fano resonance. It is compared to the transmission of a Lorentzian (purple) resonance having the same Q-factor and resonance wavelength as the red-parity Fano resonance. (c) SEM of the device with the PTE placed one lattice constant to the left from the mid-plane. (d) Measured (black) and simulated (blue) transmission spectrum of the device in part (c) exhibiting a blue parity Fano resonance. It is compared with Lorentzian (purple) transmission having the same Q-factor and resonance wavelength as the blue-parity Fano resonance.

6.3 Nonlinear power transfer functions

Another key feature of our InP photonic crystal platform is the ability to induce a resonance shift using carrier-induced nonlinear effects. Due to the strongly localized nature of the nanocavity mode, a large number of free carriers are generated inside the nanocavity via two-photon absorption (TPA) of the optical input signal [8]. This TPA followed by free-carrier effects results in a reduction of the refractive index and hence a resonance blue-shift [56]. Figure 6.4 presents the nonlinear power transfer functions of the two-types of Fano resonances compared with the case of using Lorentzian resonances. The signal is spectrally centered at the transmission

maximum of the red-parity Fano resonance (1553.6 nm), and at the transmission minimum of the blue-parity Fano resonance (1547.5 nm), as indicated by the arrows in Figs. 6.3(b) and 6.3(d). Furthermore, the red (blue) parity Fano resonance is compared to the Lorentzian resonance, shown in Figs. 6.3(b) and 6.3(d), for which the input signal is placed around its peak (minimum) transmission i.e. 1553.9 nm (1547.5 nm).

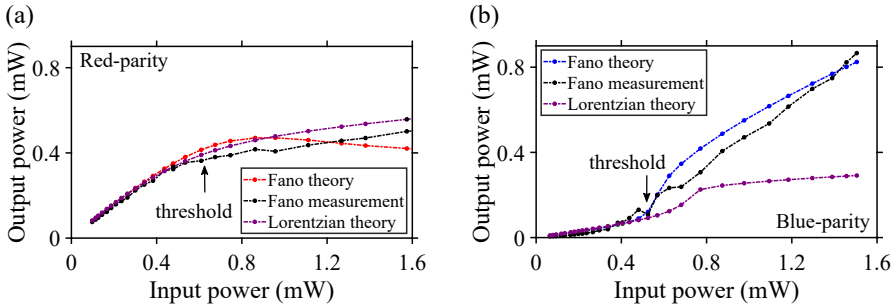

Figure 6.4: Nonlinear power transfer functions of red and blue-parity Fano resonances compared to Lorentzian resonances. (a) Measured (black line) and CMT simulated (red line) power transfer function of red-parity Fano resonance compared with simulated Lorentzian (purple) transfer function. Here, the spectral locations of the input signals are at 1553.6 nm and 1556.9 nm for red-parity Fano and Lorentzian resonances respectively. (b) Measured (black line) and simulated (blue line) power transfer function of blue-parity Fano resonance compared with simulated Lorentzian (purple) transfer function. The spectral location of the input signal is at 1547.5 nm for both blue-parity and Lorentzian resonances.

The red-parity Fano resonance exhibits measured (black line) and calculated (red line) nonlinear power transfer functions as shown in Fig. 6.4(a). The input signal is a train of ∼10 ps pulses with a repetition rate of 10 GHz. Initially, the output power follows the linear increase of the input power. However, as the input power increases above 0.5 mW, the output power saturates. This is because of the induced blueshift of the Fano resonance which results in a transmission decrease at the signal spectral position. Therefore, higher input powers are counterbalanced by an equivalent reduction in transmission leading to saturation. The deviation of the measured transfer function from that of the simulation may be caused by thermal effects which counterbalance the blue resonance shift. However, the comparison to the theoretical result for a Lorentzian resonance predicts that the red-parity Fano resonance has better power saturation due to the steeper transmission lineshape. Note that the arrows in Figs. 6.4(a) and 6.4(b) show the threshold operation points. These points are adjustable by proper choice of the signal spectral detuning

compared to the resonance wavelengths, which determines the fraction of the input power coupling to the nanocavity.

Measured (black line) and calculated (blue line) nonlinear power transfer functions for the blue-parity Fano resonances are presented in Fig. 6.4(b). The input signal is a train of ∼30 ps pulses with a repetition rate of 1 GHz. At low input powers, the transmission through the device is very low since the signal is located around the transmission minimum. However, when the average input power increases beyond 0.5 mW, the resonance starts to blueshift which leads to increased transmission of the signal. This results in saturable absorber-like transmission characteristics. On the other hand, the signal transmission for the Lorentzian resonance starts to saturate for increasing resonance shifts and does not exhibit saturable absorber-like transmission.

Therefore, the device exhibiting a red-parity Fano resonance displays nonlinear saturation of the power transmission, while the blue-parity device is suitable for applications requiring saturable absorber-like transmission, cf. Fig. 6.2(d). These functionalities could help to limit amplitude fluctuations of the '1' and '0' bit of optical data signals.

6.4 Signal reshaping experiments

In this section, we present experimental investigations of the application of the red-parity Fano resonance for signal reshaping of optical data signals, suppressing amplitude fluctuations of the '1' bit and generating a better quality signal.

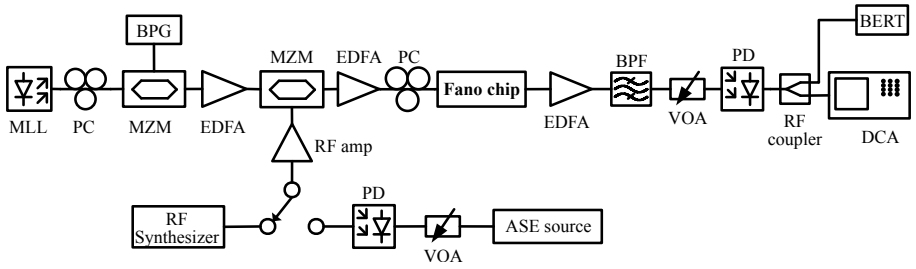

Figure 6.5: Measurement setup for signal reshaping experiments. Light from a mode-locked laser (MLL) is on-off keying (OOK) modulated at 2 Gbit/s and 10 Gbit/s in a Mach-Zehnder modulator (MZM) driven by a PRBS of $2^{15} - 1$ generated by a bit-pattern generator (BPG). Intensity fluctuations either from an RF synthesizer or from a random noise source are added to the RZ-OOK signal using a second MZM. This degraded input signal is then fed to the Fano device and the reshaped signal is analyzed at the receiver using bit-error ratio test (BERT) and the eye diagrams are measured using a digital communication analyzer (DCA).

Our signal reshaping experimental setup is shown in Fig. 6.5. Light from a mode-locked laser (MLL) is polarization controlled (PC) and on-off keying (OOK) modulated at 2 Gbit/s or 10 Gbit/s in a Mach-Zehnder modulator (MZM) driven by pseudo-random bit-sequence length of $2^{15} - 1$ generated by a bit-pattern generator (BPG). Two implementations of intensity noise were introduced on the optical signal. The first employs a signal generated by a radio frequency (RF) synthesizer operated at 500 MHz while the second is a random noise source, implemented using an amplified spontaneous emission (ASE) source, whose output power is controlled by a variable optical attenuator (VOA) before launching into a photodiode (PD). The RF signal from either source is used to drive a second MZM, which imposes these intensity fluctuations on top of the reference *clean* RZ-OOK signal to emulate a degraded input signal. The resulting signal is amplified using an erbium-doped fiber-amplifier (EDFA) and coupled into the photonic crystal red-parity Fano chip, which suppresses amplitude fluctuations giving rise to a cleaned signal. This reshaped signal is then compared to the reference and degraded input signals at the receiver by measuring eye diagrams using a digital communication analyzer (DCA) oscilloscope and bit error ratio using a bit-error ratio tester (BERT). Reference and degraded signals are measured after passing through an on-chip reference waveguide.

Results for the signal reshaping measurements are presented in Fig. 6.6. Here, we have investigated the noise suppression performance of the device towards intensity noise generated by a 500 MHz sinusoidal signal. The frequency of the sinusoidal signal is selected so that amplitude fluctuations are slower than the modulation speeds of the data signals, which are at 2 Gbit/s, 5 Gbit/s, and 10 Gbit/s. Figure 6.6(a) shows eye diagrams for a 2 Gbit/s modulated reference signal (top), degraded signal (middle) and the reshaped signal (bottom). It can be inferred that the amplitude fluctuations in the '1' bit level are reduced, improving the eye opening of the reshaped signal. To quantify this, measured BER as function of received power are shown in Fig. 6.6(b). The reshaped signal shows a 2 dB receiver sensitivity improvement compared to the degraded signal at a BER of 10^{-9}. Similarly, the measurements were performed for 5 Gbit/s and 10 Gbit/s RZ-OOK signals. The eye diagrams for the reference, degraded and reshaped are shown for 5 Gbit/s and 10 Gbit/s in Figs. 6.6(c) and 6.6(e), respectively. Additionally, Fig. 6.6(d) and Fig. 6.6(f) show that the reshaped signals have 1 dB and 2 dB receiver sensitivity improvement at a BER of 10^{-9} for 5 Gbit/s and 10 Gbit/s signals, respectively. The energy consumption of the devices for these noise suppression experiments are estimated to be 104 fJ/bit, 118 fJ/bit, and 41 fJ/bit for 2 Gbit/s, 5 Gbit/s, and 10 Gbit/s, respectively.

Intensity fluctuation of data signals in real systems, however, do not have a fixed frequency as investigated in the experiments above. Therefore, we used the random noise source, cf. Fig. 6.7, which has a bandwidth twice as large as the highest data modulation speed. The histogram of the noise distribution is shown

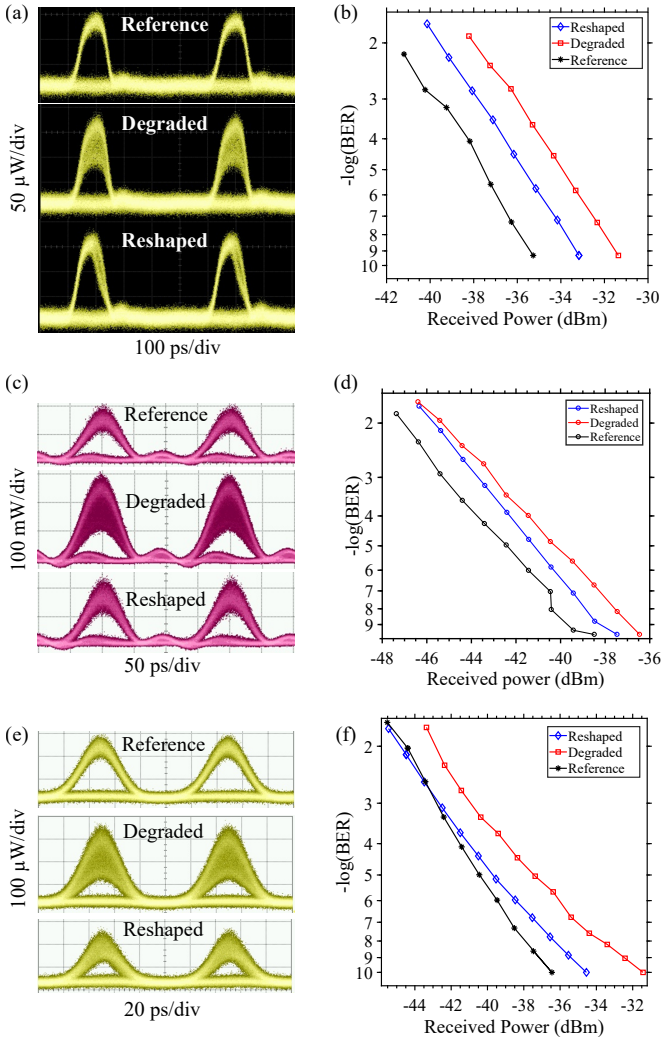

Figure 6.6: Noise suppression of RZ-OOK signals using red-parity Fano resonance. (a), (c) and (e) show RZ-OOK eye diagrams of 2 Gbit/s, 5 Gbit/s, and 10 Gbit/s modulated reference signals without noise (top), the input degraded signal with 500 MHz intensity noise (middle), and the reshaped signal (bottom), respectively. BER performance measurements for 2 Gbit/s, 5 Gbit/s and 10 Gbit/s are shown in (b), (d), and (f), respectively.

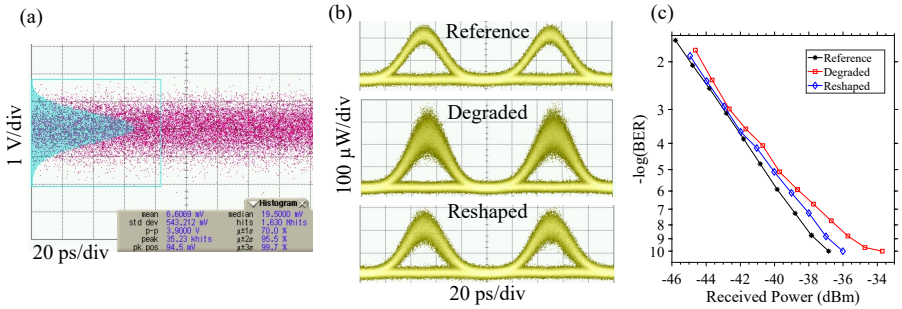

Figure 6.7: Suppression of random intensity noise. (a) histogram of the generated random noise showing Gaussian distribution (b) Eye diagrams of 10 Gbit/s RZ -OOK for the reference (top), degraded with random noise (middle), and reshaped (bottom) signals. (c) the BER measurements for signals shown in part (a).

in Fig. 6.7(a). The eye diagrams for the reference signal (top), degraded signal with random noise (middle) and reshaped signal (bottom) are shown in Fig. 6.7(b). Additionally, the BER performance measurements are shown in Fig. 6.7(c). The reshaped signal (blue) shows a 1 dB receiver sensitivity improvement at a BER of 10^{-9} compared to the degraded signal (red) with an energy consumption down to 47 fJ/bit.

6.5 Discussion

In this section, we discuss the device limitations, choice of input signal bandwidth, and the prospects of further improving the device performance for signal reshaping applications. For these experiments, operations at data rates higher than 10 Gbit/s is not achieved. This limitation is due to the slow recovery of the device, which is estimated to be around 12 ps [93]. Our red-parity Fano resonance device fails to suppress noise fluctuations of signals with average power levels beyond the level at which the resonance shifts past the minimum of the transmission. This is because high input powers will introduce pulse carving effect which distorts the pulse shape [72]. Due to this, the Fano resonance structure cannot be employed to power-limit NRZ modulated signals, which have higher average power than that of RZ signals [2], as shown in Fig. 6.8. The NRZ 'reshaped' eye diagram shown in Fig. 6.8 shows that the device adds more fluctuation. On the other hand, from the CMT based calculations, the Lorentzian resonance shows less pulse distortion effect even at higher input power levels since larger resonance shifts are always accompanied by lower signal transmission due to the monotonous decrease of the transmission

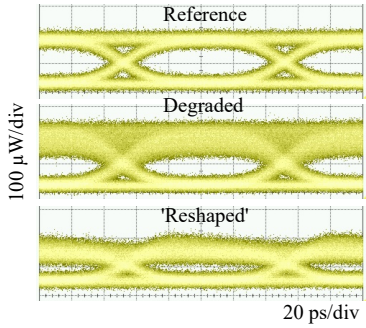

Figure 6.8: 10 Gbit/s NRZ signal reshaping using red-parity Fano resonances. Eye diagrams for the reference signal (top), degraded signal with 500 MHz intensity noise (middle), and the supposedly '*reshaped*' signal (bottom). It shows that NRZ signal reshaping using red-parity Fano resonance is not convenient.

off the resonance peak. So the Lorentzian structure is particularly advantageous for noise suppression of NRZ signals, as demonstrated in Ref. [87, 88].

The limitation of our blue-parity Fano resonance is that the spectral overlap between the cavity resonance and the input signal, which is placed spectrally blue detuned from the minimum of the Fano resonance, is small. This reduces the fraction of the input power coupling to the nanocavity leading to an inefficient nonlinear process. This could be improved by designing the cavity resonance frequency to be closer to the transmission minimum of the Fano resonance. One can achieve this by optimizing the transmission coefficient of the PTE and the Q-factor of the nanocavity, hence enhancing the power coupling into the nanocavity.

The choice of input signal bandwidth depends on several factors. For the present device, the red-parity Fano resonance has a total Q-factor around 1700, corresponding to a photon life time of ~ 1.4 ps and a cavity linewidth of ~ 0.9 nm, assuming Lorentzian lineshape. Considering a blue-shift of the resonance corresponding to a full swing from transmission maximum to minimum spectral location, the input signal must have a bandwidth that is smaller than the Fano extrema separation, i.e. 1 nm. This ensures that the transmission of the input signal is strongly modulated because of the nonlinear resonance shift [94]. Assuming Gaussian pulses, we have found that the shortest input pulse should be ~ 5 ps [72]. For our experiments, we have used mode a locked laser source generating ~ 10 ps pulses corresponding to signal bandwidth of ~ 0.35 nm. For a given signal bandwidth, the Fano device is optimized, with the coupling to the waveguide and the radius of the airhole being the primary design parameters.

The reshaping experiments presented in this work are simplified proof-of-

concept demonstrations of the device performance. In real reshaping and regeneration experiments, cascaded fiber transmission links, e.g. via the use of a recirculating loop, should be implemented in which case the properties of fiber links such as dispersion and propagation losses have to be taken into account, truly demonstrating the regeneration property of the device for minimizing noise accumulation [95].

6.6 Summary

All-optical signal reshaping applications using InP photonic crystal Fano resonance structures is presented. By combining two types of sharp asymmetric Fano resonance lineshapes with efficient carrier-induced nonlinear effects in the nanocavity, nonlinear power transfer functions have been measured and validated. Using these nonlinear transfer functions, we proposed the use of red-parity and blue-parity Fano resonances for suppressing noise fluctuations of the '1' and '0' bit levels of optical data signals respectively. The noise suppression functionality of the red-parity Fano resonance is demonstrated for RZ-OOK modulated signals up to 10 Gbit/s with low energy consumption down to 41 fJ/bit. Additionally, we have shown that the use of blue-parity Fano resonances is effective for the realization of a saturable absorber-like threshold.

Chapter 7

All-optical switching using Fano resonances

7.1 Introduction

The capacity of optical communication links has been growing very fast as a result of dense modulation formats, various multiplexing schemes, the use of multi-core fibres and other developments. However, switching data packets in data centres between such high speed optical links is still one of the main causes of bottlenecks [4]. This is mainly due to the need for conversion from the optical domain to the electrical domain and vice versa for switching and signal processing. The use of optical switches is believed to enable signal processing in the optical domain without the need for conversion to the electrical domain, hence avoiding bottlenecks and reducing the energy consumption [10, 2, 4]. This chapter focuses on wavelength conversion and optical time domain demultiplexing applications of InP photonic crystal Fano resonances reported in [60, 96, 93].

7.2 Model based on coupled-mode theory

Let us briefly discuss the extension to our CMT simulation model, discussed in Chapter 4, in order to account for pump-probe based all-optical switching. Here, the photonic crystal cavity is excited by a relatively high power pump pulse, which triggers the nonlinear processes in the cavity. After an adjustable time delay, a second signal is used to probe the excited cavity similar to the works reported in [56, 60, 12].

Compared to the discussions in chapters 5 and 6, here we inject two optical signals into the photonic crystal Fano switch. Therefore, the rate of change of the cavity field amplitude of the probe and pump signals can be written using Eq. (4.25) as [56]

$$\dot{a}_s(t) = (-\gamma_v - \gamma_{in} - i(\omega_0 + \Delta\omega_s(t) - \omega_s))a_s(t) + \sqrt{2\gamma_1}e^{i\theta_1}s^i_{s+}(t)\,, \tag{7.1}$$

$$\dot{a}_p(t) = (-\gamma_v - \gamma_{in} - i(\omega_0 + \Delta\omega_p(t) - \omega_s))a_p(t) + \sqrt{2\gamma_1}e^{i\theta_1}s^i_{p+}(t)\,, \tag{7.2}$$

where $a_s(t)$ and $a_p(t)$ are the cavity field amplitudes for the probe and pump signals, respectively. The complex resonance shifts for the probe and the pump signals can be written using Eq. (4.26) [56]

$$\begin{aligned}\Delta\omega_s(t) = &-\big(K_{kerr}|a_s(t)|^2 - K_{car}N_c(t) + K_{th}\Delta T\big)\\ &- i\big(K_{TPA}|a_s(t)|^2 + K_{FCA}N_c(t)\big)\,,\end{aligned} \tag{7.3}$$

$$\begin{aligned}\Delta\omega_p(t) = &-\big(K_{kerr}|a_p(t)|^2 - K_{car}N_c(t) + K_{th}\Delta T\big)\\ &- i\big(K_{TPA}|a_p(t)|^2 + K_{FCA}N_c(t)\big)\,.\end{aligned} \tag{7.4}$$

In our simulations, we have assumed that the probe signal is much weaker than the pump signal and hence we have only taken into account the resonance shifts and thermal effects caused by the pump signal.

7.3 Wavelength conversion using Fano resonance

Wavelength conversion involves the transfer of a bit pattern from one signal at a specified wavelength to another signal at a new wavelength, without affecting the bit pattern [19]. It can be used to select and change the carrier frequency of a single channel out of a wavelength division multiplexed (WDM) signal. This allows efficient optical packet switching without the need for buffering and synchronization of the optical data packet [97].

A number of experimental demonstrations of all-optical wavelength conversion have been reported using different physical mechanisms and material systems. Optical fiber based implementations using cross-phase modulation (XPM) in nonlinear optical loop mirror (NOLM) configurations [98, 99] and four-wave mixing (FWM) based wavelength converters using highly nonlinear photonic crystal fiber [100, 101] are some examples. Several semiconductor optical amplifier (SOA) based wavelength converters [102, 103] have also been reported. Photonic crystal membrane based converters include 10 GHz wavelength conversion using FWM in GaInP photonic crystal waveguides [104], wavelength conversion of 20 Gbit/s NRZ data signal using a Lorentzian resonance in a hybrid InP/SOI photonic crystal nanocavity [105], 5 GHz wavelength conversion using carrier-induced nonlinearities in coupled GaAs photonic crystal cavities [12], and wavelength conversion of 10 Gbit/s and 20 Gbit/s signals using Fano resonances in InP photonic crystal structure [60, 96]. In

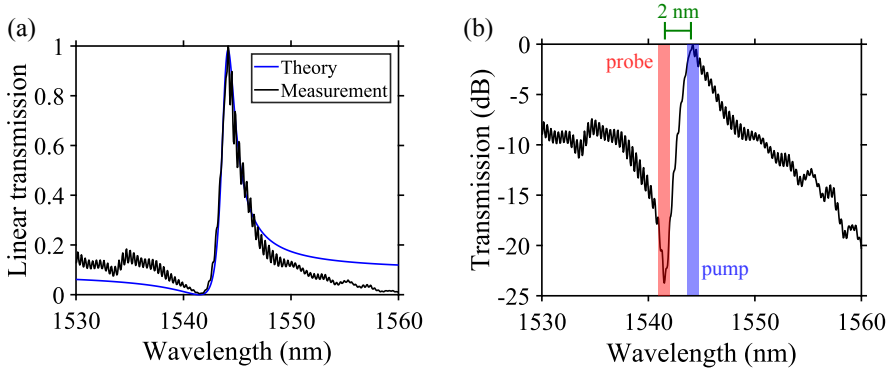

Figure 7.1: (a) Measured (black line) and CMT calculated (blue line) transmission spectrum of blue parity Fano resonance. From the CMT fit to the measurement, the estimated parameters are $t_B = 0.3$, $Q_t = 1000$, and $\lambda_0 = 1543.9$ nm. (b) Measured transmission in dB, showing the transmission difference between the peak and the minimum (the switching contrast) of the Fano resonance to be around 24 dB.

this section we present the Fano resonance based wavelength converters reported in references [60, 96].

Here, a blue-parity Fano structure similar to Fig. 6.3(c) is investigated. The measured transmission spectrum is shown in Fig. 7.1(a) together with a CMT fit. From the CMT fit, we have extracted the amplitude transmission coefficient t_B to be 0.3, the total quality factor of the cavity $Q_t \approx 1000$, $\gamma_1/\gamma_2 \approx 1$, and the resonance wavelength to be 1543.9 nm. From the log scale measured transmission in Fig. 7.1(b), it can be seen that the peak and minimum transmission values differ by ~ 24 dB within a spectral separation of ~ 2 nm.

The experimental setup for wavelength conversion including the eye diagrams of the pump and wavelength converted signals is shown in Fig. 7.2. A 10 Gbit/s RZ-OOK modulated data signal is amplified before combining it with a low power continuous wave (CW) probe signal using a 3 dB coupler. The polarizations of both signals are aligned to the TE-polarization of the wire waveguide, cf. Fig. 3.12. The modulated pump signal is spectrally located at the peak of the Fano resonance (1544 nm) while the CW probe signal is located at the transmission minimum (1542 nm) as shown by the arrows in Fig. 7.1(b). The pump pulse with a FWHM of ~ 10 ps is OOK modulated by a pseudo random bit sequence (PRBS) length of $2^{31} - 1$. This means that the pump signal is a sequence of pulses where the presence of a pulse represents a '1' bit while the absence of a pulse represents a '0' bit.

When the pump signal represents a '0' bit, the resonance will not shift due to no pump power coupled to the nanocavity. Therefore, the probe signal, which is

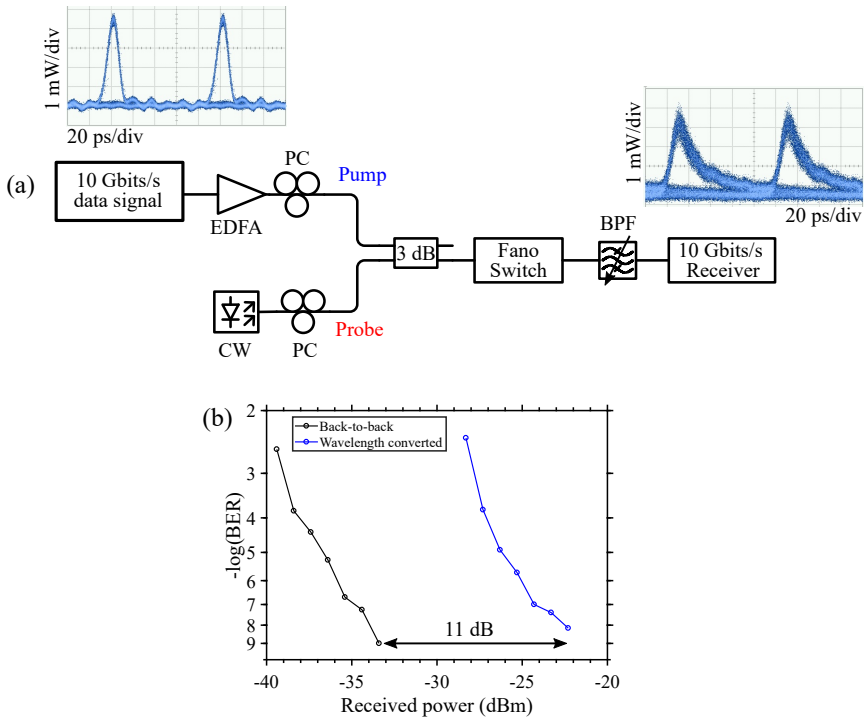

Figure 7.2: (a) Experimental setup for 10 Gbit/s wavelength conversion. A 10 Gbit/s pump signal is amplified and polarization controlled before being combined with a continuous-wave input probe signal. After wavelength conversion by the Fano switch, the pump signal is filtered out and the converted signal is detected by the receiver. The eye diagrams show modulated pump and wavelength converted signals. (b) Bit-error ratio measurement for 10 Gbit/s wavelength conversion. The black line shows the back-to-back measurement while the blue line show wavelength conversion results for pump pulse energies corresponding to 72 fJ/bit.

spectrally located at the minimum transmission of the Fano resonance, will have a suppressed transmission representing the switch-off state of the Fano device. When the pump signal represents a logical bit '1', it will induce a resonance blue-shift, cf. Fig. 4.9(b), due to carrier-induced nonlinear effects in the nanocavity. This results in maximum transmission for the CW probe signal corresponding to the switch-on state of the Fano device.

The wavelength converted data signal is separated from the pump signal using a bandpass filter after which it is amplified and detected by a 10 Gbit/s receiver. The eye diagram of the received signal is shown in the top right corner of Fig. 7.2(a).

Moreover, the wavelength converted signal is quantitatively analyzed using bit-error ratio (BER) measurements as shown in Fig. 7.2(b). Error-free wavelength conversion with energy consumption down to 72 fJ/bit (−4.4 dBm) is demonstrated. It can be seen that a power penalty of ~ 11 dB has occurred compared to the back-to-back (B2B) measurements at a BER of 10^{-9}. The back-to-back (B2B) reference measurements are performed by sending the 10 Gbit/s pump signal directly to the receiver bypassing the Fano switch.

7.4 Optical time domain demultiplexing using Fano resonance

Optical time domain multiplexing (OTDM) is a technique in which N optical signals at the same bit rate B sharing the same carrier frequency are multiplexed to form a composite stream of bits at the bit rate of $N \times B$ [19]. A schematic illustration of an OTDM transmitter based on the delay-line technique is shown in Fig. 7.3(a). It shows that the input periodic pulse trains at the repetition rate equal to the single channel bit rate B is split into four branches. Each of the four branches are modulated using a Mach-Zehnder modulator (MZM). The bit stream in the nth branch is then delayed by an amount $(n-1)/(N \times B)$, where $n = 1$ to 4, using optical fiber segments of controlled lengths, leading to four channels A to D separated in time [19]. These four channels are then recombined to form a composite signal referred to as an OTDM signal having an aggregate bit rate of $4 \times B$. Such a multiplexed system allows high speed transmission and efficient use of the bandwidth [106]. At the receiver end, each of the OTDM channels has to be detected without interference from the neighbouring channels. However, due to limited electronic receiver bandwidth, it is difficult to detect a single channel directly from a high speed OTDM signal [107]. This sets a limit to the highest bit rate at which the system can be operated. On the other hand, optics offers the possibility of operation at much higher speed. Therefore, optical time domain demultiplexing could be implemented to separate the high speed OTDM signal into individual channels which can then be detected by the receiver [106, 108]. Such a demultiplexing process requires a periodic signal at the single channel constituent frequency, known as clock signal, that triggers the demulitiplexing action [19]. A schematic illustration of optical time domain demultiplexing is given in Fig. 7.3(b) in which only channel A is demultiplexed out of the OTDM signal consisting of four channels.

Several works have reported demonstrations of optical time domain demultiplexing using photonic integrated circuit platforms. For instance, 160 Gbit/s to 40 Gbit/s demultiplexing using optoelectronic phase modulation and spectral filtering [108], demultiplexing of 10.56 Gbit/s data stream into 16 or 32 channels using FWM in GaInP photonic crystal waveguides [109], and 170.8 Gbit/s to 42.7 Gbit/s demultiplexing employing FWM in silicon-organic hybrid waveguides [107]. Electro

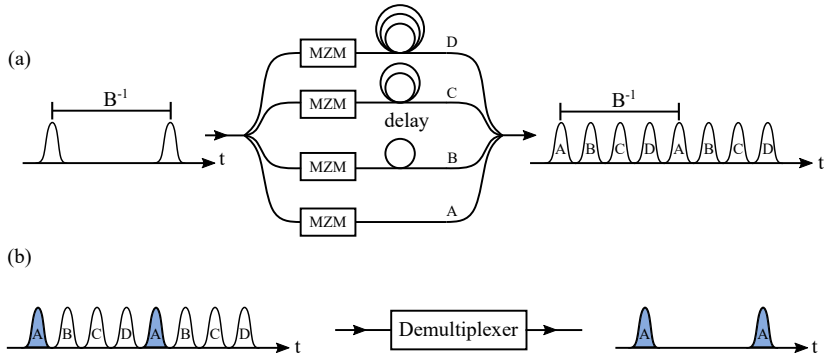

Figure 7.3: Optical time domain multiplexing and demultiplexing. (a) An OTDM transmitter based on the delay-line technique in which four data channels are multiplexed forming a higher data rate signal. (b) An optical time domain demultiplexer selecting only channel A out of an OTDM signal consisting of four channels.

absorption (EA) modulator based 160 Gbit/s to 40 Gbit/s demultiplexing [106], and demonstration of 10 GHz pulse extraction and removal from a signal pulse train at 40 GHz by combining a Lorentzian resonance with carrier-induced nonlinearities in InGaAsP photonic crystal nanocavity [8] have also been reported. Additionally, all-optical demultiplexing of 160 Gbit/s to 10 Gbit/s exploiting slow-light enhanced FWM in a silicon photonic crystal waveguide has been demonstrated [110]. Here, we discuss our work reported on the applications of InP photonic crystal Fano resonances for optical time domain demultiplexing in [93].

We have used the same device as in the wavelength conversion experiment, cf. Fig. 7.1. The measurement setup for optical time domain demultiplexing using a Fano switch is shown in Fig. 7.4. A 40 Gbit/s OTDM probe signal is combined with a train of $\sim$ 10 ps pump pulses using a 3 dB coupler. The OTDM signal is modulated using a PRBS pattern length of $2^{31} - 1$. The pump pulses have a repetition rate of 10 GHz which is the same as the bit rate of a single channel. The time delay of the probe signal compared to the pump signal is adjusted using a delay line, and both signals are coupled to the Fano switch using grating couplers. The spectral locations of the pump and the probe signals are at the peak and minimum transmission points of the asymmetric Fano resonance, similar to the wavelength conversion experiment. The full setup for this demultiplexing experiment is shown in appendix D.

Figure 7.5(a) shows the eye diagrams for the 40 Gbit/s OTDM probe signal (top), the 10 GHz pump signal (middle), and the demultiplexed signal (bottom). When a pump pulse excites the cavity, a blue-shift of the Fano resonance occurs.

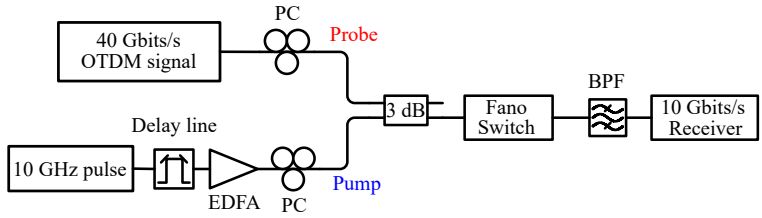

Figure 7.4: Optical time domain demultiplexing measurement setup. A 40 Gbit/s OTDM probe signal and a 10 GHz train of pump pulses are combined using a 3 dB coupler. The time delay between the two signals is adjusted using a delay line. After demultiplexing using the Fano switch, the pump signal is filtered out and the demultiplexed channel is detected by a 10 Gbit/s receiver.

This allows a particular OTDM channel to be transmitted. As soon as the pump pulse leaves the cavity, the resonance shifts back blocking the transmission for the remaining channels. The pump signal is then filtered out using a bandpass filter (1 nm), and the demultiplexed signal is detected using a 10 Gbit/s receiver. The demultiplexed signal is analyzed using BER measurements as shown in Fig. 7.5(b). The BER measurements of the 10 Gbit/s demultiplexed signal clearly show error-free performance with a power penalty of ~ 11 dB at a BER of 10^{-9} compared to B2B measurement. Switching energy of approximately 63 fJ/bit (-2 dBm) was required for the pump pulses in these demultiplexing measurements. For these devices, the input coupling losses were 6 dB. The back-to-back (B2B) reference measurements are carried out by sending a 10 Gbit/s signal directly to the receiver bypassing the Fano switch.

Comparison between each of the four demultiplexed channels in terms of the received optical power required to achieve a BER of 10^{-4} is presented in Fig. 7.5(c). For each channel, received power levels were recorded for BERs slight above and below 10^{-4}. Then, the received power for achieving a BER of 10^{-4} is found by linear interpolation. The received power measurement uncertainty is around 0.5 dBm. It can be seen from Fig. 7.5(c) that all the four channels can be demultiplexed with similar optical power at the receiver, approximately -27 dBm.

From the eye diagram of the demultiplexed 10 Gbit/s signal, cf. Fig. 7.5(a), we can roughly estimate that the total rise and fall time of the switch to be around 25 ps. This corresponds to the time slot that a single channel occupies in the 40 Gbit/s OTDM signal. Furthermore, we estimated the recovery of the device, defined as the time it takes for the transmission to drop to $1/e$ of its peak value, is ~ 12 ps. Note that this recovery time is longer when compared to the values

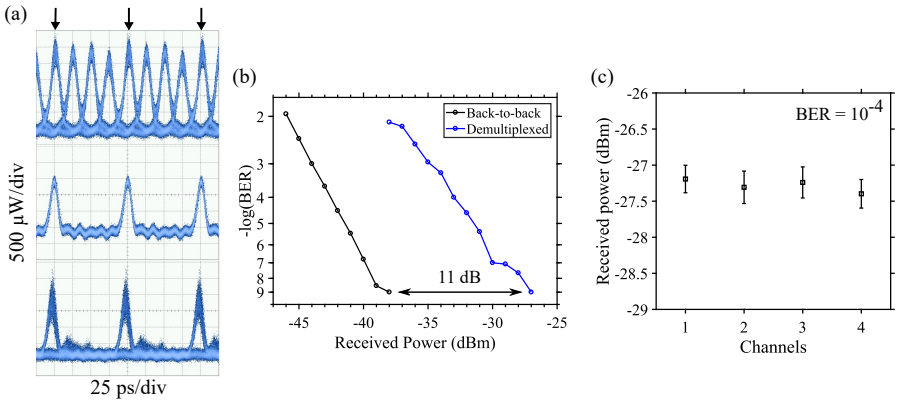

Figure 7.5: Optical time domain demultiplexing using Fano resonances. (a) Eye diagrams of the 40 Gbit/s input OTDM data signal (top), the 10 GHz pump signal (middle), and the demultiplexed signal (bottom). (b) BER measurements for demultiplexed signal, corresponding to a pump energy of 63 fJ/bit, and back-to-back measurement. (d) Comparison of the four demultiplexed channels in terms of received power to achieve a BER of 10^{-4}.

reported for GaAs photonic crystal cavity switches, i.e. ~ 6 ps [111].

While the 40 Gbit/s to 10 Gbit/s optical time domain demultiplexing using a simple and small footprint device serves as a proof of principle demonstration, demultiplexing at higher data rates > 80 Gbit/s is required for practical applications. This is partly because current electronic receiver technology can easily detect a 40 Gbit/s signal without the need for demultiplexing [106, 107]. We start our investigation by assuming that we have an 80 Gbit/s OTDM signal consisting of 8 channels each occupying a time slot of 12.5 ps. We would like to demultiplex one of the channels using a photodetector having response time of 100 ps corresponding to a single channel bandwidth of 10 GHz. The response time of the photodetector corresponds to integrating over these 8 bit periods. Depending on the amount of energy carried by the signal during this integration time, the receiver decides whether a '0' or a '1' bit is received. To avoid having to test all the possible bit sequences, we focused on the worst case scenario, where the difference between the signal energy arriving at the detector for demultiplexing '0', and '1' bits is minimal [94]. Figure 7.6 shows this worst case scenario analysis for demultiplexing an 80 Gbit/s OTDM signal to 10 Gbit/s. For this analysis, we have used the Fano resonance parameters from Fig. 7.1(a). The maximum signal energy that can be received in the case of demultiplexing a '0' bit is when the following 7 channels are all representing '1' bit. This case is shown in Fig. 7.6(a). On the other hand,

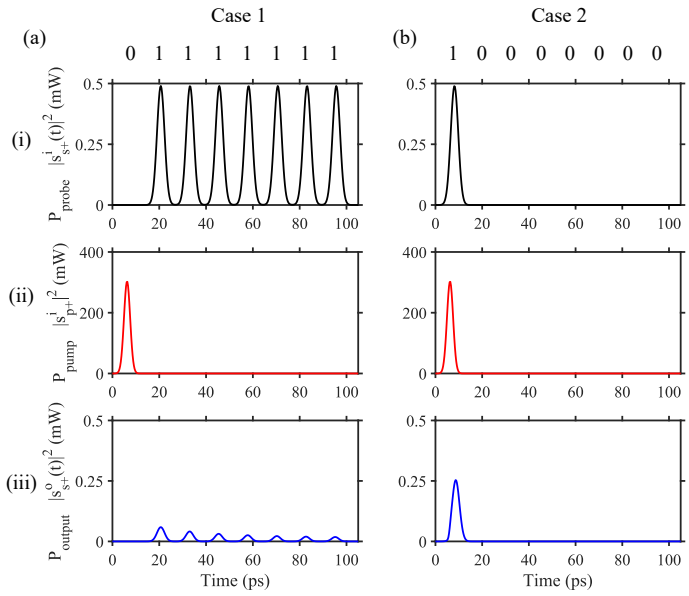

Figure 7.6: Worst case scenario analysis of 80 Gbit/s to 10 Gbit/s demultiplexing for two extreme limits (a) case 1: a bit '0' that is required to be demultiplexed is followed by 7 consecutive '1's. (b) case 2: a bit '1' that is required to be demulitplexed is followed by 7 consecutive '0's. The probe signals in region (i) show the input signals waveform. The pump signals are shown in region (ii), and the demultiplexed signals are shown in region (iii).

the minimum signal energy that can be received in the case of demultiplexing a '1' bit is when the following 7 channels are all representing '0' bit, cf. Fig. 7.6(b). A figure of merit (FoM) can be defined to quantify the ability of the photodetector to distinguish between the demultiplexed '0' and '1' bits as [94]

$$FoM = \frac{U_2}{U_1} \tag{7.5}$$

where U_1 and U_2 represent the total signal energy received in case 1, and case 2, respectively. In general, a $FoM > 1$ is desired, otherwise errors may occur in the demultiplexing process.

In Fig. 7.6 regions (i) and (ii) represent the OTDM probe and the pump signals for the corresponding bit sequences in case 1 and case 2. The probe and pump signals are assumed to be Gaussian pulses with FWHM of 3.8 ps and 3 ps respectively. The FWHM of the probe is chosen in order to fit the pulse time slot

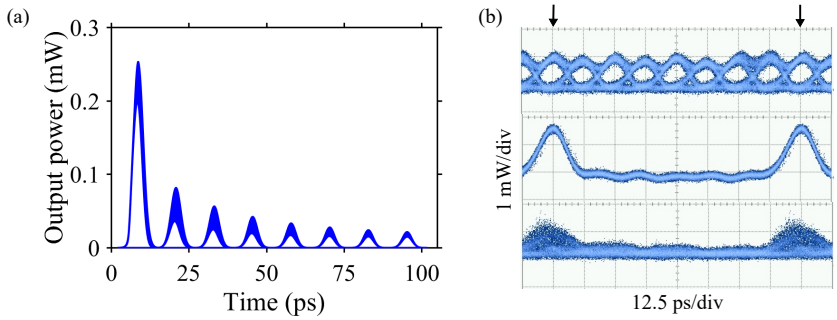

Figure 7.7: (a) Simulated eye diagrams for 80 Gbit/s to 10 Gbit/s demultiplexing using a PRBS length of $2^{15} - 1$. It can be seen that the transmission of the neighbouring channels is suppressed, but not completely switched off. (b) Measured eye diagrams of 80 Gbit/s OTDM signal (top), 10 GHz pump signal (middle), '*demultiplexed*' signal (bottom). It can be observed that the device is not able to clearly demultiplex the selected channel.

within 12.5 ps. On the other hand, the FWHM of the pump is chosen to maximize the FoM while keeping the spectral overlap with the probe signal at a minimum in order to avoid cross-talk. The average input powers for the probe and pump signals are set to -8 dBm and 10 dBm respectively. Again, the power of the pump is selected in order to maximize the FoM. Moreover, the probe signal is delayed by 2 ps compared to the pump signal. This ensures that the carrier induced nonlinear processes in the cavity lead to maximum transmission within the time slot of the selected OTDM channel. It can be inferred from Fig. 7.6 region (iii) that the transmission of the successive channels have been suppressed (case 1), while the peak transmission that can be achieved in case 2 is half of the peak power of the probe signal, indicating a possible source of power penalty. In this case, the calculated FoM is 1.2.

Figure 7.7(a) shows examples of eye diagrams simulated for 80 Gbit/s to 10 Gbit/s demultiplexing using a PRBS length of $2^{15} - 1$. The first channel is demultiplexed, while the transmission for neighbouring channels is suppressed but not completely switched off. Figure 7.7(b) shows measured eye diagrams for 80 Gbit/s OTDM signal (top), 10 GHz pump pulse (middle), and a supposedly demultiplexed 10 Gbit/s signal (bottom) using a PRBS length of $2^{31} - 1$. Owing to the digital communication analyzer bandwidth (40 GHz), the eye diagram for the 80 Gbit/s signal is distorted. Unfortunately, it was not possible to successfully demultiplex a single channel, as can be observed from the closed eye diagram in the bottom of Fig. 7.7(b). This is due to the slow carrier relaxation time causing long transmission tail [56, 68], which can be clearly seen from the wavelength converted eye

diagram of Fig. 7.2(a). This slow carrier relaxation time is dominated by surface recombination process, as discussed in Section 4.3.1.

7.4.1 Switching at GHz rates

In this subsection, we would like to note a few general remarks on the response of the photonic crystal cavity structure when operated at GHz regime. It is important to note the two distinct time scales associated with the thermal and carrier relaxation times around the cavity. The thermal relaxation times are in microseconds time scales, while the carrier relaxation times are in picoseconds range [36, 111]. Generally, at GHz repetition rate the cavity dynamics is dominated by the carrier relaxation, while operations at MHz repetition rates could significantly be dominated by thermal effects [36].

For the 10 Gbit/s wavelength conversion, the major part of the probe transmission induced by the pump recovers within tens of picoseconds, as shown by the eye diagram in Fig. 7.2(a). If the repetition rate increases beyond 10 GHz, the probe transmission will experience incomplete recovery due to the slow component of the carrier relaxation rate. This result in carrier build-up and hence lower modulation of the probe signal. This deterioration of the switching performance is known as the patterning effects [56, 12].

Switching at GHz repetition rates also results in larger thermal effects due to the higher average power levels of the pump signal. This leads to red-shifting of the cavity resonance due to the thermo-optic effect at much slower time scales, in microsecond regime [36, 12].

For the wavelength conversion and optical time domain demultiplexing experiments discussed above, the relatively large power penalty (11 dB) originates partly from the patterning effect and partly from the coupling losses into and out of the device. Therefore, efficient reduction of the thermal effects and faster recovery time constants have to be achieved for high speed operation. In following section, we briefly discuss possible solutions for alleviating these issues.

7.5 Towards higher speed all-optical switching

As discussed in the previous section, when the pump power is absorbed via TPA in the cavity, free-carriers accumulate and cause a change in the refractive index leading to a resonance shift. On the other hand, when the pump power is off, accumulated free-carriers relax with time scales determined by the carrier recombination and diffusion rates in InP [56]. This sets a limit to the highest switching speed that can be achieved using carrier induced nonlinearities as opposed to the much faster instantaneous Kerr effect based switches, discussed in Section 2.2.2 [24, 68].

There are few approaches proposed to address these issues. Using a p-doped InP is a simple and effective method towards realizing high speed switching [68]. This allows a transition from the ambipolar diffusion regime to the faster minority carrier (electron) dominated diffusion regime. An approximately twofold acceleration of the carrier dynamics has been reported using p-doped InP photonic crystal in [68]. The diffusion coefficient of electrons and holes in InP is approximately $130\,\mathrm{cm}^2/\mathrm{s}$, and $5\,\mathrm{cm}^2/\mathrm{s}$, respectively [112].

Another possibility is to sweep carriers out of the cavity region by applying a reverse biased voltage across the cavity. This can be implemented using either a p-i-n junction, or a metal-semiconductor-metal (MSM) structure. Successful implementations of carrier extraction in silicon samples across standard strip waveguides [113, 114], and photonic crystal cavities [113, 115] have been reported. Here, we aim for combining this technology with our InP photonic crystal Fano structures for achieving faster switching. A schematic diagram of the structure is shown in Fig. 7.8(a). It consists of p and n-doped regions, and p and n ohmic contacts in addition to the photonic crystal Fano structure. The metal contacts are sufficiently far from the photonic crystal in order to avoid losses. The p and n-doped regions extend up to the cavity region, and the separation between the doped regions is around 600 nm composed of intrinsic InP.

Figure 7.8(b) shows an optical microscope image of the fabricated structure. The device fabrication starts with growth of the InP wafer by metalorganic vapour phase epitaxy (MOVPE). This wafer is then directly bonded to a silicon wafer using the technique reported in [116]. After the substrate removal, several alignment marks that are required for subsequent fabrication steps are defined using a UV lithography process. Using one of these alignment marks, a silica glass mask for the p-doping region is defined using UV lithography followed by a reactive ion etching (RIE). The p-doping of InP is then possible by diffusion of zinc (Zn) using the silica glass mask in the MOVPE chamber. After rapid thermal annealing at 450 °C, the glass mask is removed using buffered hydrofluoric acid (BHF). The wafer is then ready for fabrication of photonic crystal structure, as described in Section 3.2. Note that the membranization process is done after the metal contact deposition, liftoff and thermally annealing processes. The ohmic contact to the n-type InP is made of Ni/Ge/Au metal combinations with 40/50/125 nm thickness, respectively. On the other hand, the ohmic contact to the p-type InP is composed of Ti/Pt/Au metal combinations with 30/50/250 nm thickness, respectively. Note that this sample does not have n-doped region extending into the photonic crystal region due to unavailability of an ion implantation machine in the cleanroom facility. Therefore, the whole InP layer except the p-doped region is intrinsic. However, n-doping under the n-contact is formed by Ge diffusion into InP [117], which allows the formation of p-i-n structure.

The SEM image of the final fabricated device is shown in Fig. 7.8(c). The yellow shaded region illustrates the p-doped region extending to the photonic crystal cavity

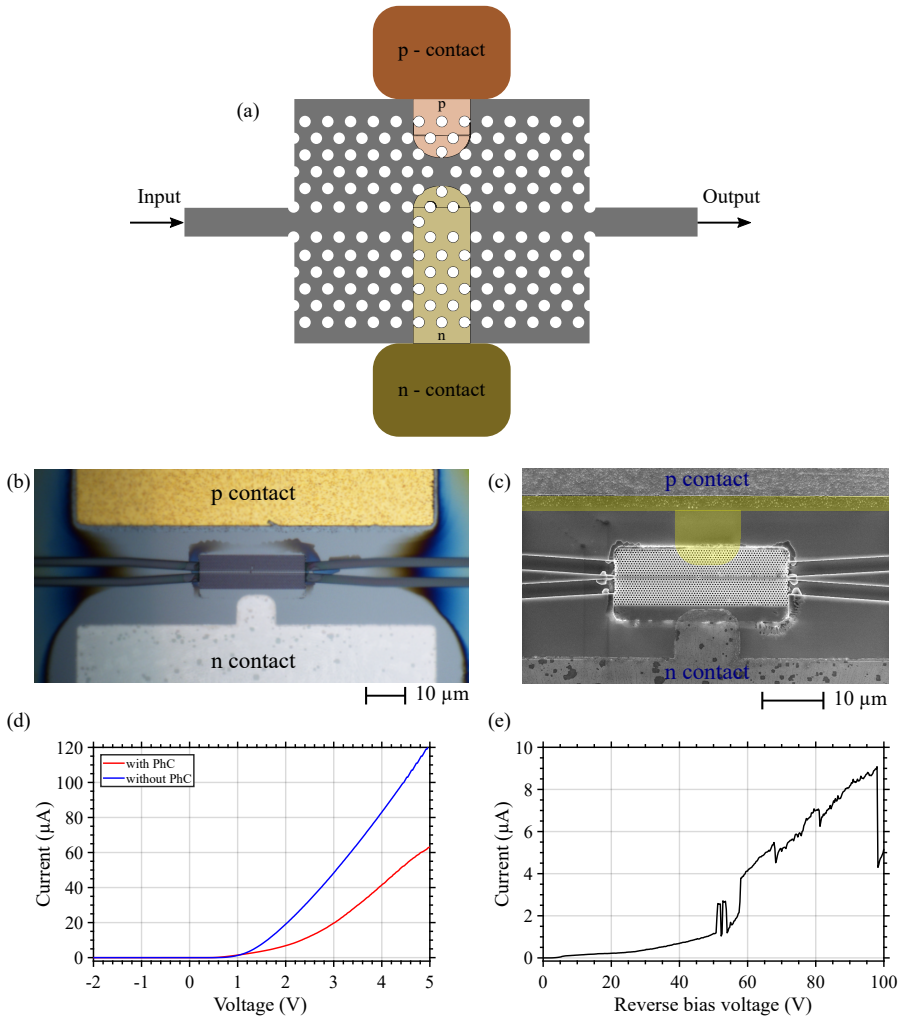

Figure 7.8: InP photonic crystal Fano structure with p-i-n junction for carrier sweeping. (a) A schematic diagram of the device consisting of p and n-doped regions, and p and n-contacts. (b) Optical microscope image of the fabricated device. (c) SEM image of the fabricated device, yellow shaded region shows designed p-doped region extending to the cavity region. (d) Measured I-V curve for a PhC structure, and a test device without PhC pattern (bulk). (e) Reverse bias voltage vs current for the device with PhC structure. The separation between the p-doped region and the n-contact is around 9.5 μm.

region. The separation between the p-doped region and the n-contact is around 9.5 μm. Note that the n-contact is designed to have similar profile as the p-doped region. The p-doping concentration level is around $10^{17}\,\mathrm{cm}^{-3}$.

Figure 7.8(d) shows current-voltage (I-V) characteristic curves for a device consisting of the photonic crystal pattern ($r/a = 0.277$) and a reference device without photonic crystal (bulk) under forward bias case. Here, the positive and the negative terminals of the voltage source are connected to the p-contact and the n-contacts, respectively. Figure 7.8(e) shows the measured reverse bias voltage versus current. In this case, the positive and the negative terminals of the voltage source are connected to the n-contact and the p-contacts, respectively. It can be observed that a reverse bias voltage up to 50 V can be applied across the photonic crystal with leakage current lower than 2 μA. Beyond this critical voltage value the current starts to increase rapidly. For these measurements, there was no input light coupled to the device. For the case in which light is coupled into the cavity, we expect that the photocurrent will significantly be higher at much lower voltage values than this critical voltage.

These electrical characterizations show that the device allows the flow charges in one direction but not in the opposite direction, indicating the formation of the p-i-n junction and hence diode characteristics. We believe that the carrier sweep-out will not be affected too much by the photonic crystal structure [115]. Upon application of reverse bias voltage across the p-i-n junction, depletion region around the cavity can be achieved. Because of the large built-in electric field in the depletion region, electron-hole pairs generated by TPA in the cavity accelerate in opposite directions and drift to the n-and p-sides, respectively. This drifting of carriers out of the cavity region will significantly reduce the lifetime of free-carriers. However, the effect of this reduced effective carrier lifetime on the quality factor of the cavity, and carrier-induced nonlinearities are yet to be investigated. The nonlinear loss in the cavity due to free-carrier absorption is, on the other hand, expected to reduce as a result of carrier lifetime reduction [115].

Optical characterizations of this sample, however, was not successful due to high coupling losses to and out of the device owing to the parameters of the grating couplers being offset from their target values.

7.6 Summary

The switching experiments reported in this chapter, i.e. the wavelength conversion and optical time domain demultiplexing, show the potential of Fano resonance based InP photonic crystal switches for fast and energy efficient all-optical signal processing applications. The recovery time of the device is estimated to be around 12 ps, and energy consumption down to 63 fJ/bit have been achieved. Furthermore, initial experiments on carrier sweeping also show a promising start towards implementation of higher speed all-optical switches. With this configuration, we

expect device recovery times less than 10 ps. Similar investigations reported in silicon photonic crystal cavities shows that effective carrier lifetimes down to 6 ps can be achieved without significantly affecting the quality factor of the cavity [115]. Additionally, the thermal effects around the cavity can be significantly reduced due to faster extraction of carriers. In [113], Tanabe et al. reported that heat generation around the photonic crystal cavity can be reduced to 43 % if the carriers are swept-out within 100 ps, providing the possibility for ultrafast switching. Our future work will be aimed at realizing higher switching speeds using Fano resonances enhanced by the carrier sweep-out mechanism using p-i-n structures across the photonic crystal cavity.

Chapter 8

Conclusion and outlook

In the following, the main results and achievements of this work are summarized and an outlook on future perspectives is given.

8.1 Conclusion

The first challenge that was addressed in this work is the light coupling efficiency into the device. A fiber-to-chip coupling scheme that utilizes surface emitting grating coupler is implemented on InP layer, which is either directly wafer bonded or BCB bonded to a silicon wafer. Coupling efficiency of -3.5 dB per interface is achieved. This grating coupler is also designed to fit into a standard photonic crystal membrane device fabrication process, and it can be adapted to any other III-V semiconductor platform.

The central part of this work has been the study of InP photonic crystal Fano resonance structures consisting of a nanocavity side-coupled to a waveguide. Two types of asymmetric Fano lineshapes, i.e. the red and the blue-parity, have been investigated using coupled-mode theory, and demonstrated experimentally. These asymmetric lineshapes are realized by simply controlling the location of the partially transmitting element airhole in the line-defect waveguide with respect to the mid-plane passing through the center of the nanocavity. This simple technique allow us to exploit different signal processing applications with minimal change on the device structure. The key feature of the asymmetric Fano resonances is the small spectral separation between the peak and the minimum transmission points, typically less than 2 nm with a switching contrast of more than 20 dB. By combining these characteristic lineshapes with carrier-induced nonlinear resonance shifts, compact devices potentially suitable for all-optical signal processing applications have been implemented.

We have demonstrated the use of red-parity Fano resonances for carving-out short pulses from long-duration pulses. For instance, input pulses as long as 500 ps

are experimentally shortened to 30 ps pulses. The shortest pulse that can be carved is around 5 ps, estimated using coupled-mode theory simulations. This self-pulse carving feature is further implemented for low-duty cycle (6 %) RZ-OOK signal generation at 2 Gbit/s with energy consumption down to 1 pJ/bit. This can be used in OTDM systems for generating densely multiplexed signal by reducing the time slot of the constituting channels.

Another application of Fano resonances that we have been investigating is the reshaping and noise suppression of optical data signals. The combination of the asymmetric Fano lineshape with a nonlinear resonance shift is exploited to realize nonlinear power transfer functions suitable for suppression of amplitude fluctuations of RZ data signals. We have shown that red-parity Fano resonance exhibits power-limiting property, while the blue-parity Fano resonance exhibits saturable absorber-like transmission. Using the red-parity Fano device, we have demonstrated reshaping of 10 Gbit/s RZ-OOK signals with energy consumptions down to 41 fJ/bit.

The pulse carving and the signal reshaping demonstrations using Fano resonances can be categorized as self-switching types of signal processing applications. This is because the input signal itself induces the nonlinear effect in the nanocavity and hence the switching action. Using two optical signals, in which the pump signal affects the transmission of the probe signal, we have investigated the switching performances of the blue-parity Fano resonance. *Error-free* 10 Gbit/s wavelength conversion, and 40 Gbit/s to 10 Gbit/s optical time domain demultiplexing applications with energy consumption down to 63 fJ/bit have been demonstrated. From these experiments the $1/e$ recovery time of the device is estimated to be around 12 ps. Here, the Fano resonance lineshape helps to reduce the slow transmission tail of the probe signal compared to that of the Lorentzian resonance. However the device operation speed is still limited by the slow carrier diffusion and relaxation rates. In an effort to further reduce this recovery time, p-i-n junction structure is implemented to sweep carriers out of the cavity region. Preliminary investigation on such structures is also reported.

8.2 Outlook

The achievements of this work concerning the device operation speed and energy consumption serve as proof-of-principle demonstrations. For practical applications, energy consumptions below 10 fJ/bit and operation speeds at 100 Gbit/s are envisaged. A natural starting point could be to continue on the implementation of the p-i-n junction structures across the nanocavity. This could potentially enhance the operation speed by reducing the carrier relaxation time of the device. On the other hand, this comes at an extra energy cost required for applying DC electric field across the cavity region.

Besides the slow carrier relaxation time, the current device suffers significantly

from the cross-talk between the pump and the probe signals, which are closely placed at the peak and the minimum transmission points of the asymmetric Fano resonance. This could be addressed by implementing dual resonance cavity, whose resonances are designed to be sufficiently far apart in spectrum. In this scheme, the pump signal could be placed at one of the resonances, while the probe signal could be placed at the other resonance. Thus effectively eliminating signal cross-talk.

Another issue to investigate is the thermal stability of the device. When operated at high optical power levels, the device undergoes irreversible resonance blue-shift and degradation. This may be solved by atomic layer deposition coating of the sample, which protects the photonic crystal from photo-assisted oxidation. Furthermore, improving the coupling efficiency of the grating couplers, and improving the quality of the photonic crystal in terms of fabricating straight and smooth airholes are desired in order to reduce the energy budget of the device.

Appendix **A**

Carrier-induced changes in refractive index of InP

A summary of change in refractive index of InP due to carrier-induced nonlinear processes is shown in Fig. A.1. It can be seen that bandgap shrinkage and band filling effects are much stronger for photon energies corresponding to the bandgap energy of InP $E_g = 1.34\,\text{eV}$.

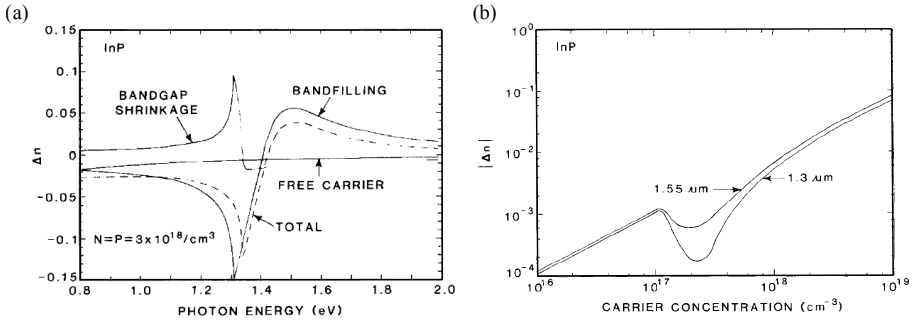

Figure A.1: Carrier-induced change in refractive index of InP. (a) Predicted changes in refractive index from bandfilling, bandgap shrinkage and Free-carrier absorption for carrier concentration level of ($N = P = 3 \times 10^{18}$ cm^{-3}) as a function of the photon energy. The total sum of these contributions is shown in the dashed line. (b) Change in refractive index at $1.3\,\mu$m (0.95 eV) and $1.55\,\mu$m (0.8 eV) for various carrier concentrations. The sign of Δn is negative in all cases in part (b). Figure taken from [28].

We consider operations at the telecom wavelength of around $1.55\,\mu$m (0.8 eV),

at which bandgap shrinkage effects are smaller, cf. Fig. A.1(a). Bandgap shrinkage results in positive changes in the refractive index while bandfilling and free-carrier absorption or plasma dispersion results in negative changes in the refractive index. The total contribution from all these three effects is indicated by the dashed line. In Fig. A.1(a), the three carrier effects are assumed to be independent, hence the total change in refractive index is a simple sum of the effects [28]. Figure A.1(b) shows the total estimated change in refractive index for InP as a function of carrier concentration for two wavelengths, $1.3\,\mu$m and $1.55\,\mu$m. In our experiments, we have achieved typical resonance shift of 1 nm, this corresponds to $\Delta n = n\Delta\lambda/\lambda_0 \approx 2 \times 10^{-3}$, where $\lambda_0 = 1550\,$nm, and $n = 3.17$ is the refractive index of InP [111]. This indicates that free-carrier concentrations around $10^{18}\,\mathrm{cm}^{-3}$ can be achieved inside our *H0* photonic crystal cavities, cf. Fig. A.1(b).

Appendix B

Carving of short pulses

The application of the red-parity Fano resonance for carving input pulses shorter than 20 ps at 1 GHz repetition rate is presented in Fig. B.1. It shows the autocorrelation measurements and the corresponding optical spectra. Figure B.1(a) shows the autocorrelation intensity for a 14.5 ps input pulse (blue line) and output pulse (red line). When the input power is around -8.6 dBm, it is possible to carve out 9.6 ps short pulses (red). The pulse widths are calculated by fitting the autocorrelation intensity assuming Gaussian pulse profile and using the relation FWHM $= \tau/\sqrt{2}$, where τ is the autocorrelation intensity width and FWHM is the estimated full width half maximum of the pulse [81]. Fig. B.1(b) shows the optical spectra of the pulses in part (a). The optical spectra for the carved pulses show asymmetric broadening compared to the input pulse spectrum since the pulse carving process mainly affect the trailing edges of the input pulse. Note that this asymmetric broadening is also obtained using CMT simulations as shown in Fig. 5.2(e) and Fig. 5.4(b & d). For a 20 ps input pulse, the Fano resonance based pulse-carver can create pulses as short as 10 ps with input power of -6 dBm, as shown in Fig. B.1(c). The corresponding optical spectra, cf. Fig. B.1(d), clearly shows the spectral broadening due to the generation of short pulses.

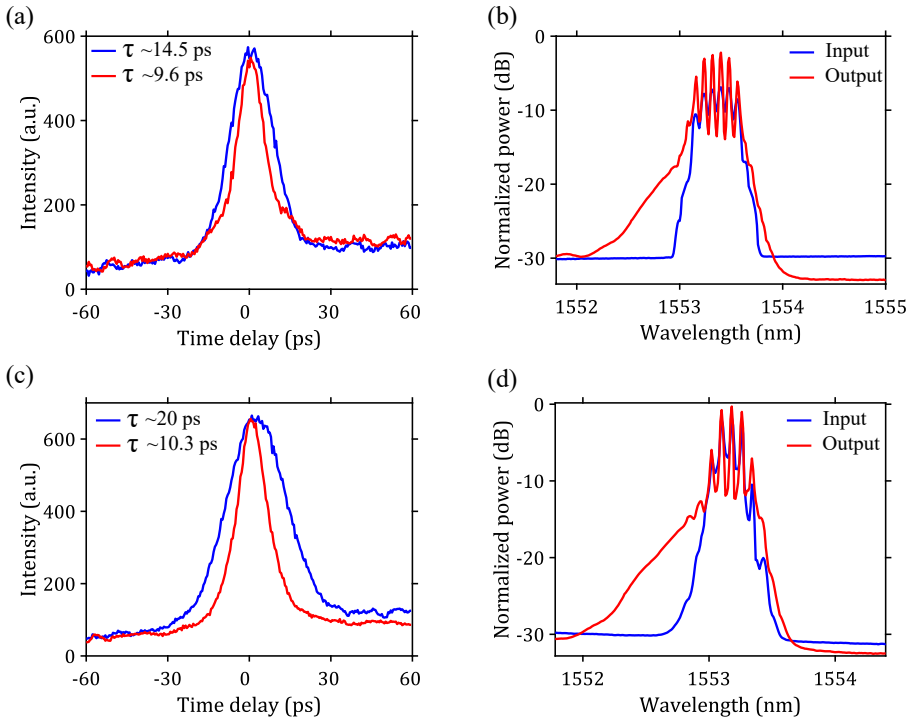

Figure B.1: Autocorrelation intensity measurement and optical spectra. (a) shows the pulse profile of a 14.5 ps wide input pulse and output pulse of 9.6 ps. (b) The corresponding optical spectra of the pulses shown in part (a). (c) Temporal pulse profiles of the 20 ps input and 10.3 ps output pulses. (d) The optical spectra of the pulses in part (c).

Appendix C

Photo-assisted oxidation of InP photonic crystal cavities

During most of the measurements carried-out in the work, we have noticed that the device undergoes irreversible resonance blue-shift when operated at relatively high power levels. This has greatly affected the stability of the device particularly during long measurements such as BER performance tests. This is due to a photo-assisted oxidation of the cavity region facilitated by the local heating of the cavity during high power operation [12, 118]. Figure C.1(a) shows the spectra for Fano resonance before and after exposure to high optical power, i.e. 9.8 dBm. It can be observed that an irreversible resonance blue-shift of around 3.5 nm has occurred. It is reported in literature [12, 119], that the passivation of GaAs photonic crystal with few nanometers of Al_2O_3 prevents oxidation. It can be shown in Fig. C.1(b) that the resonance of the cavity did not shift after exposure to high optical power, i.e. 14.5 dBm, resulting in a stable transmission spectrum for samples coated with 5 nm ALD Al_2O_3.

We further investigate the effect of ALD coating on the spectral location of the Fano resonance. Figure C.2 shows the comparison between samples coated with 5 nm Al_2O_3, 10 nm Al_2O_3, and uncoated reference sample. Note that the Al_2O_3 coated PhC samples have the same airhole radius as the reference sample before they were coated. The effect coating the sample is that the resonance wavelength shifts to longer wavelength due to the narrowing of airhole by the thin layer of Al_2O_3. An average resonance shift of around 8 nm, and 15 nm is observed for samples coated with 5 nm, and 10 nm of Al_2O_3, respectively. Moreover, the switching contrast of the Fano resonance for coated samples has reduced compared to the reference uncoated sample. The switching contrast of the Fano resonance is reduced from a typical value of 20 dB to around 10 dB, when the sample is coated with 5 nm of Al_2O_3, as shown in Fig. C.1(b).

So far we have not studied the effect of ALD coating on the Q-factor of the

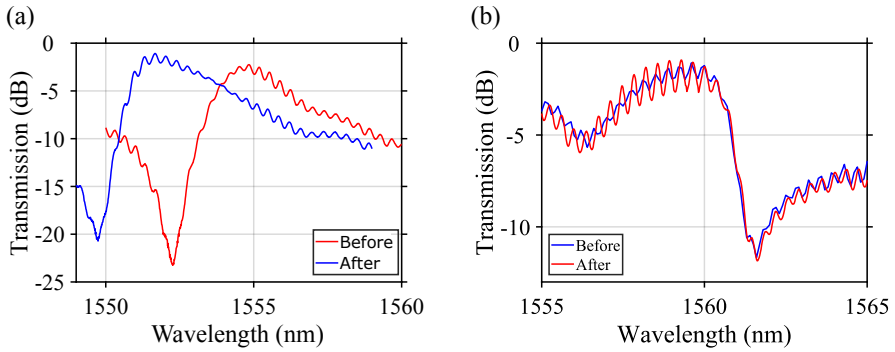

Figure C.1: (a) Transmission spectra of a reference (uncoated) sample before (red line) and after (blue line) signal reshaping experiment which involves using a 10 GHz pulse with average power of 9.8 dBm. The resonance peak blue-shifts by $\sim$ 3.5 nm due to irreversible oxidation of the photonic crystal membrane around the cavity region. (b) Transmission spectra of a 5 nm ALD Al_2O_3 coated sample before (blue line) and after (red line) pulse carving experiment which involves using a 10 GHz pulse with average power of 14.5 dBm. Both power levels are measured before the Fano device, and input coupling losses are around 10 dB.

cavity, but it has been reported in [12] that ALD coating does not decrease the quality factor of photonic crystal cavities. Additionally, The effect of ALD coating on the recovery time for our InP photonic crystal cavities is yet to be investigated. A major issue could be that it will lead to further reduction of the surface recombination velocity which is already slow in uncoated InP compared to GaAs. This might further increase the relaxation time of the carriers.

Generally, ALD coating can improve the device stability. However, careful design and characterization is required in order to fully exploit its advantages. The design goal should be to estimate an optimal Al_2O_3 layer thickness required to achieve device stability without compromising the key features of the Fano device such as the large switching contrast, efficient carrier-induced nonlinearities, and carrier relaxation time constants.

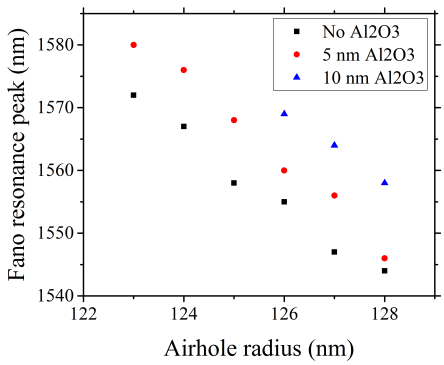

Figure C.2: Measured Fano resonance peak wavelength vs target airhole radius for a reference sample without ALD deposition of Al_2O_3 (black squares), a sample with 5 nm of Al_2O_3 (red dots), and a sample with 10 nm of ALD deposited Al_2O_3 layer (blue triangles).

Appendix D

Optical time domain demultiplexing setup

Figure D.1 shows the full setup used for optical time domain demultiplexing experiment. It consists of the OTDM transmitter, the Fano DeMUX device, and the receiver sections. Pulsed laser output from the mode locked laser (MLL) at 1557 nm is amplified and coupled into a 400 m highly nonlinear fiber (HNLF). This generates a supercontinuum ranging from 1530 nm to 1580 nm. The supercontinuum signal is then split into two arms one of which constitutes the pump signal while the other is the probe signal. The bandwidth and center frequency of both the pump and the probe signals are selected using a tunable optical band pass filter (OBPF). The pump signal is then on-off keying modulated by a Mach Zehnder modulator (MZM) at 10 Gbit/s using a pseudo random bit sequence generated by a bit-pattern generator (BPG). The actual repetition rate of the pulse is extracted using a photo diode and used as a clock signal for modulation and detection. The 10 Gbit/s RZ-OOK modulated signal is then multiplexed to form a 40 Gbit/s OTDM signal by using a two-stage multiplexer. The time delay between the pump and the probe signals is adjusted using a delay line. The pump and probe signals are polarization controlled (PC) and combined using a 3 dB coupler before coupling to the Fano DeMUX switch. After demultiplexing by the Fano switch, the pump signal is filtered out using a band pass filter. The demultiplexed signal is the amplified and fed to the receiver section. At the receiver side, the demultiplexed signal is preamplified and detected by a 10 GHz photodiode. The noise loading amplifier and the variable optical attenuator (VOA) setup is used for the bit-error ratio (BER) measurements using the signal quality analyzer. The spectrum of the signals are monitored at various point using an optical spectrum analyzer. The eye diagram of the demultiplexed signal is monitored after the pump signal is filtered out.

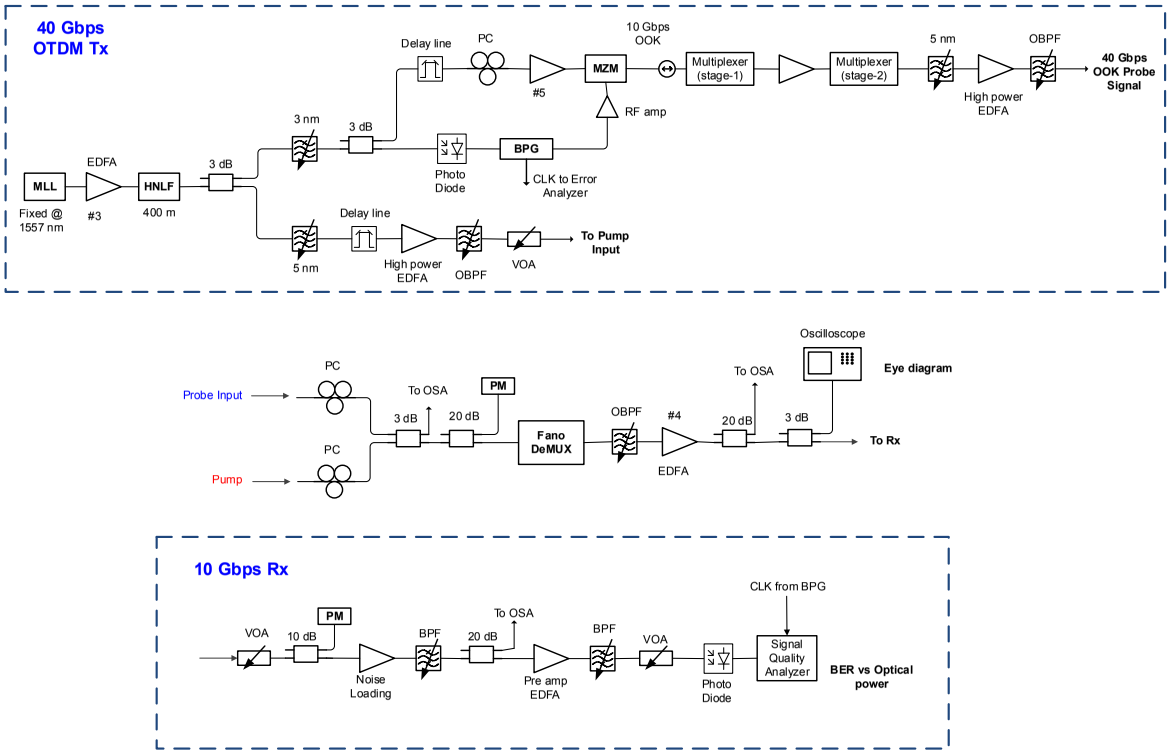

Figure D.1: Full setup for optical time domain demultiplexing experiment.

List of Acronyms

ALD Atomic Layer Deposition.

B2B Back-to-Back.

BCB Benzocyclobutene.

BHF Buffered hydrofluoric acid.

CAMFR CAvity Modelling FRamework.

CMT Coupled Mode Theory.

CW Continuous Wave.

E-beam Electron-beam.

ER Extinction ratio.

FCA Free-Carrier Absorption.

FDTD Finte difference time domain.

FoM Figure of Merit.

FWHM Full Width Half Maximum.

FWM Four Wave Mixing.

GaAs Gallium arsenide.

GaInP Galium Indium Phosphide.

HF hydrofluoric.

IBZ Irreducable Brillouin Zone.

InGaAs Indium gallium arsenide.

InGaAsP Indium Galium Arsenide Phosphide.

InP Indium Phosphide.

MOVPE Metalorganic vapour phase epitaxy.

MSM Metal Semiconductor Metal.

MZM Mach-Zehnder Modulator.

NOLM Nonlinear Optical Loop Mirror.

NRZ Non return-to-zero.

OOK On-Off Keying.

OTDM Optical Time Domain Multiplexing.

PECVD Plasma enhanced chemical vapour deposition.

PhC Photonic crystal.

PhCW Photonic crystal waveguide.

PML Perfectly matched layers.

PRBS Pseudo Random Bit Sequence.

RF Radio frequency.

RIE Reactive ion etching.

rpm revolutions per minute.

RZ Return-to-zero.

SEM Scanning electron microscope.

Si Silicon.

SOA Semiconductor Optical Amplifier.

SOI Silicon on Insulator.

SPM Self-Phase Modulation.

TBP Time-bandwidth product.

TE Transverse Electric.

TM Transverse Magnetic.

WDM Wavelength Division Multiplexing.

XPM Cross-Phase Modulation.

Bibliography

[1] L. Atzori, A. Iera, and G. Morabito, "The internet of things: A survey," *Computer networks*, vol. 54, no. 15, pp. 2787–2805, 2010.

[2] D. A. B. Miller, "Device requirements for optical interconnects to silicon chips," *Proceedings of the IEEE*, vol. 97, no. 7, pp. 1166–1185, July 2009.

[3] H. J. Caulfield and S. Dolev, "Why future supercomputing requires optics," *Nature Photonics*, vol. 4, no. 5, p. 261, 2010.

[4] D. A. Miller, "Attojoule optoelectronics for low-energy information processing and communications," *Journal of Lightwave Technology*, vol. 35, no. 3, pp. 346–396, 2017.

[5] A. F. Benner, M. Ignatowski, J. A. Kash, D. M. Kuchta, and M. B. Ritter, "Exploitation of optical interconnects in future server architectures," *IBM Journal of Research and Development*, vol. 49, no. 4.5, pp. 755–775, 2005.

[6] D. A. Miller, "Are optical transistors the logical next step?" *Nature Photonics*, vol. 4, no. 1, p. 3, 2010.

[7] A. E. Willner, S. Khaleghi, M. R. Chitgarha, and O. F. Yilmaz, "All-optical signal processing," *Journal of Lightwave Technology*, vol. 32, no. 4, pp. 660–680, 2014.

[8] K. Nozaki, T. Tanabe, A. Shinya, S. Matsuo, T. Sato, H. Taniyama, and M. Notomi, "Sub-femtojoule all-optical switching using a photonic-crystal nanocavity," *Nature Photonics*, vol. 4, no. 7, p. 477, 2010.

[9] V. R. Almeida, C. A. Barrios, R. R. Panepucci, and M. Lipson, "All-optical control of light on a silicon chip," *Nature*, vol. 431, no. 7012, p. 1081, 2004.

[10] E. Kuramochi, K. Nozaki, A. Shinya, K. Takeda, T. Sato, S. Matsuo, H. Taniyama, H. Sumikura, and M. Notomi, "Large-scale integration of wavelength-addressable all-optical memories on a photonic crystal chip," *Nature Photonics*, vol. 8, no. 6, p. 474, 2014.

[11] L. O'Faolain, D. M. Beggs, T. P. White, T. Kampfrath, K. Kuipers, and T. F. Krauss, "Compact optical switches and modulators based on dispersion engineered photonic crystals," *IEEE Photonics Journal*, vol. 2, no. 3, pp. 404–414, 2010.

[12] G. Moille, S. Combrié, L. Morgenroth, G. Lehoucq, F. Neuilly, B. Hu, D. Decoster, and A. de Rossi, "Integrated all-optical switch with 10 ps time resolution enabled by ALD," *Laser & Photonics Reviews*, vol. 10, no. 3, pp. 409–419, 2016.

[13] M. Pu, L. Ottaviano, E. Semenova, and K. Yvind, "Efficient frequency comb generation in AlGaAs-on-insulator," *Optica*, vol. 3, no. 8, pp. 823–826, 2016.

[14] P. Yu, T. Hu, H. Qiu, F. Ge, H. Yu, X. Jiang, and J. Yang, "Fano resonances in ultracompact waveguide Fabry-Perot resonator side-coupled lossy nanobeam cavities," *Applied Physics Letters*, vol. 103, no. 9, p. 091104, 2013.

[15] Z. Zhang and M. Qiu, "Small-volume waveguide-section high Q microcavities in 2D photonic crystal slabs," *Optics Express*, vol. 12, no. 17, pp. 3988–3995, 2004.

[16] J. D. Jackson, *Classical electrodynamics*. John Wiley & Sons, 1999.

[17] J. D. Joannopoulos, S. G. Johnson, J. N. Winn, and R. D. Meade, *Photonic crystals: molding the flow of light*. Princeton University press, 2011.

[18] R. W. Boyd, *Nonlinear optics*. Academic press, 2008.

[19] G. P. Agrawal, *Fiber-optic communication systems*. John Wiley & Sons, 2012.

[20] B. E. Saleh, M. C. Teich, and B. E. Saleh, *Fundamentals of photonics*. Wiley New York, 1991, vol. 22.

[21] L. Novotny and B. Hecht, *Principles of nano-optics*. Cambridge university press, 2012.

[22] W. Cai and V. M. Shalaev, *Optical metamaterials*. Springer, 2010, vol. 10, no. 6011.

[23] M. Fox, *Optical properties of solids*. Oxford university press, 2010.

[24] J. Leuthold, C. Koos, and W. Freude, "Nonlinear silicon photonics," *Nature Photonics*, vol. 4, no. 8, p. 535, 2010.

[25] N. Suzuki and K. Tada, "Electrooptic properties and raman scattering in InP," *Japanese Journal of Applied Physics*, vol. 23, no. 3R, p. 291, 1984.

[26] M. Giovannini, M. Beck, N. Hoyler, and J. Faist, "Second harmonic generation in (111)-oriented InP-based quantum cascade laser," *Journal of applied physics*, vol. 101, no. 10, p. 103107, 2007.

[27] H. Kawashima, Y. Tanaka, N. Ikeda, Y. Sugimoto, T. Hasama, and H. Ishikawa, "Optical bistable response in AlGaAs-based photonic crystal microcavities and related nonlinearities," *IEEE Journal of Quantum Electronics*, vol. 44, no. 9, pp. 841–849, 2008.

[28] B. R. Bennett, R. A. Soref, and J. A. Del Alamo, "Carrier-induced change in refractive index of InP, GaAs and InGaAsP," *IEEE Journal of Quantum Electronics*, vol. 26, no. 1, pp. 113–122, 1990.

[29] T. Vallaitis, S. Bogatscher, L. Alloatti, P. Dumon, R. Baets, M. L. Scimeca, I. Biaggio, F. Diederich, C. Koos, W. Freude *et al.*, "Optical properties of highly nonlinear silicon-organic hybrid (SOH) waveguide geometries," *Optics express*, vol. 17, no. 20, pp. 17 357–17 368, 2009.

[30] M. Dinu, F. Quochi, and H. Garcia, "Third-order nonlinearities in silicon at telecom wavelengths," *Applied physics letters*, vol. 82, no. 18, pp. 2954–2956, 2003.

[31] H. Tsang, R. Penty, I. White, R. Grant, W. Sibbett, J. Soole, H. LeBlanc, N. Andreadakis, R. Bhat, and M. Koza, "Two-photon absorption and self-phase modulation in InGaAsP/InP multi-quantum-well waveguides," *Journal of applied physics*, vol. 70, no. 7, pp. 3992–3994, 1991.

[32] D. Vignaud, J. Lampin, and F. Mollot, "Two-photon absorption in InP substrates in the 1.55 μ m range," *Applied physics letters*, vol. 85, no. 2, pp. 239–241, 2004.

[33] H. Oda, K. Inoue, Y. Tanaka, N. Ikeda, Y. Sugimoto, H. Ishikawa, and K. Asakawa, "Self-phase modulation in photonic-crystal-slab line-defect waveguides," *Applied physics letters*, vol. 90, no. 23, p. 231102, 2007.

[34] S. Auyang and P. Wolff, "Free-carrier-induced third-order optical nonlinearities in semiconductors," *JOSA B*, vol. 6, no. 4, pp. 595–605, 1989.

[35] S. Adachi, *Physical properties of III-V semiconductor compounds.* John Wiley & Sons, 1992.

[36] A. de Rossi, M. Lauritano, S. Combrié, Q. V. Tran, and C. Husko, "Interplay of plasma-induced and fast thermal nonlinearities in a GaAs-based photonic crystal nanocavity," *Physical Review A*, vol. 79, no. 4, p. 043818, 2009.

[37] F. G. Della Corte, G. Cocorullo, M. Iodice, and I. Rendina, "Temperature dependence of the thermo-optic coefficient of InP, GaAs, and SiC from room temperature to 600 k at the wavelength of 1.5 μm," *Applied Physics Letters*, vol. 77, no. 11, pp. 1614–1616, 2000.

[38] D. Breuer and K. Petermann, "Comparison of NRZ- and RZ-modulation format for 40-gb/s TDM standard-fiber systems," *IEEE Photonics Technology Letters*, vol. 9, no. 3, pp. 398–400, March 1997.

[39] R. A. Shafik, M. S. Rahman, A. R. Islam, and N. S. Ashraf, "On the error vector magnitude as a performance metric and comparative analysis," in *2006 International Conference on Emerging Technologies*, Nov 2006, pp. 27–31.

[40] C. Jamois, R. Wehrspohn, L. Andreani, C. Hermann, O. Hess, and U. Gösele, "Silicon-based two-dimensional photonic crystal waveguides," *Photonics and Nanostructures-Fundamentals and Applications*, vol. 1, no. 1, pp. 1–13, 2003.

[41] S. G. Johnson and J. D. Joannopoulos, "Block-iterative frequency-domain methods for Maxwell's equations in a planewave basis," *Optics express*, vol. 8, no. 3, pp. 173–190, 2001.

[42] L. O'Faolain, S. A. Schulz, D. M. Beggs, T. P. White, M. Spasenović, L. Kuipers, F. Morichetti, A. Melloni, S. Mazoyer, J.-P. Hugonin *et al.*, "Loss engineered slow light waveguides," *Optics express*, vol. 18, no. 26, pp. 27 627–27 638, 2010.

[43] S. G. Johnson and J. D. Joannopoulos. The MIT photonic-bands package home page. [Online]. Available: https://mpb.readthedocs.io/en/latest/

[44] J. Li, T. P. White, L. O'Faolain, A. Gomez-Iglesias, and T. F. Krauss, "Systematic design of flat band slow light in photonic crystal waveguides," *Optics Express*, vol. 16, no. 9, pp. 6227–6232, 2008.

[45] L. H. Frandsen, A. V. Lavrinenko, J. Fage-Pedersen, and P. I. Borel, "Photonic crystal waveguides with semi-slow light and tailored dispersion properties," *Optics Express*, vol. 14, no. 20, pp. 9444–9450, 2006.

[46] D. Taillaert, F. Van Laere, M. Ayre, W. Bogaerts, D. Van Thourhout, P. Bienstman, and R. Baets, "Grating couplers for coupling between optical fibers and nanophotonic waveguides," *Japanese Journal of Applied Physics*, vol. 45, no. 8R, p. 6071, 2006.

[47] Q. V. Tran, S. Combrié, P. Colman, and A. De Rossi, "Photonic crystal membrane waveguides with low insertion losses," *Applied Physics Letters*, vol. 95, no. 6, p. 061105, 2009.

[48] Y. Yu, "Photonic crystal nanocavity devices for nonlinear signal processing," Ph.D. dissertation, Technical University of Denmark, 2015.

[49] Y. Ding, H. Ou, and C. Peucheret, "Ultrahigh-efficiency apodized grating coupler using fully etched photonic crystals," *Optics letters*, vol. 38, no. 15, pp. 2732–2734, 2013.

[50] L. Liu, M. Pu, K. Yvind, and J. M. Hvam, "High-efficiency, large-bandwidth silicon-on-insulator grating coupler based on a fully-etched photonic crystal structure," *Applied physics letters*, vol. 96, no. 5, p. 051126, 2010.

[51] F. Van Laere, T. Stomeo, D. Taillaert, G. Roelkens, D. Van Thourhout, T. F. Krauss, and R. Baets, "Efficient polarization diversity grating couplers in bonded InP-membrane," *IEEE Photonics Technology Letters*, vol. 20, no. 4, pp. 318–320, 2008.

[52] L. Chen, L. Zhang, C. R. Doerr, N. Dupuis, N. G. Weimann, and R. F. Kopf, "Efficient membrane grating couplers on InP," *IEEE Photonics Technology Letters*, vol. 22, no. 12, pp. 890–892, 2010.

[53] P. Bienstman, "Rigorous and efficient modelling of wavelenght scale photonic components," Ph.D. dissertation, Ghent University, 2001.

[54] A. E. Miroshnichenko, S. Flach, and Y. S. Kivshar, "Fano resonances in nanoscale structures," *Reviews of Modern Physics*, vol. 82, no. 3, p. 2257, 2010.

[55] S. Fan, "Sharp asymmetric line shapes in side-coupled waveguide-cavity systems," *Applied Physics Letters*, vol. 80, no. 6, pp. 908–910, 2002.

[56] Y. Yu, E. Palushani, M. Heuck, N. Kuznetsova, P. T. Kristensen, S. Ek, D. Vukovic, C. Peucheret, L. K. Oxenløwe, S. Combrié *et al.*, "Switching characteristics of an InP photonic crystal nanocavity: Experiment and theory," *Optics express*, vol. 21, no. 25, pp. 31 047–31 061, 2013.

[57] S. Fan, W. Suh, and J. D. Joannopoulos, "Temporal coupled-mode theory for the Fano resonance in optical resonators," *JOSA A*, vol. 20, no. 3, pp. 569–572, 2003.

[58] W. Suh, Z. Wang, and S. Fan, "Temporal coupled-mode theory and the presence of non-orthogonal modes in lossless multimode cavities," *IEEE Journal of Quantum Electronics*, vol. 40, no. 10, pp. 1511–1518, 2004.

[59] M. Heuck, P. T. Kristensen, Y. Elesin, and J. Mørk, "Improved switching using Fano resonances in photonic crystal structures," *Optics letters*, vol. 38, no. 14, pp. 2466–2468, 2013.

[60] Y. Yu, H. Hu, L. K. Oxenløwe, K. Yvind, and J. Mork, "Ultrafast all-optical modulation using a photonic-crystal Fano structure with broken symmetry," *Optics letters*, vol. 40, no. 10, pp. 2357–2360, 2015.

[61] Y. Yu, W. Xue, E. Semenova, K. Yvind, and J. Mork, "Demonstration of a self-pulsing photonic crystal Fano laser," *Nature Photonics*, vol. 11, no. 2, p. 81, 2017.

[62] T. S. Rasmussen, Y. Yu, and J. Mork, "Theory of self-pulsing in photonic crystal Fano lasers," *Laser & Photonics Reviews*, vol. 11, no. 5, 2017.

[63] J. Mork, Y. Chen, and M. Heuck, "Photonic crystal Fano laser: terahertz modulation and ultrashort pulse generation," *Physical review letters*, vol. 113, no. 16, p. 163901, 2014.

[64] T. S. Rasmussen, Y. Yu, and J. Mork, "Modes, stability, and small-signal response of photonic crystal Fano lasers," *Optics Express*, vol. 26, no. 13, pp. 16 365–16 376, 2018.

[65] Y. Yu, Y. Chen, H. Hu, W. Xue, K. Yvind, and J. Mork, "Nonreciprocal transmission in a nonlinear photonic-crystal Fano structure with broken symmetry," *Laser & Photonics Reviews*, vol. 9, no. 2, pp. 241–247, 2015.

[66] B. Luk'yanchuk, N. I. Zheludev, S. A. Maier, N. J. Halas, P. Nordlander, H. Giessen, and C. T. Chong, "The Fano resonance in plasmonic nanostructures and metamaterials," *Nature materials*, vol. 9, no. 9, p. 707, 2010.

[67] Y. Yu, M. Heuck, H. Hu, W. Xue, C. Peucheret, Y. Chen, L. K. Oxenløwe, K. Yvind, and J. Mørk, "Fano resonance control in a photonic crystal structure and its application to ultrafast switching," *Applied Physics Letters*, vol. 105, no. 6, p. 061117, 2014.

[68] G. Moille, S. Combrié, K. Fuchs, M. Yacob, J. P. Reithmaier, and A. de Rossi, "Acceleration of the nonlinear dynamics in p-doped indium phosphide nanoscale resonators," *Optics letters*, vol. 42, no. 4, pp. 795–798, 2017.

[69] A. D. Osterkryger, J. R. de Lasson, M. Heuck, Y. Yu, J. Mørk, and N. Gregersen, "Spectral symmetry of Fano resonances in a waveguide coupled to a microcavity," *Optics letters*, vol. 41, no. 9, pp. 2065–2068, 2016.

[70] M. Galli, S. Portalupi, M. Belotti, L. Andreani, L. O'Faolain, and T. Krauss, "Light scattering and fano resonances in high-Q photonic crystal nanocavities," *Applied Physics Letters*, vol. 94, no. 7, p. 071101, 2009.

[71] L. A. Coldren, S. W. Corzine, and M. L. Mashanovitch, *Diode lasers and photonic integrated circuits*. John Wiley & Sons, 2012, vol. 218.

[72] D. A. Bekele, Y. Yu, H. Hu, P. Guan, L. Ottaviano, M. Galili, L. K. Oxenløwe, K. Yvind, and J. Mork, "Pulse carving using nanocavity-enhanced nonlinear effects in photonic crystal Fano structures." *Optics letters*, vol. 43, no. 4, pp. 955–958, 2018.

[73] P. E. Barclay, K. Srinivasan, and O. Painter, "Nonlinear response of silicon photonic crystal microresonators excited via an integrated waveguide and fiber taper," *Optics express*, vol. 13, no. 3, pp. 801–820, 2005.

[74] T. Uesugi, B.-S. Song, T. Asano, and S. Noda, "Investigation of optical nonlinearities in an ultra-high-Q Si nanocavity in a two-dimensional photonic crystal slab," *Optics express*, vol. 14, no. 1, pp. 377–386, 2006.

[75] M. Heuck, S. Combrié, G. Lehoucq, S. Malaguti, G. Bellanca, S. Trillo, P. T. Kristensen, J. Mørk, J. Reithmaier, and A. De Rossi, "Heterodyne pump probe measurements of nonlinear dynamics in an indium phosphide photonic crystal cavity," *Applied Physics Letters*, vol. 103, no. 18, p. 181120, 2013.

[76] Y. Rosenwaks, Y. Shapira, and D. Huppert, "Picosecond time-resolved luminescence studies of surface and bulk recombination processes in InP," *Physical Review B*, vol. 45, no. 16, p. 9108, 1992.

[77] L. E. Black, "Surface Recombination Theory," in *New Perspectives on Surface Passivation: Understanding the Si-Al2O3 Interface*. Springer, 2016, pp. 15–28.

[78] S. Krishnamurthy, Z. G. Yu, L. P. Gonzalez, and S. Guha, "Temperature-and wavelength-dependent two-photon and free-carrier absorption in GaAs, InP, GaInAs, and InAsP," *Journal of Applied Physics*, vol. 109, no. 3, p. 033102, 2011.

[79] X. Zhao, C. Lou, H. Zhou, D. Lu, and L. Huo, "Optical regenerative NRZ to RZ format conversion based on cascaded lithium niobate modulators," *Optics express*, vol. 18, no. 23, pp. 23 657–23 663, 2010.

[80] P. T. Kristensen, J. R. de Lasson, M. Heuck, N. Gregersen, and J. Mørk, "On the theory of coupled modes in optical cavity-waveguide structures," *Journal of Lightwave Technology*, vol. 35, no. 19, pp. 4247–4259, 2017.

[81] A. Weiner, *Ultrafast optics*. John Wiley & Sons, 2011, vol. 72.

[82] D. A. Bekele, Y. Yu, H. Hu, P. Guan, M. Galili, L. Ottaviano, L. K. Oxenløwe, K. Yvind, and J. Mork, "Signal reshaping and noise suppression using photonic crystal Fano structures," *Optics express*, vol. 26, 2018.

[83] O. Leclerc, B. Lavigne, E. Balmefrezol, P. Brindel, L. Pierre, D. Rouvillain, and F. Seguineau, "Optical regeneration at 40 Gb/s and beyond," *Journal of Lightwave Technology*, vol. 21, no. 11, pp. 2779–2790, 2003.

[84] R. Slavík, F. Parmigiani, J. Kakande, C. Lundström, M. Sjödin, P. A. Andrekson, R. Weerasuriya, S. Sygletos, A. D. Ellis, L. Grüner-Nielsen *et al.*, "All-optical phase and amplitude regenerator for next-generation telecommunications systems," *Nature Photonics*, vol. 4, no. 10, p. 690, 2010.

[85] F. Ohman, S. Bischoff, B. Tromborg, and J. Mork, "Noise and regeneration in semiconductor waveguides with saturable gain and absorption," *IEEE journal of quantum electronics*, vol. 40, no. 3, pp. 245–255, 2004.

[86] J. Mork, F. Ohman, and S. Bischoff, "Analytical expression for the bit error rate of cascaded all-optical regenerators," *IEEE Photonics Technology Letters*, vol. 15, no. 10, pp. 1479–1481, 2003.

[87] K. Lenglé, M. Gay, A. Bazin, I. Sagnes, R. Braive, P. Monnier, L. Bramerie, N. Nguyen, C. Pareige, R. Madec *et al.*, "Fast all-optical 10 Gb/s NRZ wavelength conversion and power limiting function using hybrid InP on SOI nanocavity," in *European Conference and Exhibition on Optical Communication*. Optical Society of America, 2012, pp. We–2.

[88] T.-H. Nguyen, K. Lenglé, A. Bazin, L. Bramerie, C. Peucheret, M. Gay, O. Sentieys, J.-C. Simon, R. Raj, and F. Raineri, "Phase-preserving power limiting function using InP on SOI photonic crystal nanocavity," *IEEE Photonics Technology Letters*, vol. 26, no. 12, pp. 1215–1218, 2014.

[89] R. Salem, M. A. Foster, A. C. Turner, D. F. Geraghty, M. Lipson, and A. L. Gaeta, "Signal regeneration using low-power four-wave mixing on silicon chip," *Nature photonics*, vol. 2, no. 1, p. 35, 2008.

[90] P. Mechet, T. Spuesens, S. Werquin, K. Vandoorne, N. Olivier, J.-M. Fedeli, P. Regreny, D. Van Thourhout, G. Roelkens, and G. Morthier, "All-optical low-power 2R regeneration of 10-Gb/s NRZ signals using a III-V on SOI microdisk laser," *IEEE Photonics Journal*, vol. 5, no. 6, pp. 7 802 510–7 802 510, 2013.

[91] M. Tassaert, H. Dorren, G. Roelkens, and O. Raz, "Passive InP regenerator integrated on SOI for the support of broadband silicon modulators," *Optics Express*, vol. 20, no. 10, pp. 11 383–11 388, 2012.

[92] T. Vivero, N. Calabretta, I. T. Monroy, G. Kassar, F. Öhman, K. Yvind, A. González-Marcos, and J. Mørk, "2r-regeneration in a monolithically integrated four-section SOA–EA chip," *Optics communications*, vol. 282, no. 1, pp. 117–121, 2009.

[93] D. A. Bekele, Y. Yu, H. Hu, P.-Y. Bony, L. Ottaviano, L. Oxenløwe, K. Yvind, and J. Mørk, "Optical time domain demultiplexing using Fano resonance in InP photonic crystals," in *The European Conference on Lasers and Electro-Optics*. Optical Society of America, 2017, p. CK_1_5.

[94] M. Heuck, P. T. Kristensen, and J. Mørk, "Energy-bandwidth trade-off in all-optical photonic crystal microcavity switches," *Optics Express*, vol. 19, no. 19, pp. 18 410–18 422, 2011.

[95] B. Lavigne, P. Guerber, P. Brindel, E. Balmefrezol, and B. Dagens, "Cascade of 100 optical 3R regenerators at 40 Gbit/s based on all-active Mach Zehnder interferometers," in *Optical Communication, 2001. ECOC'01. 27th European Conference on*, vol. 3. IEEE, 2001, pp. 290–291.

[96] D. A. Bekele, Y. Yu, H. Hu, Y. Ding, A. Sakanas, L. Ottaviano, E. Semenova, L. K. Oxenløwe, K. Yvind, and J. Mork, "Photonic crystal Fano resonances for realizing optical switches, lasers, and non-reciprocal elements," in *Active Photonic Platforms IX*, vol. 10345. International Society for Optics and Photonics, 2017, p. 103451V.

[97] S. L. Danielsen, P. B. Hansen, and K. E. Stubkjaer, "Wavelength conversion in optical packet switching," *Journal of Lightwave technology*, vol. 16, no. 12, pp. 2095–2108, 1998.

[98] J. Yu, X. Zheng, C. Peucheret, A. T. Clausen, H. N. Poulsen, and P. Jeppesen, "All-optical wavelength conversion of short pulses and NRZ signals based on a nonlinear optical loop mirror," *Journal of Lightwave Technology*, vol. 18, no. 7, p. 1007, 2000.

[99] T. Sakamoto, F. Futami, K. Kikuchi, S. Takeda, Y. Sugaya, and S. Watanabe, "All-optical wavelength conversion of 500-fs pulse trains by using a nonlinear-optical loop mirror composed of a highly nonlinear DSF," *IEEE Photonics Technology Letters*, vol. 13, no. 5, pp. 502–504, 2001.

[100] P. A. Andersen, T. Tokle, Y. Geng, C. Peucheret, and P. Jeppesen, "Wavelength conversion of a 40-Gb/s RZ-DPSK signal using four-wave mixing in a dispersion-flattened highly nonlinear photonic crystal fiber," *IEEE Photonics Technology Letters*, vol. 17, no. 9, pp. 1908–1910, 2005.

[101] J. H. Lee, W. Belardi, K. Furusawa, P. Petropoulos, Z. Yusoff, T. M. Monro, and D. J. Richardson, "Four-wave mixing based 10-Gb/s tunable wavelength conversion using a holey fiber with a high SBS threshold," *IEEE Photonics Technology Letters*, vol. 15, no. 3, pp. 440–442, 2003.

[102] J. Dong, X. Zhang, S. Fu, J. Xu, P. Shum, and D. Huang, "Ultrafast all-optical signal processing based on single semiconductor optical amplifier and

optical filtering," *IEEE Journal of Selected Topics in Quantum Electronics*, vol. 14, no. 3, pp. 770–778, 2008.

[103] M. Matsuura, N. Kishi, and T. Miki, "Ultrawideband wavelength conversion using cascaded SOA-based wavelength converters," *Journal of Lightwave Technology*, vol. 25, no. 1, pp. 38–45, 2007.

[104] K. Lengle, L. Bramerie, M. Gay, M. C. e Silva, S. Lobo, J.-C. Simon, P. Colman, S. Combrie, and A. De Rossi, "Investigation of FWM in dispersion-engineered GaInP photonic crystal waveguides," *Optics Express*, vol. 20, no. 15, pp. 16 154–16 165, 2012.

[105] K. Lenglé, T. N. Nguyen, M. Gay, L. Bramerie, J.-C. Simon, A. Bazin, F. Raineri, and R. Raj, "Modulation contrast optimization for wavelength conversion of a 20 Gbit/s data signal in hybrid InP/SOI photonic crystal nanocavity," *Optics letters*, vol. 39, no. 8, pp. 2298–2301, 2014.

[106] H. Murai, M. Kagawa, H. Tsuji, and K. Fujii, "EA-modulator-based optical time division multiplexing/demultiplexing techniques for 160-Gb/s optical signal transmission," *IEEE Journal of Selected Topics in Quantum Electronics*, vol. 13, no. 1, pp. 70–78, 2007.

[107] C. Koos, P. Vorreau, T. Vallaitis, P. Dumon, W. Bogaerts, R. Baets, B. Esembeson, I. Biaggio, T. Michinobu, F. Diederich *et al.*, "All-optical high-speed signal processing with silicon–organic hybrid slot waveguides," *Nature photonics*, vol. 3, no. 4, p. 216, 2009.

[108] K. Igarashi, K. Katoh, and K. Kikuchi, "Optoelectronic time-division demultiplexing of 160-Gbit/s optical signal based on phase modulation and spectral filtering," *Optics Express*, vol. 15, no. 3, pp. 845–851, 2007.

[109] I. Cestier, A. Willinger, V. Eckhouse, G. Eisenstein, S. Combrié, P. Colman, G. Lehoucq, and A. De Rossi, "Time domain switching/demultiplexing using four wave mixing in GaInP photonic crystal waveguides," *Optics express*, vol. 19, no. 7, pp. 6093–6099, 2011.

[110] B. Corcoran, M. D. Pelusi, C. Monat, J. Li, L. O'Faolain, T. F. Krauss, and B. J. Eggleton, "Ultracompact 160 Gbaud all-optical demultiplexing exploiting slow light in an engineered silicon photonic crystal waveguide," *Optics letters*, vol. 36, no. 9, pp. 1728–1730, 2011.

[111] C. Husko, A. De Rossi, S. Combrié, Q. V. Tran, F. Raineri, and C. W. Wong, "Ultrafast all-optical modulation in GaAs photonic crystal cavities," *Applied Physics Letters*, vol. 94, no. 2, p. 021111, 2009.

[112] M. S. Shur, *Handbook series on semiconductor parameters*. World Scientific, 1996, vol. 1.

[113] T. Tanabe, H. Taniyama, and M. Notomi, "Carrier diffusion and recombination in photonic crystal nanocavity optical switches," *Journal of Lightwave Technology*, vol. 26, no. 11, pp. 1396–1403, 2008.

[114] Y. Ding, H. Hu, H. Ou, L. K. Oxenløwe, and K. Yvind, "Effective carrier sweepout in a silicon waveguide by a metal-semiconductor-metal structure," in *Lasers and Electro-Optics (CLEO), 2015 Conference on*. IEEE, 2015, pp. 1–2.

[115] L.-D. Haret, X. Checoury, F. Bayle, N. Cazier, P. Boucaud, S. Combrié, and A. de Rossi, "Schottky MSM junctions for carrier depletion in silicon photonic crystal microcavities," *Optics express*, vol. 21, no. 8, pp. 10 324–10 334, 2013.

[116] H. K. Sahoo, L. Ottaviano, Y. Zheng, O. Hansen, and K. Yvind, "Low temperature bonding of heterogeneous materials using Al2O3 as an intermediate layer," *Journal of Vacuum Science & Technology B, Nanotechnology and Microelectronics: Materials, Processing, Measurement, and Phenomena*, vol. 36, no. 1, p. 011202, 2018.

[117] A. G. Baca and C. I. Ashby, *Fabrication of GaAs devices*. IET, 2005, no. 6.

[118] F. Intonti, N. Caselli, S. Vignolini, F. Riboli, S. Kumar, A. Rastelli, O. G. Schmidt, M. Francardi, A. Gerardino, L. Balet *et al.*, "Mode tuning of photonic crystal nanocavities by photoinduced non-thermal oxidation," *Applied Physics Letters*, vol. 100, no. 3, p. 033116, 2012.

[119] S. Kiravittaya, H. Lee, L. Balet, L. Li, M. Francardi, A. Gerardino, A. Fiore, A. Rastelli, and O. Schmidt, "Tuning optical modes in slab photonic crystal by atomic layer deposition and laser-assisted oxidation," *Journal of Applied Physics*, vol. 109, no. 5, p. 053115, 2011.